UNIVERSIDADE TÉCNICA DE LISBOA
INSTITUTO SUPERIOR TÉCNICO

Search for a fourth generation b'-quark at LEP-II

Nuno Filipe da Silva Fernandes de Castro

(Licenciado)

Dissertação para obtenção do Grau de Mestre em Física

Orientador: Professor Doutor António Joaquim Onofre de Abreu Ribeiro Gonçalves
Co-orientador: Professor Doutor Mário João Martins Pimenta

Constituição do Júri:
Presidente: Professor Doutor Mário João Martins Pimenta
Vogais: Professor Doutor Orlando Olavo Aragão Aleixo e Neves de Oliveira
Professor Doutor António Joaquim Onofre de Abreu Ribeiro Gonçalves
Professor Doutor Pedro Moraes Salgueiro Teixeira de Abreu

Março de 2004

Typeset with $\LaTeX$.

Ao Vô Lito,
que me ensinou a brincar aos cientistas.

Vanity of vanities, saith the Preacher, vanity of vanities; all is vanity.
What profit hath a man of all his labour which he taketh under the sun?
One generation passeth away, and another generation cometh.

Bible, *Ecclesiates 1:2*.

Each generation imagines itself to be more intelligent than the one that went before it, and wiser than the one that comes after it.

George Orwell.

Resumo

Na presente tese é apresentada uma análise dedicada à pesquisa da produção de pares de quarks sequenciais da quarta família em LEP ($e^+e^- \to b'\bar{b'}$). Os dados analisados foram recolhidos pelo detector DELPHI a energias de centro de massa que variaram entre 196 GeV e 209 GeV e que correspondem a uma luminosidade integrada de cerca de 420 pb^{-1}. Esta pesquisa foi motivada por medidas de precisão e pesquisas anteriores em LEP-I e em TEVATRON que são compatíveis com a existência de quarks b' com massa superior a $m_Z/2$.

Na região de massa estudada (96 GeV/c^2 $< m_{b'} <$ 103 GeV/c^2), os decaimentos $b' \to cW$ (através de correntes carregadas) e $b' \to bZ$ (através de correntes neutras com mudança de sabor) devem ser dominantes, de acordo com as previsões teóricas. Na ausência de sinal (produção dupla de quarks b'), foram estabelecidos limites superiores, com um nível de confiança de 95%, nas razões de decaimento dos dois modos estudados. Estes limites, conjugados com as previsões teóricas, foram usados para constranger os valores possíveis da razão $|\frac{V_{cb'}}{V_{tb'}V_{tb}}|$, onde $V_{cb'}$, $V_{tb'}$ e V_{tb} são elementos da matriz de Cabbibo-Kobayashi-Maskawa generalizada a quatro famílias. Dois casos extremos foram considerados: o caso degenerado ($m_{t'} - m_{b'} \sim 1$ GeV/c^2) e o caso onde a diferença de massas entre o b' e o t' está próxima do valor máximo permitido ($m_{t'} - m_{b'} \sim 50$ GeV/c^2).

Palavras Chave

LEP, DELPHI, quarta geração, hierarquia de massas dos fermiões, quarks, CKM

Abstract

In this thesis, a search for the pair production of sequential fourth generation quarks at LEP ($e^+e^- \to b'\bar{b}'$) is presented. The data collected by DELPHI at centre-of-mass energies ranging from 196 GeV to 209 GeV, corresponding to an integrated luminosity of about 420 pb^{-1}, were analysed. This search was motivated by the electroweak precision data and by previous searches for the pair production of b' quarks at LEP-I and at the TEVATRON, which still allow a b' heavier than $m_Z/2$.

In the considered mass range (96 GeV/c^2 $< m_{b'} <$ 103 GeV/c^2) the $b' \to cW$ (charged currents) and $b' \to bZ$ (flavour changing neutral currents) decay modes are expected to be dominant. In the absence of a signal, upper limits on the branching ratios of these decay modes were obtained at 95% confidence level. The obtained limits on $BR_{b' \to cW}$ and $BR_{b' \to bZ}$, together with the theoretical predictions within a sequential model, were used to constrain the values of $|\frac{V_{cb'}}{V_{tb'}V_{tb}}|$, where $V_{cb'}$, $V_{tb'}$ and V_{tb} are elements of the extended 4×4 Cabbibo-Kobayashi-Maskawa matrix. Two extreme cases were considered: the almost degenerate case ($m_{t'} - m_{b'} \sim 1$ GeV/c^2) and the case where the mass difference is close to the largest possible value ($m_{t'} - m_{b'} \sim 50$ GeV/c^2).

Key Words

LEP, DELPHI, fourth generation, fermion mass hierarchy, quarks, CKM

Acknowledgments

I owe a great debt of gratitude to Professor António Onofre, for having given me the opportunity to start this work, as well as for his unfailing help and guidance, during the last three years. This work was also co-oriented by Professor Mário Pimenta and researcher Catarina Espírito-Santo, whom I wish to thank for their patience and encouragement.

Professor Rui Santos, researcher Sancho Oliveira, as well as Professor Orlando Oliveira, gave an important contribution to the theoretical parts of this work. The theoretical interpretation of the experimental results obtained in this thesis has largely increased the relevance of the physical result, as it always happens. From my personal point of view, this was a wonderful example of how fruitful the collaboration between theoreticians and experimentalists can be.

I thank Laboratório de Instrumentação e Física Experimental de Partículas for all the support it has given me, namely by paying my grant during part of the time of this work. To the Centro de Física Computacional da Universidade de Coimbra I owe having had a working room during all these years. I also acknowledge the support given by the Fundação para a Ciência e a Tecnologia, through the grant with reference SFRH/BM/8130/2002.

To all the members of the Portuguese DELPHI group, a special thank you for the continuous support and friendship (if you can ever thank someone for their friendship). I was very lucky to have found such a nice and welcoming working group.

I want to thank Filipe Veloso, my working colleague, for his time, help, suggestions, support and, above all, for his friendship. To the other friends and colleagues, I also wish to say thank you for having accepted me among their midst.

To my family I owe their love and emotional support, but I am sure I will be able to find better ways to thank them for that. A very special word to Mariana, for everything that can not easily be written.

Contents

List of Figures

List of Tables

Chapter 1

INTRODUCTION

The Standard Model of particle physics (SM) is in excellent agreement with experimental data, but leaves nevertheless some open questions. Among other parameters, the number of fermion generations and their mass spectrum are not explained by the SM. Although the number of light neutrino species is well established, there are both experimental and theoretical motivations to search for a heavy fourth generation of fermions. In fact, such extra generation is not ruled out by the electroweak precision data and several SM extensions predict or even require additional fermions.

The most straightforward way of adding an additional generation of fermions is to assume that this new generation is a replica of the known families. In the quark sector, an up-type quark (t') and a down-type quark (b') are added. Although the existence of a leptonic sector is also needed to assure the cancellation of gauge anomalies, no assumptions on the masses and mixing of the leptons have to be made in order to study the quark sector. Assuming that the extended 4×4 Cabibibo-Kobayashi-Maskawa matrix have a structure similar to the 3×3 one, all the b' decay widths depend only on the ratio $R_{CKM} = |\frac{V_{cb'}}{V_{tb'}V_{tb}}|$ and on the t' and b' masses. The mass difference between the t' and b' is constrained by the electroweak precision data.

Previous searches for a sequential generation of quarks at LEP-I showed that the b' must be heavier than $m_Z/2$. At the TEVATRON, both the D∅ and CDF collaborations, established limits on the b' mass under assumptions on the branching ratios for a particular b' decay channel.

In this thesis, the pair production of a sequential fourth generation b'-quark at LEP ($e^+e^- \to b'\bar{b}'$) was studied in the b' mass range $96 \to 103$ GeV/c^2. The analysed data were collected with the DELPHI detector at LEP-II at centre-of-mass energies ranging from 196 GeV to 209 GeV. The relative importance of the possible b' decay modes depends on the b' mass. In the considered b' mass range, the $b' \to bZ$ (flavour changing neutral current) and $b' \to cW$ (charged current) decay modes are expected to be dominant. In the absence of a b' signal, 95% confidence level (CL) upper limits on the branching ratios as a function of $m_{b'}$ for these two b' decay modes can be established. The obtained limits, together with the theoretical predictions within a sequential model, can be used to set exclusions on the plane $(R_{CKM}, m_{b'})$ for two extreme cases: the almost degenerate case ($m_{t'} - m_{b'} = 1$ GeV/c^2) and the case where the mass difference is close to the largest possible value ($m_{t'} - m_{b'} = 50$ GeV/c^2).

The present thesis is organized as follows: the SM and its extensions including extra generations of fermions are discussed in chapter 2; the DELPHI detector is described in chapter 3; in chapter 4 the Monte Carlo generators for signal and background processes are presented; the data analysis is discussed in chapter 5; the results are presented in chapter 6 and the conclusions of this work are presented in chapter 7.

Chapter 2

THE FOURTH GENERATION OF QUARKS

In this chapter the present knowledge on fermions is briefly reviewed. Their family structure within the Standard Model of particle physics (SM) is presented in section 2.1 and the existence of additional fermion generations is discussed in section 2.2. Particular relevance is given to the production and decay of a sequential fourth generation b'-quark, which is the main subject of this thesis. Previous b'-quark searches at colliders are also reviewed.

2.1 The Standard Model

The SM is a gauge theory which incorporates the electroweak theory[1] (EW) [1, 2, 3] and quantum chromodynamics (QCD) [4, 5]. Although the SM symmetry group is not a theoretical prediction, $SU(2)_L \otimes U(1)_Y \otimes SU(3)_c$ is consistent with the known phenomenology. This group is the direct product of three gauge groups and coupling constants for each factor (g, g' and g_s) have to be chosen. The $SU(2)_L \otimes U(1)_Y$ and $SU(3)_c$ groups are associated with the EW and QCD theories, respectively.

The SM lagrangian, $\mathcal{L}_{SM}$, embodies the present knowledge of the electroweak and strong interactions. It can be divided into four sectors:

$$\mathcal{L}_{SM} = \mathcal{L}_{gauge} + \mathcal{L}_{matter} + \mathcal{L}_{Higgs} + \mathcal{L}_{Yukawa}\ . \qquad (2.1)$$

The $\mathcal{L}_{gauge}$ term describes the pure gauge interactions. The kinetic energy and the self interactions of the strong and electroweak fields are included in this sector.

The gauge interactions of the fermion (matter) fields, ψ_i, are included in $\mathcal{L}_{matter}$. These matter fields, associated to quarks and leptons of spin 1/2, are multiplets classified according to their helicity state: left handed (LH) doublets of $SU(2)_L$ and right

[1] The electroweak theory unifies the quantum electrodynamics (QED) with the weak interaction.

handed (RH) singlets of $U(1)_Y$:

$$\psi_i = \begin{pmatrix} U_i \\ D_i \end{pmatrix}_L,\ U_{iR},\ D_{iR} \qquad \text{(for quarks)} \tag{2.2}$$

and

$$\psi_i = \begin{pmatrix} \nu_i \\ l_i \end{pmatrix}_L,\ l_{iR} \qquad \text{(for leptons)}, \tag{2.3}$$

where U_i (D_i) stands for an up-type (down-type) quark, l_i represents a charged lepton and ν_i a neutrino. The index i runs over the number of fermion generations and the R (L) index stands for the right (left) handedness of the fermions.

The number of quark flavours has to be equal to the number of lepton species, *i.e.* although the number of fermion generations is a free parameter of the theory, the same number of lepton and quark families is required in order to cancel gauge anomalies. This cancellation assures that the theory is renormalizable [6, 7].

The introduction of mass terms in the lagrangian would explicitly break the local gauge symmetry. A possibility for the gauge bosons to acquire mass is through a mechanism of spontaneous symmetry breaking[2]. In the SM, this is achieved by introducing the Higgs field, ϕ [8, 9]. This field has a finite vacuum expectation value and its inclusion in the theory leads to the prediction of a massive scalar boson, the Higgs boson, which was not discovered until now. The characterization of ϕ requires two parameters: the vacuum expectation value, v, and μ, which is related to the Higgs boson mass ($m_H = \sqrt{2}\mu^2$). The Higgs sector of the theory is included in the SM lagrangian by the term $\mathcal{L}_{Higgs}$.

In the SM, the fermions acquire mass via Yukawa couplings to the Higgs field, which are included in $\mathcal{L}_{Yukawa}$. The SM assumes that there are no right handed neutrinos and therefore they are expected to be massless. Nevertheless, recently the SK [10], K2K [11], SNO [12] and KamLAND [13] collaborations reported an evidence for neutrino oscillation, which may indicate that neutrinos are massive. The extensions of the SM to accommodate massive neutrinos are beyond the scope of this thesis[3].

After the spontaneous symmetry breaking, the bosonic sector of the SM has one scalar field, corresponding to the neutral Higgs boson (H) two charged bosons (W^+ and W^-), two neutral bosons (Z and γ) and eight gluons (g). The gluons have an additional quantum number, the color (C) and are responsible for the strong interaction between quarks. Each quark exists in three color versions (red, green or blue).

The charged currents (CC) induce a mixing between the different generations of quarks. By convention, this mixing is described as a rotation of the down-type quarks, parameterized in terms of the Cabibbo-Kobayashi-Maskawa (CKM) matrix [16], V. For n generations of quarks, V is a $n \times n$ unitary matrix, whose elements have to be determined. Flavour changing neutral currents (FCNC) are absent at tree level but through CKM mixing can naturally appear at one-loop level [17].

[2]The difference is important because the theory with spontaneous symmetry breaking is renormalizable.

[3]A recent review on neutrino physics can be found in [14]. Possible extensions of the SM to accommodate massive neutrinos are discussed, for instance, in [15].

The fermion multiplets are eigenstates of the isospin operator, $\hat{T}$. The hypercharge, Y, is defined as $Y = 2(Q - T_3)$, where Q is the fermion electric charge (in units of the positron charge, e) and T_3 is the third component of the isospin. The quantum numbers of the SM fermions and bosons are summarized in table 2.1.

		T	T_3	Y	Q	C
leptons	ν_L	1/2	+1/2	-1	0	—
	l_L	1/2	-1/2	-1	-1	—
	l_R	0	0	-2	-1	—
quarks	U_L	1/2	+1/2	+1/3	+2/3	R,G,B
	D_L	1/2	-1/2	+1/3	-1/3	R,G,B
	U_R	0	0	+4/3	+2/3	R,G,B
	D_R	0	0	-2/3	-1/3	R,G,B
gauge bosons	B^0	0	0	0	0	—
	W^+	1	+1	0	+1	—
	W^0	1	0	0	0	—
	W^-	1	-1	0	-1	—
	gluons	0	0	0	0	(RGB)
Higgs	H	1/2	-1/2	1	0	—

Table 2.1: *The quantum numbers of the Standard Model particles are shown. To each fermion corresponds an anti-particle with opposite charge, but the same mass. L and R stands for the fermion helicity. The electric charges, Q, are normalized to the positron charge. R, G and B stand for the possible color charges (red, green and blue). The photon, γ, and the Z are linear combinations of the B^0 and W^0 bosonic fields.*

2.1.1 The number of light neutrino species

The number of light (*i.e.* with masses below $m_Z/2$) neutrinos species (N_ν), was established in 1989 by the measurement at LEP of the Z decay width [18, 19, 20, 21]. The fits to the Z hadronic line-shape assuming different N_ν [22] can be seen in figure 2.1.

The most recent result on N_ν was reported by the LEP Electroweak Working Group [24] and arises from the comparison of the partial width of the Z leptonic decay ($\Gamma_{Z\to l_i l_i}$) with the partial width corresponding to the invisible decay of the Z ($\Gamma_{Z\to inv}$):

$$\frac{\Gamma_{Z\to inv}}{\Gamma_{Z\to l_i l_i}} = 5.942 \pm 0.016 \ . \tag{2.4}$$

The SM prediction for the ratio of the partial widths to neutrinos and charged leptons is [24]:

$$\left(\frac{\Gamma_{Z\to \nu_i \nu_i}}{\Gamma_{Z\to l_i l_i}}\right)_{SM} = 1.9912 \pm 0.0012 \ . \tag{2.5}$$

N_ν is given by the ratio of the expressions 2.4 and 2.5:

$$N_\nu = 2.9841 \pm 0.0083 \ , \tag{2.6}$$

which establishes that the number of light neutrino species, N_ν, is three, with an error below 1%. From astrophysics, the study of the primordial abundance of ^{4}He also gives an indication of the existence of three light neutrino species [25, 26].

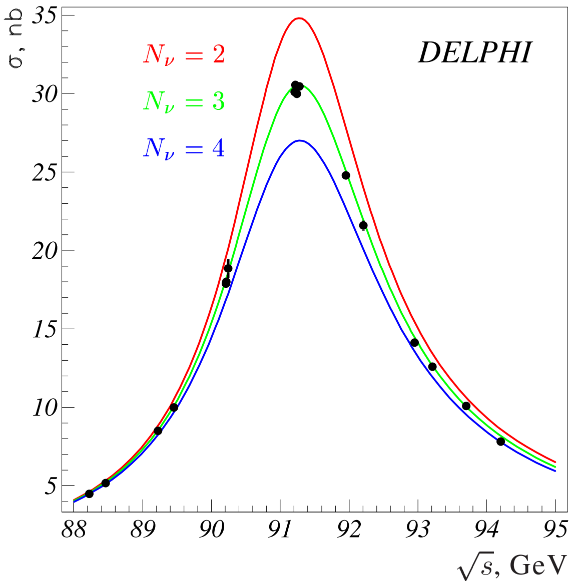

Figure 2.1: *The fits to the hadronic line-shape are shown for different hypothesis on the number of light neutrino species, N_ν [23].*

2.1.2 The Standard Model free parameters

The gauge and Higgs sectors of the SM depend on five parameters: the three gauge couplings (g, g' and g_S) and the two Higgs field parameters (v and μ). These parameters can be related with the following experimental measurable quantities[4]:

$$\alpha_{em} = \frac{(g \sin\theta_w)^2}{4\pi} \; , \quad \tan\theta_w = \frac{g}{g'} \; , \; m_Z^2 = \frac{g^2 v^2}{2\cos^2\theta_w} \; , \; m_H = \sqrt{2}\mu^2 \; .$$

The g_S coupling is related with α_S [27]. The measured values of these quantities and the 95% CL limits on the Higgs mass are shown in table 2.2.

quantity	value	uncertainty (ppb)
α_{em} ($Q^2 = 0$)	$7.297\,352\,533(27) \times 10^{-3}$ $(\epsilon_0 \hbar c)$	3.7
$\sin\theta_w(m_Z)$	$0.231\,13(15)$	6.5×10^5
$\alpha_s(m_Z)$	$0.117\,2(20)$	1.7×10^7
m_Z	$91.187\,6(21)$ GeV$/c^2$	2.3×10^4
m_H	114 GeV$/c^2 < m_H < 219$ GeV$/c^2$	—

Table 2.2: *Measured values of physical quantities [23] which can be used to define the SM gauge couplings. The 95% CL bounds on the Higgs mass are also shown: the lower bound was obtained from the direct searches at LEP [28] and the upper bound was set by the electroweak precision data [24]. The uncertainty associated to each measured value is expressed in parts per billion (ppb).*

In a three generations scenario[5], there are six quarks, three charged leptons and

[4]The choice of this set of observables is not unique. For example, the W mass ($m_W = gv/2$) or the Fermi constant ($G_F = 1/(2v^2)$) could also be chosen

[5]The result on N_ν supported the formulation of the SM with three families. Moreover, all the known fermions belong to those three generations.

three neutrinos. The masses of the quarks and charged leptons are free parameters of the SM to be determined experimentally (*c.f.* table 2.3).

generation	quark	mass (GeV/c^2)	charged lepton	mass (MeV/c^2)
first	u	1.5×10^{-3} to 4.5×10^{-3}	e	$0.510\,988\,9(21)$
	d	5×10^{-3} to 8.5×10^{-3}		
second	c	1.0 to 1.4	μ	$105.658\,356(52)$
	s	80×10^{-3} to 155×10^{-3}		
third	t	174.3 ± 5.1	τ	$1776^{+0.29}_{-0.26}$
	b	4.0 to 4.5		

Table 2.3: *Measured values of the known quark and charged lepton masses (three generations of fermions). The light quark (u, d and s) masses are estimates of the* current quark masses *[23].*

The CKM matrix elements are also free parameters of the SM[6]. Assuming only three generations and the unitarity of the CKM matrix, 90% confidence level limits on the magnitude of the V_{ij} elements can be determined [23]:

$$\begin{pmatrix} V_{ud} & V_{us} & V_{ub} \\ V_{cd} & V_{cs} & V_{cb} \\ V_{td} & V_{ts} & V_{tb} \end{pmatrix} = \begin{pmatrix} 0.9741 \text{ to } 0.9756 & 0.219 \text{ to } 0.226 & 0.0025 \text{ to } 0.0048 \\ 0.219 \text{ to } 0.226 & 0.9732 \text{ to } 0.9748 & 0.038 \text{ to } 0.044 \\ 0.004 \text{ to } 0.014 & 0.037 \text{ to } 0.044 & 0.9990 \text{ to } 0.9993 \end{pmatrix} \tag{2.7}$$

It is also possible to extend the 3×3 CKM matrix to accommodate more than three generations of fermions. In this case, the constraint imposed by unitarity cannot be used and the allowed ranges (at 90% confidence level) of the matrix elements connecting the first three generations are [23]:

$$\begin{pmatrix} 0.9721 \text{ to } 0.9747 & 0.215 \text{ to } 0.224 & 0.002 \text{ to } 0.005 & \dots \\ 0.209 \text{ to } 0.227 & 0.966 \text{ to } 0.976 & 0.038 \text{ to } 0.044 & \dots \\ 0 \text{ to } 0.09 & 0 \text{ to } 0.12 & 0.08 \text{ to } 0.9993 & \dots \\ \vdots & \vdots & \vdots & \ddots \end{pmatrix} \tag{2.8}$$

2.2 Fermions beyond the SM

Despite the success of the SM in describing the accumulated experimental data, it leaves some unanswered questions as, for instance, the number of fermion generations and their mass spectrum. In fact, although the number of light neutrinos is well established, the number of fermions generations is still unknown. Even if presently there is no evidence for extra generations of fermions, it is also true that there is no experimental or theoretical reason to exclude such hypothesis. In this section, models which allow fermions beyond the third generation are discussed.

[6]The 3×3 CKM matrix elements can be parameterized in terms of three angles and one phase.

2.2.1 Models with extra generations of fermions

Extra generations of fermions are present in several extensions of the SM [29, 30, 31, 32]. Some supersymmetric models [33, 34, 35], for instance, can accommodate or even require a fourth generation of fermions.

The most straightforward way of including another generation of fermions in the SM is to assume that this extra generation is a replica of the known families (sequential model). Such an extra SM-like generation of fermions needs both the quark and lepton sectors, which have quantum numbers similar to the known SM fermions. A fourth generation neutrino has to be heavy in order to avoid the LEP-I bound, which establishes that any new fermions that couple to the Z should have a mass larger than $m_Z/2$ [24]. The new fermions included in this way are chiral, as their left and right components transform differently under the $SU(2)_L \otimes U(1)_Y$ gauge group. In the quark sector, for example, an up-type quark, t', and a down-type quark, b', are added to the known ones:

$$\begin{pmatrix} t' \\ b' \end{pmatrix}_L , \; t'_R \, , \; b'_R \, . \tag{2.9}$$

Extra generations of mirror quarks or leptons are an alternative way of introducing new fermions. Mirror fermions have chiral properties opposite to the sequential fermions (*i.e.* the RH components are in the weak doublets and the LH ones are in the weak singlets) [36, 37].

There are also SM extensions which predict non-chiral fermions (called vector-like) with LH and RH components which transform similarly under $SU(2)_L \otimes U(1)_Y$. They can be either weak doublets [38] or singlets [39, 40, 41].

A sequential fourth generation of quarks (referred to as t' and b') will be considered in this thesis. Although within this model a leptonic sector is also required, no assumption on the new leptons masses or mixing has to be made [42, 43, 44].

2.2.2 Constraints from the electroweak precision data

High precision electroweak measurements can be used to constrain physics beyond the SM. The ρ parameter [29] is defined as:

$$\rho = \frac{m_W^2}{m_Z^2 \cos^2 \theta_w} \, , \tag{2.10}$$

and, at tree level, it is expected to be 1 within the SM. Any deviations from this value are related to electroweak radiative corrections, which should be sensitive to new fermions in the loops [45, 46]. The measured value of the ρ parameter is [23]:

$$\rho = 1.0012^{+0.0023}_{-0.0014} \, . \tag{2.11}$$

A chiral fourth generation of fermions, with both the new quarks and leptons being degenerate, is excluded at 99.8% confidence level. In this case, the number of fermion generations is expected to be 2.97 ± 0.30 [23, 47]. However, if a non-degenerate family of leptons is considered, a lower confidence level for exclusion is obtained [29]. Therefore, although a degenerate new family of fermions is disfavored, a non-degenerate one is still allowed.

Moreover, it was shown that the mass difference range $|m_{t'} - m_{b'}| \leq 60$ GeV/c^2, where t' and b' are the sequential fourth generation quarks, is consistent with the available data [29, 48]. These results are in agreement with a recent fit to the electroweak data [49, 50], which is compatible with the existence of a fourth generation: the χ^2 of the fit assuming three families of fermions is as good as the one with four generations with the new quark masses not too further apart.

2.2.3 The sequential fourth generation of quarks

In this section the production and decay of a fourth generation b' quark are discussed within the sequential model. This discussion is based on the calculations reported in [42, 43, 48]. A brief review of the previous searches for sequential b' quarks is also done.

Production and decay of the b'-quark

Fourth generation b'-quarks can be pair-produced both in lepton colliders ($e^+e^- \to \gamma/Z \to b'\bar{b}'$) and in hadron colliders ($p\bar{p} \to b'\bar{b}'$, through gluon fusion or quark/anti-quark annihilation).

The b'-quark may decay via CC to UW, with $U = t', t, c, u$, or via FCNC to DX, with $X = Z, H, \gamma, g$ and $D = b, s, d$ (figure 2.2).

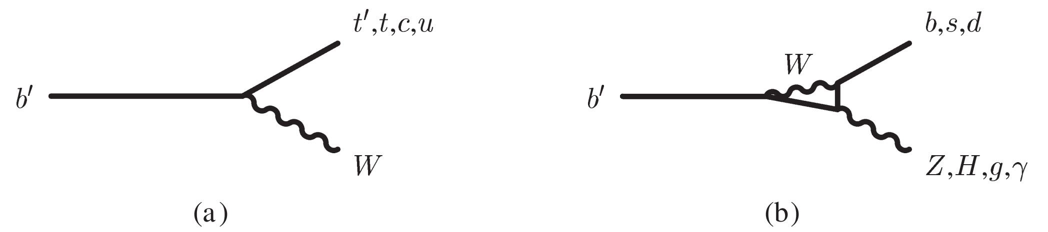

Figure 2.2: *Feynman diagrams corresponding to the (a) CC and (b) FCNC b' decay modes.*

The possible b' decays were calculated in [51, 52, 53, 54, 55, 56]. One peculiar aspect of the b' decays is that, depending on the values of the extended 4×4 CKM matrix elements, the FCNC decays can be as important as the CC decays [54]. The dominance of a particular decay mode depends on the values of the CKM matrix element and on the b' and t' masses: it is the so called *cocktail solution* [48].

In the sequential model, the extended 4×4 CKM matrix is expected to have a structure very similar to the SM one (3×3). If CP violation is not considered, all its elements are real. Furthermore, considering the approximate diagonality and the unitarity of the CKM matrix, it is possible to write all the branching ratios (BR) of the possible b' decay modes as a function of three quantities alone: $m_{t'}$, $m_{b'}$ and $R_{CKM} = |\frac{V_{cb'}}{V_{tb'}V_{tb}}|$ [42, 43].

The study of the possible b' decay modes was done assuming that t' is heavier than b' (which is motivated by the SM mass hierarchy) and by fixing the value of $m_{t'} - m_{b'}$. Two extreme cases were considered: the almost degenerate case ($m_{t'} - m_{b'} = 1$ GeV/c^2) and the case where the mass difference is close to the largest possible value ($m_{t'} - m_{b'} = 50$ GeV/c^2). In both cases, the decay $b' \to t'W$ is kinematically forbidden[7]. The decay $b' \to t'W^*$ although allowed, is phase space suppressed and consequently it is extremely small [57].

The relative importance of the possible b' decays depend on the considered b' mass. If $m_{b'} < m_W$, only the FCNC b' decays through a γ or a g are possible. In this case, $b' \to b\gamma$ and $b' \to bg$ decay modes are expected to be the dominant ($b' \to s\gamma, d\gamma$ and $b' \to sg, dg$ are expected to give a very small contribution to the total decay width.). The only two competitive decays for the mass range $m_Z < m_{b'} < m_H$ are $b' \to cW$ and $b' \to bZ$. As soon as the Higgs channel becomes available (*i.e.* when $m_{b'} > m_H + m_b$), the $BR_{b' \to bH}$ can be as large as the $BR_{b' \to bZ}$. The branching ratios of the two-body decay $b' \to b\gamma$, and of the three body decays [53] $b' \to b e^+ e^-$, $b' \to b \nu \bar{\nu}$ and $b' \to b q \bar{q}$ are expected to be smaller than $BR_{b' \to bg}$.

In this thesis, the b' mass range under study is $m_{b'} = 96 \to 103$ GeV/c^2, which means that the $b' \to cW$ and $b' \to bZ$ decays are dominant [48, 42, 43].

In figure 2.3 the branching ratios of the dominant b' decays for $R_{CKM} = 0.001$ are shown. It is possible to see that, for small values of R_{CKM} and $m_{b'} \sim m_Z$, the gluon channel can be relevant (due to phase space suppression of the $b' \to bZ$ decay). For higher b' masses (above the Z threshold and below the H threshold), the $b' \to bZ$ clearly becomes the dominant FCNC decay. When $m_{t'} = m_t$ the FCNC decays are GIM suppressed [17]. In this case, the $b' \to cW$ becomes the only relevant decay mode. For the almost degenerate case (figure 2.3a) the GIM cancelation occurs when $m_{b'} \sim m_t$. When the $m_{t'} - m_{b'}$ mass difference grows the GIM cancellation point is shifted for smaller $m_{b'}$ (figure 2.3b). Higher values of R_{CKM} favour the $b' \to cW$ decay, as can be seen in figure 2.4.

The b' decay length is expected to be below 10^{-3} cm [42]. Consequently, the b' should decay in the central region of a conventional detector.

Previous searches for b'-quarks

At LEP-I, the ALEPH [58], DELPHI [59], L3 [60] and OPAL [61] experiments performed dedicated searches for the pair production of b'-quarks ($e^+e^- \to b'\bar{b}'$), establishing the lower limit $m_{b'} > 46$ GeV/c^2. No assumptions on the branching ratios of the b' decay modes ($b' \to b\gamma$ or $b' \to bg$) were made.

In the Run-I of the TEVATRON, both the D$\emptyset$ and CDF collaborations reported limits on $\sigma(p\bar{p} \to b'\bar{b}') \times (BR_{b' \to X})^2$, where X is the chosen b' decay mode. Assuming that $BR_{b' \to bZ} = 1$, CDF found that $m_{b'} > 199$ GeV/c^2 [62] (*c.f.* figure 2.5). The D$\emptyset$ analysis dedicated to the t pair production search [63] can also be used to place limits on $\sigma(p\bar{p} \to b'\bar{b}') \times (BR_{b' \to cW})^2$ [64]. Assuming that $BR_{b' \to cW} = 1$, it is also possible to establish a lower limit of 128 GeV/c^2 on the b' mass. Both limits were derived

[7] This is true even if $m_{b'} > m_{t'}$.

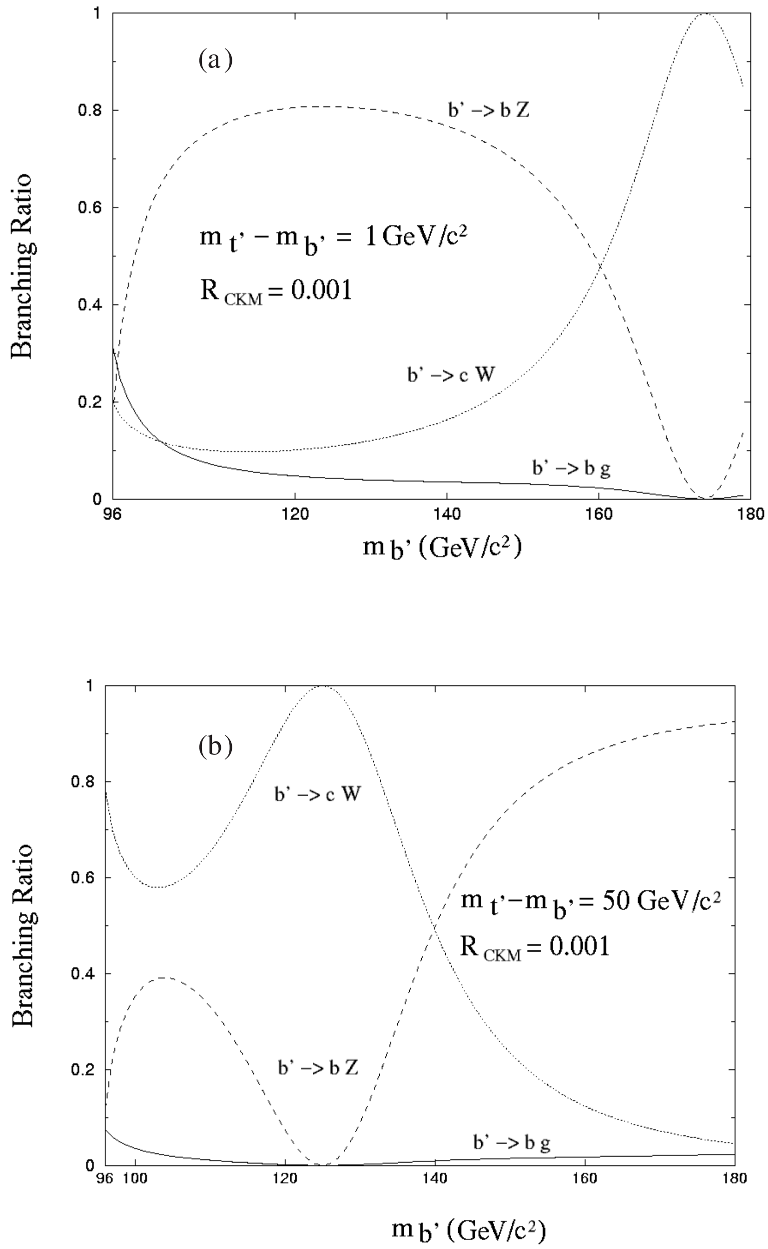

Figure 2.3: *The branching ratios of the dominant b' decays as a function of the b' mass for $R_{CKM} = 0.001$ [42] and $m_H > m_{b'} + m_b$ are shown. Two extreme cases were considered: (a) $m_{t'} - m_{b'} = 1$ GeV/c^2 and (b) $m_{t'} - m_{b'} = 50$ GeV/c^2. The dashed line corresponds to $BR_{b' \to bZ}$, the solid line corresponds to $BR_{b' \to bg}$ and the dotted line corresponds to $BR_{b' \to cW}$.*

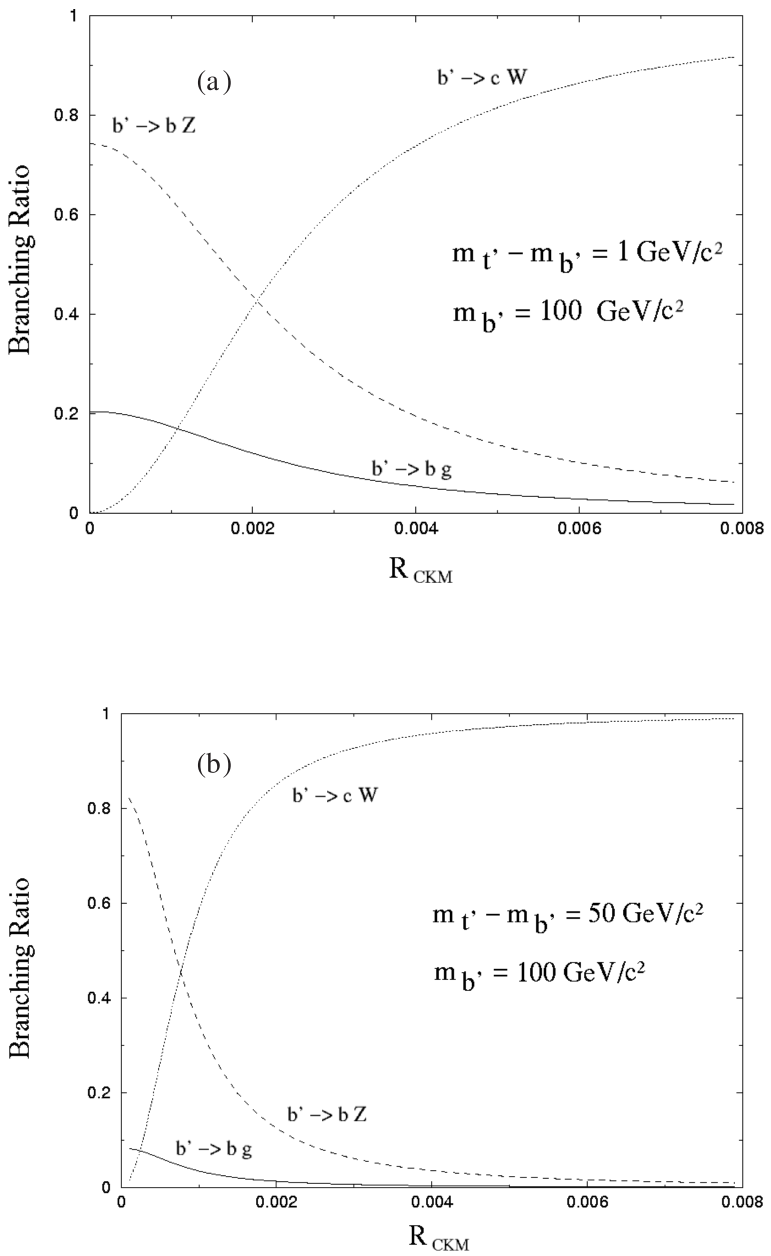

Figure 2.4: *The branching ratios of the dominant b' decays as a function of R_{CKM} for $m_{b'} = 100$ GeV/c^2 and $m_H > m_{b'} + m_b$ are shown [42]. Two extreme cases were considered: (a) $m_{t'} - m_{b'} = 1$ GeV/c^2 and (b) $m_{t'} - m_{b'} = 50$ GeV/c^2. The dashed line corresponds to $BR_{b' \to bZ}$, the solid line corresponds to $BR_{b' \to bg}$ and the dotted line corresponds to $BR_{b' \to cW}$.*

assuming that the b and c masses are negligible and that $\sigma(p\bar{p} \to b'\bar{b}') = \sigma(p\bar{p} \to t\bar{t})$.

Although the most recent results come from CDF and D∅, they suffer from the drawback of the need to assume limits on the branching ratios of the studied b' decay modes in order to be able to place limits on $m_{b'}$.

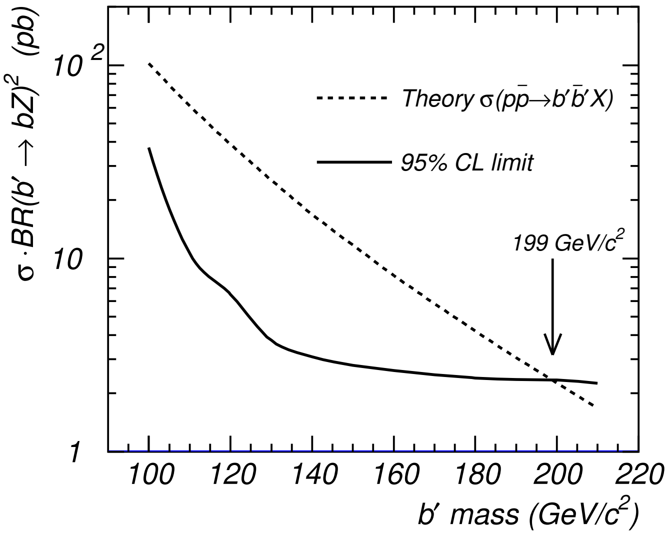

Figure 2.5: *CDF limit on $\sigma(p\bar{p} \to b'\bar{b}') \times (BR_{b' \to cW})^2$ as a function of the b' mass [62]. The theoretical prediction for $\sigma(p\bar{p} \to t\bar{t})$ is also shown (dashed line).*

Chapter 3

THE DELPHI EXPERIMENT AT LEP

In this chapter the LEP collider and the DELPHI experiment are described. In section 3.1 the LEP injection and acceleration chain are discussed. The different DELPHI subdetectors are presented in section 3.2. The chapter ends with a brief description of the data acquisition system and luminosity measurements.

3.1 The LEP collider

The Large Electron Positron collider [65, 66], LEP, was located at CERN (European Organization for Nuclear Research), near Geneva. LEP was an e^+e^- collider, which started operating in 1989 and finished in 2000. During the first phase of operation (LEP-I), data were collected at centre-of-mass energies ($\sqrt{s}$) close to the Z mass. The high statistics accumulated allowed precision studies of the SM with a high level of accuracy. In 1995, the e^+e^- centre-of-mass energy was increased to higher values, starting the LEP-II phase of operation. The aim of this phase was to continue precision studies above the W pair production threshold and also to search for new physics. The highest collision energy reached by LEP-II was around 209 GeV.

The production of high energy electrons and positrons required a complex injection and acceleration chain (figure 3.1). The electrons were produced by heating a copper filament, while the positrons were produced by the collision of 200 MeV electrons with a tungsten target. Electrons and positrons were then accelerated to 600 MeV at the Linear Injector-LEP (LIL) and accumulated in the Electron-Positron Accumulator (EPA). The beams were then injected in the Proton Synchrotron (PS) and in the Super Proton Synchrotron, being accelerated to 3.5 GeV and 20 GeV, respectively. Finally, they were injected in LEP, which had a perimeter of about 27 km and was buried at a depth varying between 50 and 175 m. It was composed by eight linear sections of 210 m on either side of the eight potential collision points, four of each housed the LEP experiments: ALEPH, DELPHI, L3 and OPAL. The acceleration of the electrons and positrons was done at the linear sections (at opposite directions), by Radio-Frequency (RF) cavities. Alternating with the linear sections, there were eight arcs, equipped with magnets, which bended and focused the beams.

Due to synchrotron radiation, the beams lost energy at each turn. The lost energy was continuously replaced by the RF system. The effect of synchrotron radiation at the detection time was reduced by placing the detectors in the linear sections.

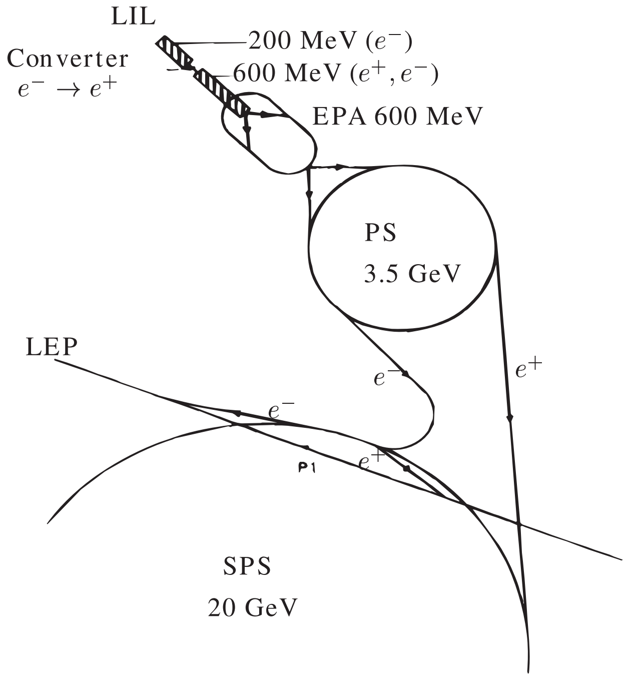

Figure 3.1: *LEP injection and acceleration chain.*

Beam particles (electrons and positrons) circulated in bunches, focused by a set of superconducting quadrupoles and sextupoles with very strong field gradients. The dimensions of such bunches were 10 μm and 250 μm in the vertical and horizontal directions, respectively.

An important parameter of LEP was the luminosity, $\mathcal{L}$, which is defined as the number of beam particles that cross the collision region per unit of area and per second. The event rate, $\frac{dN}{dt}$, for a physical process with a cross-section σ, is defined as:

$$\frac{dN}{dt} = \mathcal{L}\sigma = n_b f \frac{N_+ N_-}{S}\sigma\,, \tag{3.1}$$

where n_b is the number of bunches per cycle, $N_\pm$ is the number of positrons (electrons) per bunch in each beam, f is the revolution frequency and S is the cross-section of the bunches. The knowledge of these properties allows the determination of the LEP luminosity. The number of particles per bunch at LEP was about 10^{11}. During LEP-II, $n_b = 4$, with the interval between collisions being $\sim 22\mu$s. The typical value for the luminosity was $\sim 10^{32}(1/\mathrm{s}\cdot\mathrm{cm}^2)$.

The beam energy was measured by LEP using methods [67] relying on the effect of the dipole fields acting on the beams. The accurate measure of the magnetic field and of the bending created by it allowed the determination of the beam energy with a precision of 25 MeV.

3.2 The DELPHI detector

The DELPHI (DEtector with Lepton and Hadron Identification) was one of the four detectors located in the LEP tunnel. It was designed to allow the identification of final state particles, having a high granularity and covering as much solid angle as possible. A detailed description of the detector can be found elsewhere [68, 69]. In this thesis emphasis is put on the subdetectors directly related to the present analysis. A perspective view of DELPHI is shown in figure 3.2 and a longitudinal profile of one quarter of the detector is represented in figure 3.3.

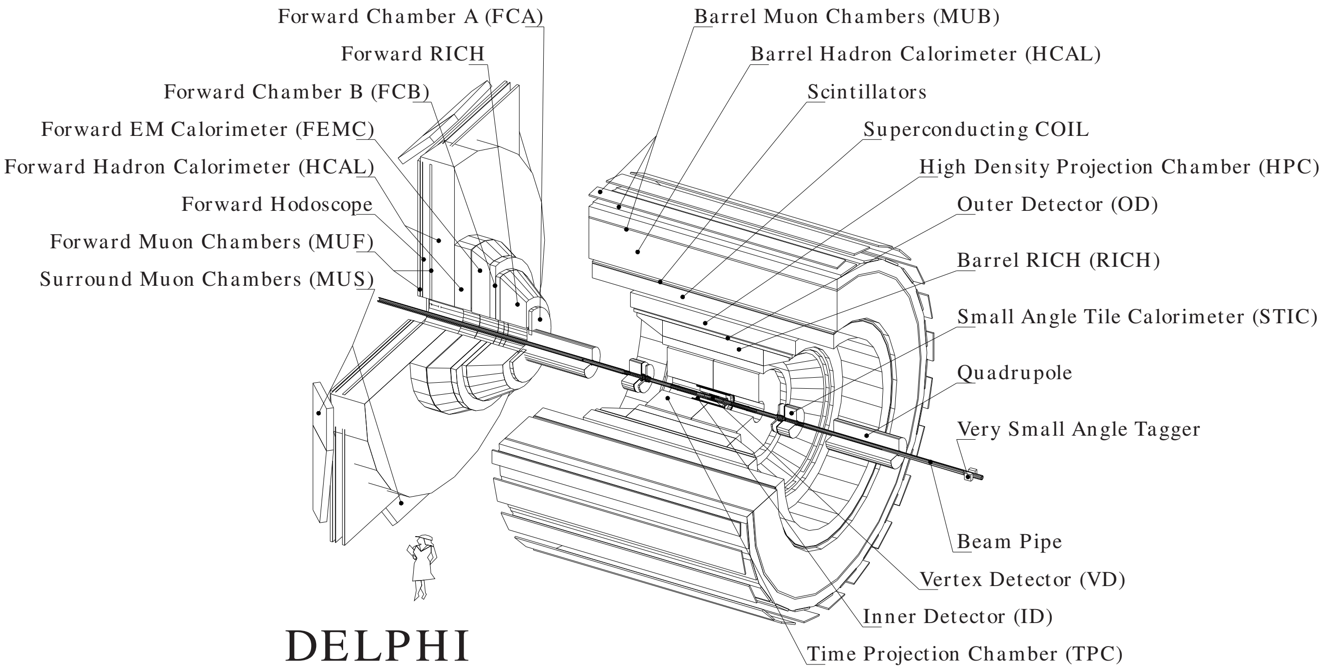

Figure 3.2: *A perspective view of the DELPHI detector (adapted from [69]). The layout of the barrel region and one of the endcaps is shown.*

DELPHI was composed by a cylinder (barrel region) and two endcaps in the forward regions of the detector. In the DELPHI coordinate system (figure 3.4), the z axis follows the direction of the electron beam, the x axis points to the center of LEP and the y axis points upwards. The radial coordinate, R, is given by $\sqrt{x^2+y^2}$. The polar angle, represented by θ, is defined with respect to the z axis and the azimuthal angle is represented by ϕ. The barrel region covers polar angles above $40°$ and below $140°$.

3.2.1 Subdetector layers

The DELPHI detector was composed by several subdetectors, organized in layers. It covered almost the full solid angle (down to $\theta \sim 3°$) and was designed to allow the reconstruction of the physical properties of the final state particles. According to the polar angle, the barrel and forward regions were defined. The different subdetector layers relevant to the present analysis are:

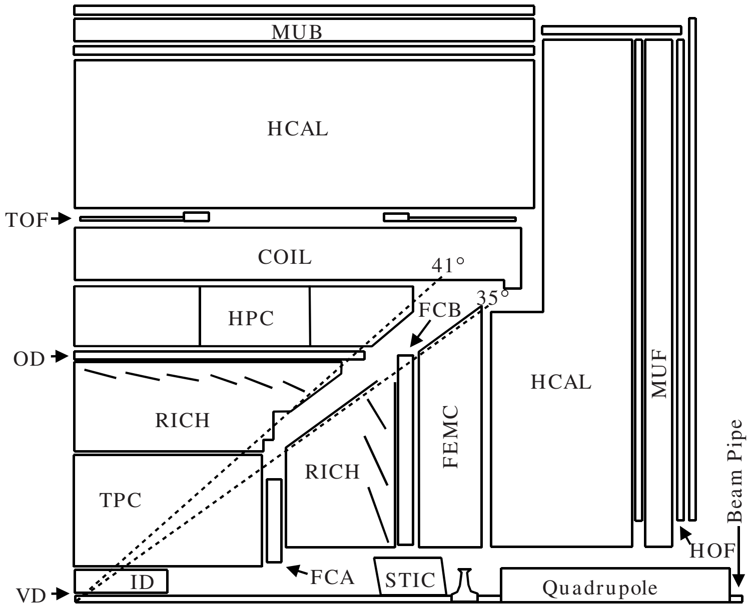

Figure 3.3: *A longitudinal profile of one quarter the DELPHI detector (adapted from [68]).*

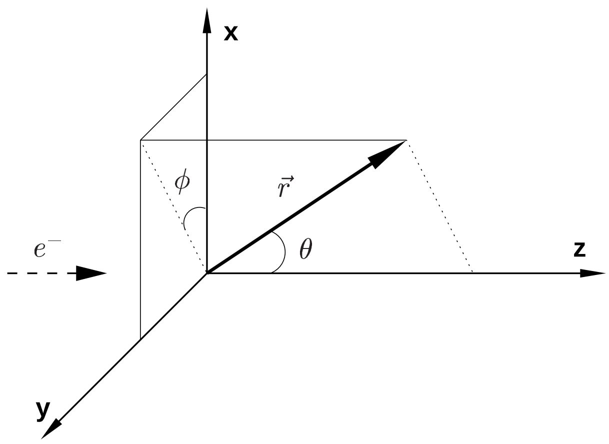

Figure 3.4: *The DELPHI coordinate system is represented. The z axis follows the direction of the electron beam and the x axis points to the center of LEP.*

- the tracking detectors (VD, ID, TPC, OD, FCA, FCB, MUB, MUF and MUS), which measured the trajectories, momenta, charges and ionization losses;
- the ring imaging Čerenkov detectors (RICH), which allowed the particle identification through the Čerenkov radiation produced by charged particles traveling with a velocity greater than the speed of light in the media;
- the time of flight detectors (TOF and HOF), which had a fast response, being useful to trigger the data acquisition systems;
- the electromagnetic calorimeters (HPC, FEMC and STIC), which measured the energy of electrons and photons;
- the hadron calorimeters (HCAL), which measured the energy of hadrons;

All the four LEP detectors had a similar structure. Nevertheless, DELPHI main vocation was the particle identification, being the only one to have a RICH. The RICH subdetectors were located in both the barrel and the forward regions.The Čerenkov photons are emitted at a fixed angle which is a function of the charged particle velocity and of the media refraction index. The RICH was composed by two different radiator materials (liquid and gas) in order to be sensitive to different ranges of momentum. For some momentum ranges the RICH information was complemented by the Time Projection Chamber (TPC) measurements.

Tracking

The tracking devices were used in the reconstruction of the trajectories of charged particles. A superconducting solenoid (COIL) produced a magnetic field, parallel to the beam pipe (z axis) and with an intensity of 1.2 T, which curved the charged particles trajectories according to its momentum and charge. The COIL, with a length of 7.4 m and an inner diameter of 5.2 m, surrounded the barrel tracking devices, the forward tracking chambers and the electromagnetic calorimeters (barrel and forward).

The DELPHI tracking system was segmented into several subdetectors, briefly described below. Their contribution to the track spatial resolution is summarized in table 3.1.

- **Vertex detector (VD)**
  The VD was located near the interaction point, covering the polar angle region between 25° and 155°. It was a silicon strip detector with an inner radius of 5.6 cm, composed by three coaxial cylindric layers, each one with 24 azimuthal sectors. The VD provided $R\phi$ and z information. Due to the superposition of the VD sectors, a maximum of 6 $R\phi$ measurements per charged track could be attained. Although all VD layers provided $R\phi$ information, only the first and third layers allowed z measurements. The VD $R\phi$ single hit resolution was $\sim 7.6\,\mu$m. The single hit precision for the z coordinate depended on the incidence angle of the track, attaining a maximum of $\sim 9\,\mu$m for perpendicular tracks.

barrel	R (cm)	θ coverage (°)	hit resolution (μm)
VD	6.3, 9.0, 10.9	> 25	7.6 ($R\phi$), 9 (z)
ID	12 to 23	> 15	50 ($R\phi$), 1.5 mrad (ϕ)
TPC	40 to 110	> 20	250 ($R\phi$), 880 (Rz)
OD	197 to 206	> 42	110 ($R\phi$), 3.5 cm (z)
forward	$\|z\|$ (cm)	θ coverage (°)	hit resolution (μm)
FCA	~ 160	11 to 32	290 (xy), 8.5 mrad (θ), 24 mrad (ϕ)
FCB	~ 275	11 to 36	150 (xy), 3.5 mrad (θ), $4/\sin\theta$ mrad (ϕ)

Table 3.1: *Spacial resolution of the tracking subdetectors [70]. The location and polar angle coverage (the complementary polar angle coverage is assumed) are also shown.*

- **Inner detector (ID)**
  The ID was divided into two distinct parts: the inner part, which was a drift chamber, and the outer part, composed by Multi Wire Proportional Chambers (MWPC). It covered the polar angles between 15° and 165°. The ID had a fast readout time ($\Delta t < 3\ \mu$s), which enabled it to participate in the first level of the trigger. The resolutions of the ID for charged tracks were $\sigma(R\phi) \sim 50\ \mu$m and $\sigma(\phi) \sim 1.5$ mrad.

- **Time projection chamber (TPC)**
  The TPC was the DELPHI main tracking device. It allowed the measurement of the most precise three dimensional position information for the reconstruction of the trajectories of the charged particles. The TPC was a cylindric drift chamber with an inner radius of 0.35 m and outer radius of 1.11 m, covering the polar region $20° < \theta < 160°$. It was filled with a gas mixture (80% of argon and 20% of methane) at a pressure of 1 atm. Electrons and positive ions produced in the gas ionization due the incoming charged particles, were drifted away toward the extremities of the TPC under the effect of an electric field. The single point precision for charged tracks was ∼250 μm in the $R\phi$ plane and ∼880 μm in the Rz plane. The TPC also allowed the measurement of the energy lost by ionization, dE/dx.

- **Outer detector (OD)**
  The OD consisted of five layers of drift tubes, located two meters away from the interaction point in the polar angle region $42° < \theta < 138°$. The OD $R\phi$ resolution was $\sim 110\ \mu$m. The longitudinal position measurement had a $\sigma(z) \sim 3.5$ cm and a fast readout time, which enabled the OD to participate in the first level of the trigger.

- **Forward chambers (FCA and FCB)**
  The Forward Chambers A and B were located in the DELPHI endcaps, on each end of the TPC. They were essentially sets of drift tubes. The FCA and FCB covered the polar angle regions $11° < \theta < 32° \ \vee\ 148° < \theta < 169°$ and $11° < \theta < 36° \ \vee\ 154° < \theta < 169°$, respectively.

- **Muon chambers (MUB, MUF and MUS)**
  The Muon Chambers are the DELPHI most external layer of subdetectors. They were drift chambers, designed to detect the passage of muons, which were the only particles able to reach and give signal at these subdetectors.

The track momentum resolution depended on the characteristics of the different subdetectors used for the reconstruction and it was lower in the forward region. The momentum measurement resolution for muons with $p = 45.6$ GeV/c (from the $Z \to \mu\mu$ decay) is summarized in table 3.2.

θ coverage (°)	detectors	$\sigma(1/p)$ (GeV/c)$^{-1}$
≥ 42	VD, ID, TPC and OD	0.6×10^{-3}
≥ 42	ID, TPC, and OD	1.1×10^{-3}
≥ 42	VD, ID, and TPC	1.7×10^{-3}
25 to 36	VD, FCB and TPC	1.3×10^{-3}
25 to 30	FCB and (TPC, FCA)	1.5×10^{-3}
< 25	FCB and (TPC, FCA)	2.7×10^{-3}

Table 3.2: *Momentum measurement resolution for 45.6 GeV/c muons in different polar angle regions [69].*

Calorimetry

The calorimeters measured the energy depositions of the charged and neutral particles. The DELPHI calorimeters were: the barrel (HPC) and forward (FEMC and STIC) electromagnetic calorimeters and the hadron calorimeter (HCAL). They were designed to have a high granularity, giving detailed position information. In opposition to the tracking devices, where the charged particles interacted with the low density media without loosing much of their energy, the calorimeters were made of very dense materials. Therefore, both charged and neutral particles may be fully stopped inside the calorimeters and their energy could be entirely contained in the detector[1]. In the DELPHI electromagnetic calorimeters, the photons converted into e^+e^- pairs with the subsequent radiation of photons by the electrons. The multiplication of such processes originated a cascade with the final state particles having a small energy. Hadrons were also able to cross the electromagnetic calorimeters, reaching the much larger hadron calorimeters, where their energy was deposited through nuclear interactions with the detectors media. The energy and spatial resolutions of the calorimeters are shown in table 3.3.

barrel	θ coverage (°)	$\sigma(E)/E$ ($[E]$ = GeV)	spatial resolution
HPC	> 42	$0.043 + 0.62/\sqrt{E}$	1.0 mrad (θ), 1.7 mrad (ϕ)
HCAL	> 43	$0.21 + 1.12/\sqrt{E}$	2.96° (θ), 3.75° (ϕ)
forward	θ coverage (°)	$\sigma(E)/E$ ($[E]$ = GeV)	spatial resolution
FEMC	8 to 35	$0.052 + 0.27/\sqrt{E} + 0.11/E$	0.5 cm
STIC	3 to 11	$0.015 + 0.135/\sqrt{E}$	0.25 mm to 1.20 mm
HCAL	11 to 48	$0.21 + 1.12/\sqrt{E}$	2.62° (ϕ)

Table 3.3: *Energy and spatial resolution of the electromagnetic and hadron calorimeters [70]. The polar angle coverage (the complementary polar angle coverage is assumed) is also shown.*

[1] In fact, muons are essentially the only detected particles which were not fully stopped in the calorimeters, reaching the outermost part of DELPHI.

- **High density projection chamber (HPC)**
  The HPC was located in the barrel region of DELPHI ($42^\circ < \theta < 138^\circ$), with an inner and outer radius of 208 cm and 260 cm, respectively. It was a sampling calorimeter, composed by lead and by a gaseous mixture.

- **Forward electromagnetic calorimeter (FEMC)**
  The FEMC was a homogeneous and highly segmented calorimeter, formed by blocks of leadglass having the shape of truncated pyramids and disposed in order to be almost projective to the interaction point. It was placed in the DELPHI forward region, covering the angular region $8^\circ < \theta < 35^\circ$ and the complementary region $145^\circ < \theta < 172^\circ$. The Čerenkov light produced by the particles crossing the FEMC was read by triodes.

- **Small angle tile calorimeter (STIC)**
  The STIC was the DELPHI luminosity monitor [71, 72] and was designed to have a high accuracy ($\sim 0.1\%$). It was a lead scintillator calorimeter, composed by two cylindric detectors placed on each side of the beamspot (covering the angular region $3^\circ < \theta < 11^\circ \vee 169^\circ < \theta < 177^\circ$). The light produced in the scintillator was readout by wavelength shifter fibers.

- **Hadron calorimeter (HCAL)**
  The HCAL was installed in the return yoke of the DELPHI magnet. It was divided in two endcaps and a barrel region, covering almost the full solid angle (the polar angle coverage was $11^\circ < \theta < 169^\circ$). It was an iron/gas sampling calorimeter. The iron was also used as return yoke of the solenoid.

3.2.2 Hermiticity

The characterization of the final state particles required a detector as hermetic as possible. In fact, the experimental signature of processes with neutrinos in the final state was the presence of missing energy and momentum in the events.

DELPHI covered almost 90% of the solid angle, with the region around the beam pipe ($\theta < 2^\circ$ and $\theta > 178^\circ$) being totally uncovered. The barrel and the forward electromagnetic calorimeters were separated by a gap in polar angle roughly corresponding to $35^\circ < \theta < 40^\circ$ (*c.f.* figure 3.3). This was the region of passage of the cables which allowed the readout of the internal detectors. Furthermore, the region $\theta \sim 90^\circ$ was not fully covered by the majority of the detectors, since the supports of several detectors and cabling were passed through it. Most of these regions were covered by part of the tracking devices and by the hadron calorimeter, enabling the detection of charged particles and hadrons. However, the ability to detect photons was severely reduced. Therefore, a supplementary set of photons taggers (lead-scintillator counters), was installed. They covered the $\theta \sim 40^\circ$ and the $\theta \sim 140^\circ$ regions, as well as the region were the two hemispheres of the HPC met ($\theta \sim 90^\circ$). Additionally, the azimuthal angle regions not fully covered by the TOF, due to obstruction from the supports of the COIL, were covered by the ϕ *taggers*, which were lead-scintillator counters placed behind the azimuthal divisions of the HPC modules ($\phi \sim 7.5^\circ + (n-1)15^\circ$, with $n = 1, \ldots, 24$).

3.2.3 Data taking and trigger

The DELPHI data taking was performed using three different systems: the Data Acquisition System (DAS) [73], the Slow Control system (SC) [74] and the Quality Checking system (QC) [75, 76]. The DAS was responsible for the full chain of data taking, including the trigger modes and LEP status. The SC was responsible for monitoring, at each time, the status of the different subdetectors and of the connections between them. The QC was intended to do a first check on the detector working conditions and on the data quality.

The goal of the trigger system [77] was to choose, at each beam crossing (every 22 μs), the potentially interesting events, reducing the flux of data to be stored. It was designed in order to maximize the efficiency for the known physics, keeping at the same time a high sensitivity to new physics phenomena. The trigger system was divided into four levels, with the fist two working in real time. The fist level of trigger was based on fast response of the ID, OD, FCA, FCB, TOF and HOF detectors, while the second used the slower detectors like the TPC, HPC and MUF. The event rate was further reduced by the third and fourth levels, which were software filters, asynchronous with the beam crossing. The third level of trigger was designed to reduce the number of accepted events using more stringent constraints on the tracking detectors and sharper threshold settings. The function of the fourth trigger level was to reject, before data logging, the events which passed the previous levels but contained reduced physics informations.

3.2.4 Luminosity measurement

The luminosity was measured at DELPHI by counting the number of events from the Bhabha scattering ($e^+e^- \rightarrow e^+e^-$) at small angles [71, 72], dominated by the t-channel exchange of a photon. This process was chosen due to its clear experimental signature (two energetic leptons) and to the small theoretical errors associated with its cross-section evaluation. The integrated luminosity, for a given period, was obtained in the following way:

$$\mathcal{L} = \int_{\delta t} L(t) = \frac{N_{Bhabha}}{\sigma^{eff}_{Bhabha}} , \tag{3.2}$$

with N_{Bhabha} being the measured number of Bhabha events and σ^{eff}_{Bhabha} being the theoretical cross-section for this process convoluted with the detection efficiency and geometrical acceptance considered. The precision of the luminosity measurement by DELPHI at LEP-II was $\sim 0.1\%$.

3.2.5 Analysed data samples

The data analysed in this thesis were collected by the DELPHI detector during the LEP-II phase, in the years 1999 and 2000. The centre-of-mass energy ranged from 196 GeV to 209 GeV, corresponding to an integrated luminosity around 420 pb^{-1}.

The 1999 runs were set to well defined centre-of-mass energies. In 2000, the beam acceleration was done in finner steps, which allowed to get the increase of the energy as the beam intensity decreased, instead of running LEP at a previously defined centre-of-mass energy. A significant part of the collected data was taken at $\sqrt{s}$ beyond the planned scope of LEP. In the final period of the year 2000 run, DELPHI suffered from a problem which affected one sector of the TPC (corresponding to 1/12 of the acceptance). This required modifications on the track reconstruction [78] and these data were analysed separately.

The analysed data were divided into six energy bins. The luminosity corresponding to each bin is shown in table 3.4.

year	1999			2000		
label	196	200	202	205	207	206*
$\langle\sqrt{s}\rangle$ (GeV)	195.5	199.5	201.6	204.8	206.6	206.3
luminosity (pb^{-1})	76.0	82.7	40.2	80.0	81.9	59.2

Table 3.4: *Luminosity collected with the DELPHI detector at each centre-of-mass energy. The data collected during the year 2000 with the TPC fully operational were split into two energy bins, below and above* $\sqrt{s} = 206$ GeV*, with* $\langle\sqrt{s}\rangle = 204.8$ GeV *and* $\langle\sqrt{s}\rangle = 206.6$ GeV*, respectively. The energy bin labeled 206* corresponds to the data collected with a sector of the TPC turned off.*

3.2.6 Event reconstruction

The first step of the data analysis was the processing of the information from the different subdetectors, in order to identify and reconstruct the physical properties of the final state particles. The raw data stored by the DAS and the simulated events[2] were processed by DELANA [79], a dedicated event reconstruction program. The output stream of DELANA was the Data Summary Tape (DST), conceived to have a reduced amount of data.

At a first stage, DELANA reconstructed the local information from each subdetector. The output of this level was a point in the $(R\phi, Rz)$ plane (*e.g.* from VD), a energy depositions in the calorimeters or partially reconstructed tracks (*e.g.* from TPC). This information was used in the global track reconstruction, leading to the vertex reconstruction and to the final state particles identification.

The data structure used by DELANA to store information of the different reconstruction steps was TANAGRA (Track ANAlysis and GRAphics) [80]. This structure was also the input of the DELPHI event display code, DELGRA (DELphi GRAphics program) [81], which allowed the 3-dimensional visualization of the event topology and of each of the subdetectors.

[2]Monte Carlo simulation of signal and SM background processes will be discussed in chapter 4.

Track reconstruction

The track search algorithm used for the barrel region used a track segment seen in the TPC and extrapolated it inwards and outwards to find compatible track elements in the ID and OD subdetectors, respectively. In the TPC sector divisions (or in the TPC dead sector for the 2000 data taking [78]) the ID and OD track elements were directly connected in order to recuperate tracks that would otherwise be lost. In the forward region, the track elements seen in the TPC could not be used as first search hypothesis. In this case the FCB and beamspot[3] information was used to define the initial hypothesis for the track reconstruction.

After this initial hypothesis, track candidates were fitted together with the information from the remaining tracking subdetectors and from the RICH. In addition, the fitted tracks were then extrapolated into the VD inwards and into the muon chambers outwards. At this point, all the VD hits were associated to the tracks. If the tracks had very low energy, they were bended inside the magnetic field and did not reach the TPC. In this case the direct association of the ID and VD track elements was performed [82].

Leptons, photons and hadrons identification

The particle identification was done combining information from the tracking devices, calorimeters (both electromagnetic and hadronic) and muon chambers. The identification of low momentum leptons was done through the measurement of the dE/dX (TPC) and Čerenkov angles (RICH), which provided direct information on which particle was present in the event.

Electron and photon identification was based on the REMCLU [83] package. In the barrel region, electrons were seen as tracks with an associated shower in the HPC and almost no shower in the HCAL. The ratio between the energy deposited in the HPC, E_{em}, and the track momentum, p, is expected to be ~ 1, independently of the electron energy. Another important information was the spatial compatibility of the reconstructed tracks and the shower[4], which was used to determine if an energy deposition should be associated to a neutral particle (in this case the energy deposition was called neutral) or to a track.

Similarly to electrons, photons were expected to originate showers in the HPC, with almost no energy depositions in the HCAL. The main difference between electrons and photons is that the energy depositions in the HPC are associated to reconstructed tracks in the electron case. On the contrary, neutral energy depositions in the HPC above 500 MeV unassociated to charged tracks were considered photon candidates. The HPC shower profile also provide discrimination between photons and other particles. For each photon candidate, the longitudinal and transverse profile of the HPC shower was analysed. In particular, in the shower transverse development, the dispersion of the energy deposits, must not present the double-peak structure

[3] The beamspot information is used as a constraint imposing that the track origin should be near the interaction point.

[4] This was done by a pattern recognition algorithm, which extrapolated the reconstructed particle and compared this information with the HPC shower (called electromagnetic shower) reconstruction [69].

characteristic of the $\pi^0 \to \gamma\gamma$ decay. In the forward region, the electron and photon identification relied on the information from the FEMC and STIC subdetectors.

Due to detector limitations, some photons and electron candidates did not fulfill all the identification criteria. In order to improve detection efficiency, candidates not passing a tighter selection could still be recovered. Photons converted into e^+e^- pairs[5], and therefore having two associated tracks, could still be considered photon candidates in the looser selection, although tighter selection required the absence of track elements associated to the electromagnetic energy deposit. According to a misidentification probability assigned to the candidate by the REMCLU [83], it was classified as *tight* or *loose*. This misidentification probability was related with the χ^2 of the fit to the data, assuming the electron or photon hypothesis.

Muons and charged hadrons had almost no energy depositions in the electromagnetic calorimeters[6]. As most of the hadrons originated showers in the hadron calorimeters and the muons had a very small energy deposition there, it was possible to distinguish them. The iron of the hadron calorimeters provided a first level of separation between hadrons and muons: most of the hadrons were stopped by this material, whereas all muons with momenta above 2 GeV/c were expected to penetrate the Muon Chambers (MUB, MUF or MUS). For the muon candidates, the ratio between the energy deposited in the hadron calorimeters, E_{had}, and the associated track momentum, p, was expected to be less than 0.1, while $E_{em}/p \sim 0$.

The association of the Muon Chambers hits to the reconstructed tracks is done with the EMMASS [84] package. Muon classification is done with the MUFLAG [85] package. For each of the muon candidates, a fit of the reconstructed track and the muon chamber hits is done. The χ^2 of the fit is used to classify the accepted muon candidates as *very loose*, *loose*, *standard* or *tight*.

[5] About 40% of the photons convert before they reach the HPC and about 7% of them convert in front of the TPC, originating visible tracks.

[6] This applies to charged hadrons with a decay length large enough. If they decayed near the interaction point, its identification had to be done through the analysis of the particles originated in the decay. In this case, information on secondary vertex was also used.

Chapter 4

MONTE CARLO SIMULATION

In order to identify new physics, the knowledge of the physical properties of the particular process under study (the signal) and of the SM background processes is required. For such purpose, event generators based on Monte Carlo techniques were used to generate signal and background events. These events were then passed through the full DELPHI detector simulation. This chapter is organized as follows: in section 4.1 the signal generator is presented, while the background processes and the corresponding generators are discussed in section 4.2. The DELPHI detector simulation is briefly described in section 4.3.

4.1 Signal events

Signal event samples, corresponding to the pair production of b'-quarks at LEP ($e^+e^- \to b'\bar{b}'$), were generated with PYTHIA 6.200 [86]. The angular distributions assumed for the b' pair production and subsequent decay were those predicted by the SM for any heavy down-type quark [42].

The FCNC $b' \to bZ$ decay and the CC $b' \to cW$ decay were considered. Although PYTHIA allows the $b' \to cW$ decay in a straightforward way, it does not provide the FCNC decay channel for quarks. This decay had to be implemented in the code, according to the expected theoretical distributions (*c.f.* chapter 2). The polar angles of the b' in the laboratory frame and of the b in the b' rest frame at generator level are shown in figure 4.1. The reconstructed mass of the Z boson is also shown.

Initial state radiation (ISR) and final state radiation (FSR) corrections were taken into account, as their contribution is important for the cross-section evaluation and for the generated event kinematics. ISR was implemented as pure QED corrections while FSR corrections also included QCD corrections. In figure 4.2 the effect of the ISR and FSR corrections on the b' pair production cross-section at LEP is shown, for $m_{b'} = 100$ GeV/c^2, as a function of the centre-of-mass energy. The Born level cross-section and the radiative corrections were computed with PYTHIA and are in agreement with the theoretical SM calculations [42].

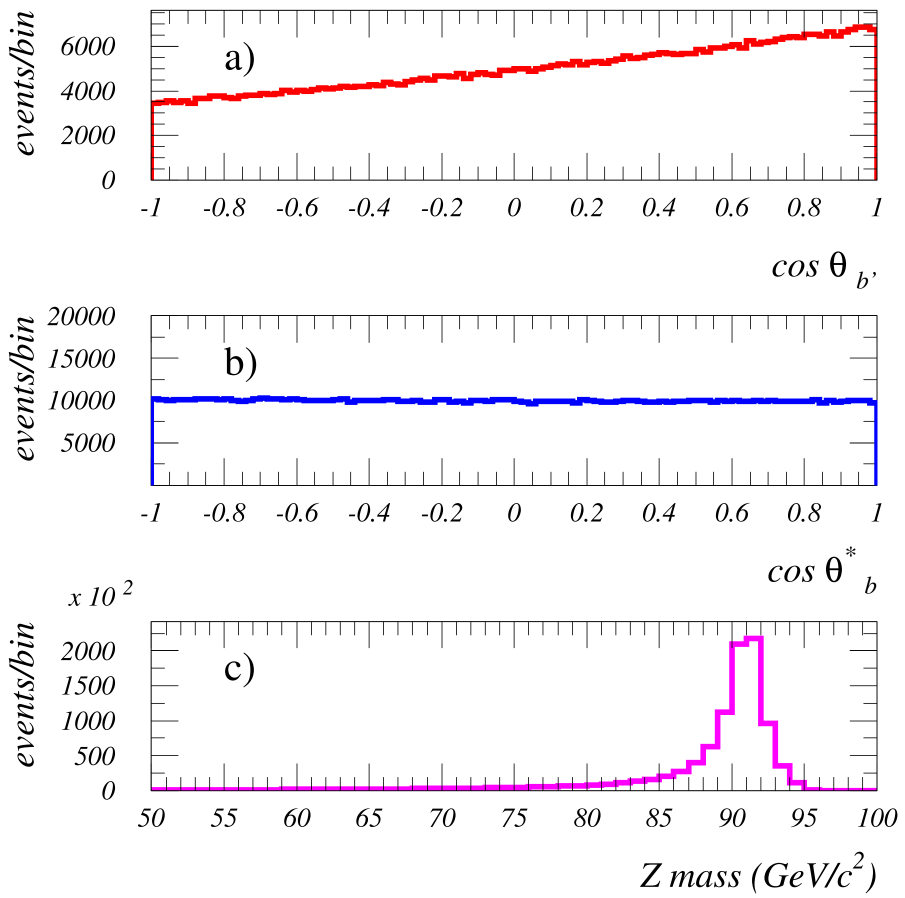

Figure 4.1: *Distributions of relevant variables at the generator level for the FCNC $b' \to bZ$ decay channel are shown: (a) cosine of the polar angle of the b' in the laboratory frame, (b) cosine of the polar angle of the b in b' rest frame and (c) reconstructed mass of the Z boson. For these plots 500 000 events were generated with $m_{b'} = 100$ GeV/ c^2 and $\sqrt{s} = 205$ GeV.*

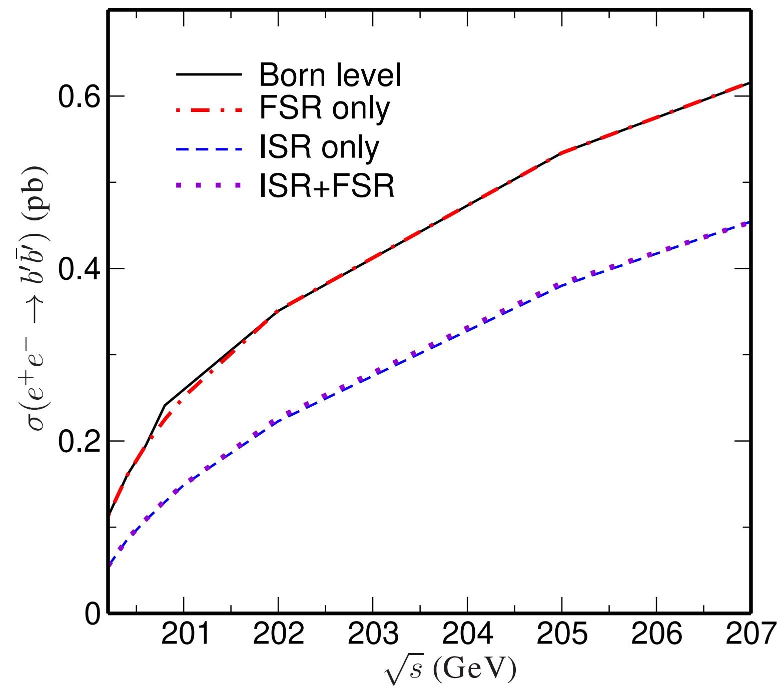

Figure 4.2: *Cross-sections for the pair production of b'-quarks at LEP ($m_{b'}$ = 100 GeV/c^2) as a function of the centre-of-mass energy, according to PYTHIA 6.200. The effect of the initial (ISR) and final (FSR) state radiation corrections is shown.*

The $e^+e^- \to b'\bar{b}'$ production cross-sections as a function of the b' mass and centre-of-mass energy are shown in figure 4.3. The effect of both ISR and FSR corrections was taken into account.

Different samples of $e^+e^- \to b'\bar{b}'$ events were generated for different b' mass, decay channel ($b' \to cW$ or $b' \to bZ$), centre-of-mass energies and decays of the Z and W bosons. A characteristic common to all the events final states is the presence of, at least, two jets, which were originated by the c (b) quarks present after the decay $b'b' \to cWcW$ ($b' \to bZbZ$).

4.2 Background events

The background for any search for new physics beyond the SM corresponds to the SM processes. The most relevant background processes for the present analyses are those leading to topologies with several charged tracks. At typical LEP-II energies, such processes are, according to the SM, WW, $q\bar{q}$ and ZZ (figures 4.4a, b and c). Although less important, the $e^+e^- \to e^+e^-$hadrons events (henceforth named "$\gamma\gamma$" and represented in figure 4.4d) and Bhabha events ($e^+e^- \to e^+e^-$) were also considered. The cross-sections corresponding to the most relevant SM processes at LEP are shown in figure 4.5. The ISR and FSR effects were taken into account. In the case of the pair production of quarks through a Z boson exchange, the radiative corrections

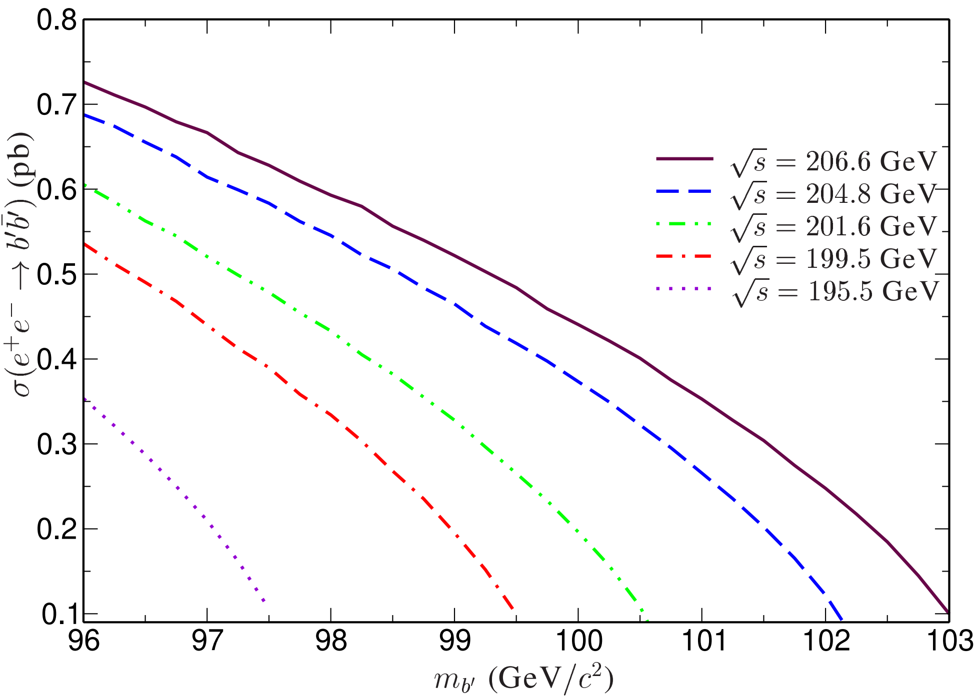

Figure 4.3: *Cross-sections for the pair production of b'-quarks at LEP as a function of the b' mass and centre-of-mass energy, according to PYTHIA 6.200. Both initial and final state radiation corrections were taken into account.*

are particularly important ($e^+e^- \to q\bar{q}\gamma$). In this case, a hard photon with energy

$$E_\gamma = \frac{s - m_Z}{2\sqrt{s}} \tag{4.1}$$

can be produced, leading to effective centre-of-mass energies, $\sqrt{s'}$, close to the Z peak.

Background events were generated with several Monte Carlo programs. Both the neutral (ZZ) and charged (WW) currents four-fermion final states were generated with WPHACT [88]. "$\gamma\gamma$" events were generated using WPHACT and PYTHIA [89]. The $q\bar{q}(\gamma)$ final state was generated with KK2F [90]. Bhabha events were generated with BHWIDE [91].

4.3 Detector simulation

In order to compare the generated samples with the real data, the detector effects have to be taken into account. The code performing the DELPHI detector simulation is DELSIM (DELphi SIMulation program) [92], which contains a description of the geometry, material composition and operation efficiency of the detector. This program simulates the interation of the simulated particles with the various subdetectors and its main purpose is to digitalize the DELPHI detector response to the generated events. Data structures similar to raw data were obtained and subsequently processed with the DELPHI reconstruction program (DELANA, which was described in chapter 3, section 3.2.6).

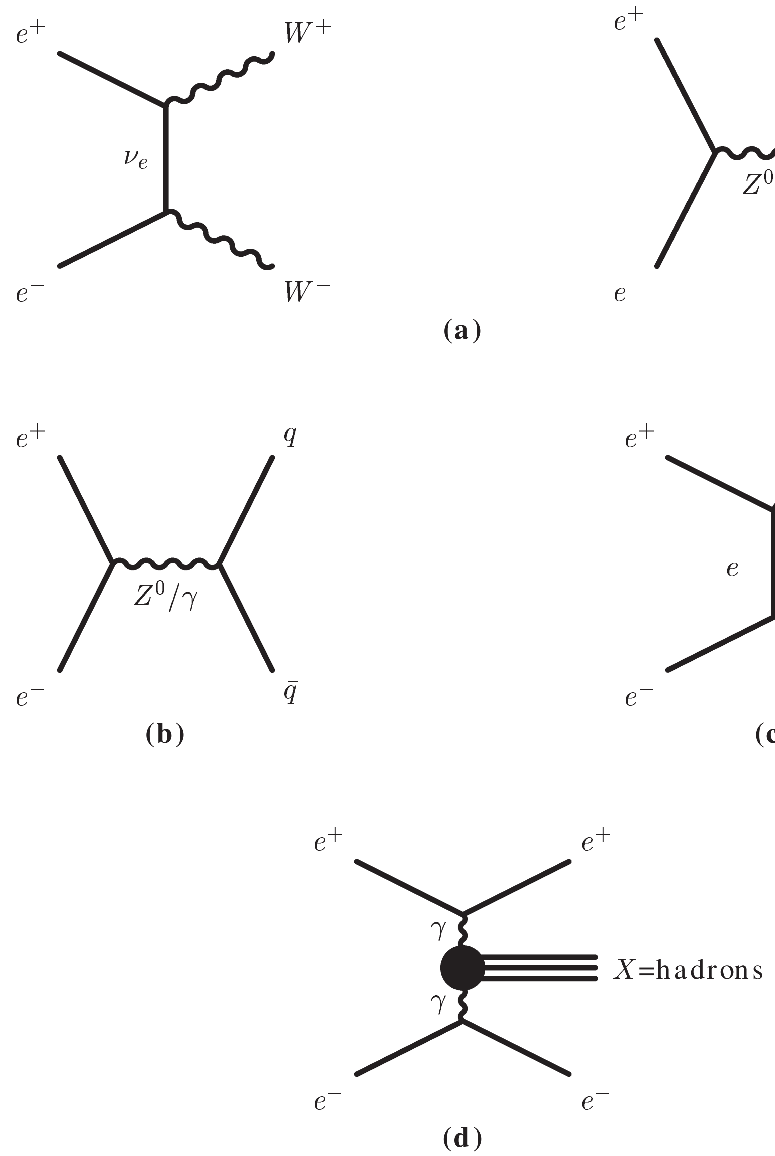

Figure 4.4: *The lowest order Feynman diagrams corresponding to the most relevant SM processes are shown. The (a) WW, (b) $q\bar{q}$, (c) ZZ and (d) "$\gamma\gamma$" processes are represented.*

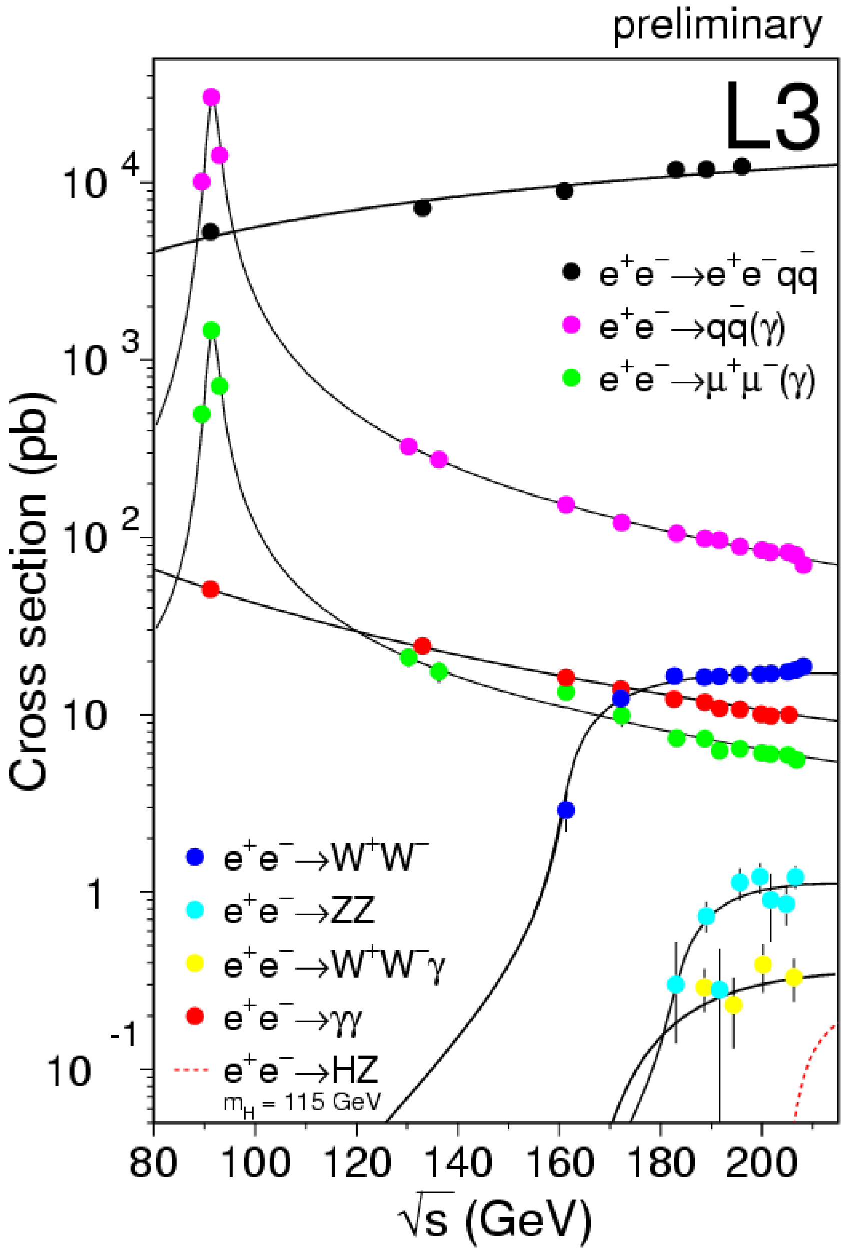

Figure 4.5: *Cross-sections of typical Standard Model processes at LEP as a function of the centre-of-mass energy, measured by the L3 collaboration [87]. The SM predictions are also shown.*

Chapter 5

DATA ANALYSIS

Data and simulated events can be characterized in a topological way according to the number of jets, isolated leptons and photons present in the final states. In this chapter, the criteria used to select the different topologies associated to the physical channels under study are described. The definition of a common basic event selection (preselection) is presented in section 5.1. In section 5.2, the assignment of each event to a specific topology is discussed. The specific analyses for each topology are presented in section 5.3.

5.1 Common analysis criteria

The $b' \to cW$ (CC) and $b' \to bZ$ (FCNC) decay modes and the subsequent decays of the gauge bosons (W or Z) originate several different final states (*c.f.* figure 5.1). According to the number of jets[1], isolated leptons and photons, different topologies can be defined. The topologies under study and the branching ratios (BR) of the associated bosons decays are summarized in table 5.1. About 81% (90%) of the total branching ratio of the FCNC (CC) channels was covered.

b' decay	bosons decay	BR (%)	topology
$b' \to bZ$ (FCNC)	$ZZ \to ll\nu\nu$	4.0	$bbll\nu\nu$
	$ZZ \to qq\nu\nu$	28.0	$bbqq\nu\nu$
	$ZZ \to qqqq$	48.6	$bbqqqq$
$b' \to cW$ (CC)	$WW \to qql\nu$	43.7	$ccqql\nu$
	$WW \to qqqq$	45.8	$ccqqqq$

Table 5.1: *The different topologies under study and associated branching ratios. The charged leptons are represented by l and the neutrinos by ν. The jets originated by the hadronization of a generic quark are represented by q, while b (c) stands for a b-quark (c-quark) jet.*

[1] Due to hadronization, the quarks originate jets in the final state.

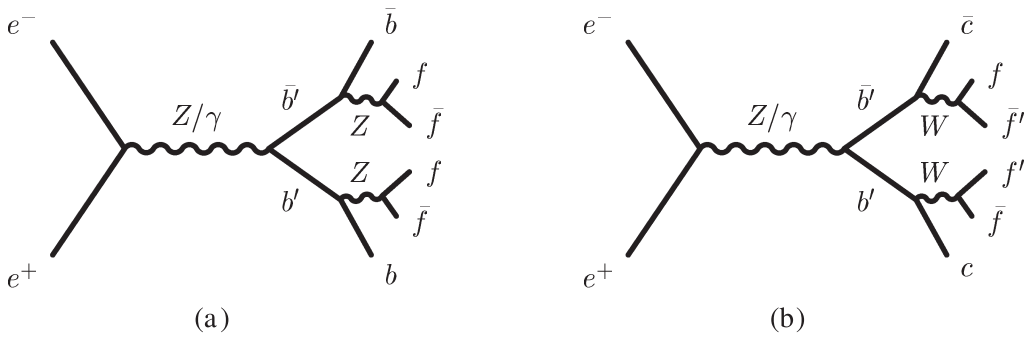

Figure 5.1: *Feynman diagrams corresponding to the pair production of b'-quark at LEP for the (a) FCNC and (b) CC decay modes.*

5.1.1 Isolated charged particles and clusters

The $bbll\nu\nu$ and $ccqql\nu$ topologies are characterized by the presence of energetic isolated leptons from the leptonic decays of the Z or W bosons. Due to electromagnetic radiative decays of unstable particles and QED *bremsstrahlung*, it is also possible to find isolated photons in the selected events.

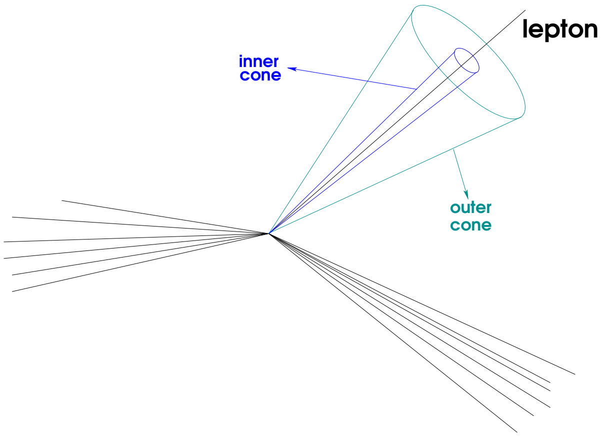

Figure 5.2: *Schematic representation of the double cone structure used to determine the isolation of a charged particle in the event.*

In order to search for isolated particles a method which does not depend on the event topology was used. In this method, a double cone was constructed around each particle (*c.f.* figure 5.2): the energy of the inner cone was considered associated to the particle, while isolation was ensured by requiring the energy between the two cones to be below a certain value. Isolated leptons (photons) were defined by cones centered around the axis of the charged particle track (neutral cluster) and with half opening angles of 5° and 25° (5° and 15°). The average energy density in the region between the two cones had to be below 150 MeV/degree (100 MeV/degree). In the case of neutral deposits, no charged particle with more than 250 MeV was allowed inside the inner cone. The energy of the isolated particle was then re-evaluated as the sum of the energies inside the inner cone. For well identified leptons or photons[2] the above requirements were weakened. In this case the angle of the external cone, α, was varied according to the energy of the lepton (photon) candidate, down to 2° for

[2]Well identified electrons or photons were those classified as tight by the REMCLU. Well identified muons were those classified as tight or standard by MUFLAG (*c.f.* chapter 3).

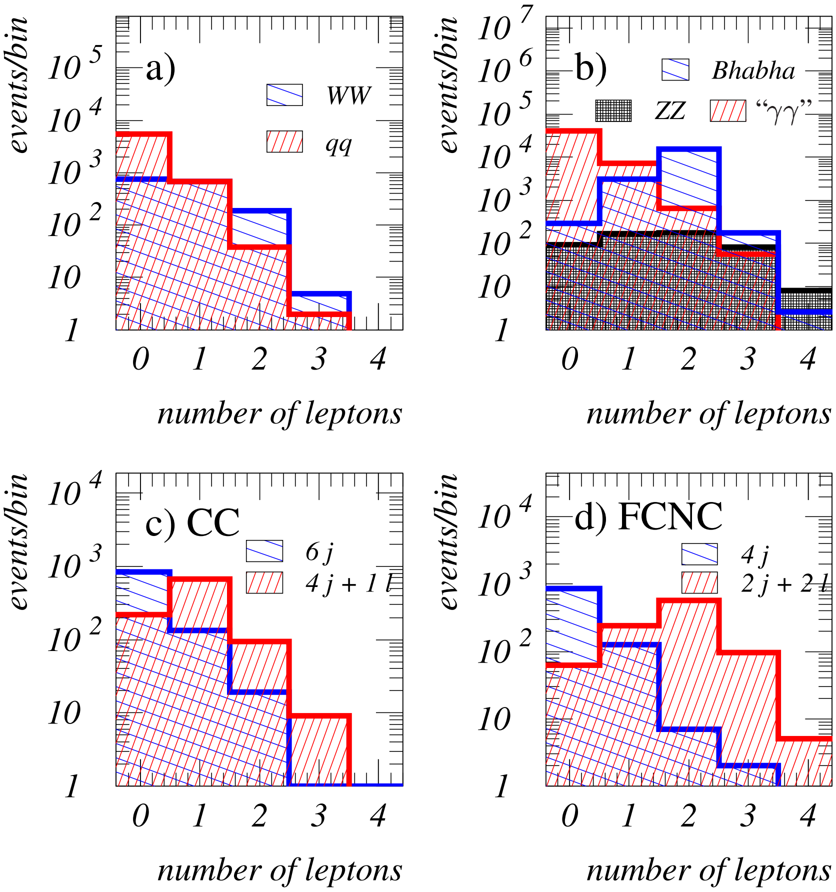

Figure 5.3: *Distribution of the number of isolated leptons present in the simulated events ($\sqrt{s} = 207$ GeV). The background contributions from different SM processes are shown: (a) WW and $q\bar{q}$, (b) Bhabha, ZZ and "$\gamma\gamma$" events . The signal distributions ($m_{b'} = 100$ GeV/c^2) are also shown: (c) CC and (d) FCNC b' decays (the FCNC six jet final state is very similar to the CC one).*

$p_l \geq 70$ GeV/c (3° for $E_\gamma \geq 90$ GeV). The allowed energy inside the cone was reduced by $\sin\alpha/\sin 25°$ ($\sin\alpha/\sin 15°$) and no further energy association was done.

The number of isolated leptons and photons in the simulated samples (both background and signal) are shown in figures 5.3 and 5.4, respectively.

5.1.2 Hadronic jets

All particles, except isolated leptons, were clustered into jets by using the Durham iterative jet algorithm [93]. In each iteration, the scaled transverse momentum,

$$y_{ij} = 2\frac{\min(E_i^2, E_j^2)}{E_{vis}^2}[1 - \cos(\alpha_{ij})], \tag{5.1}$$

is calculated for each pair of final state particles. E_i and E_j are the energies of the particles i and j, α_{ij} is the angle between them and E_{vis} is the visible energy of the event. The two particles with the smallest value of y_{ij} are combined, defining

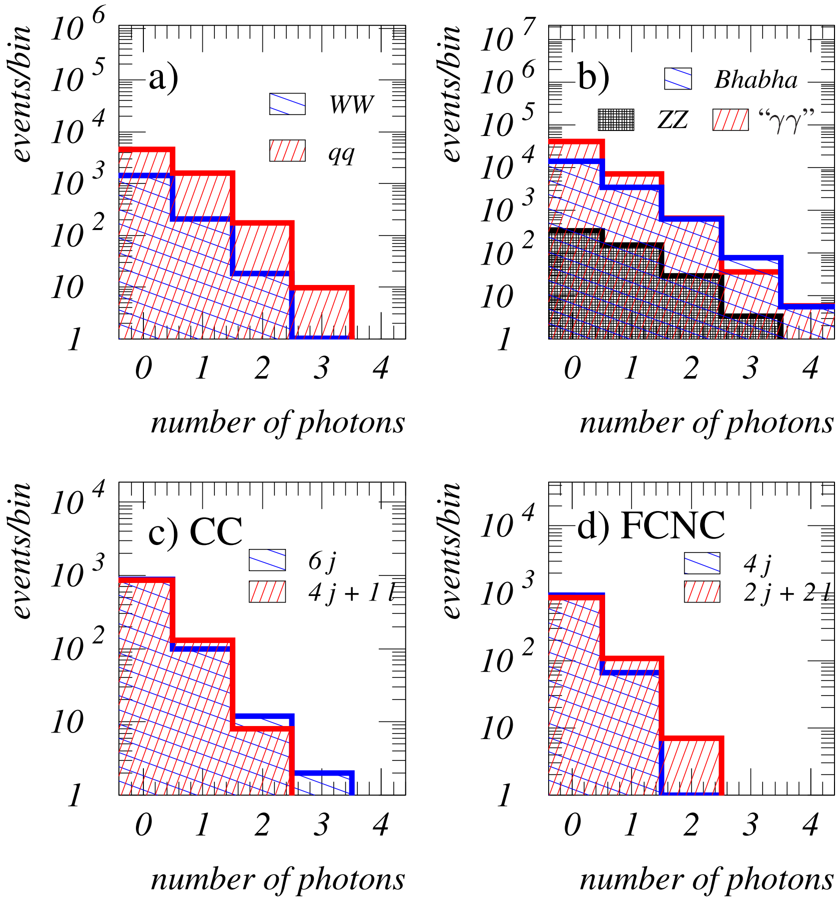

Figure 5.4: *Distribution of the number of isolated photons present in the simulated events ($\sqrt{s} = 207$ GeV). The background contributions from different SM processes are shown: (a) WW and $q\bar{q}$, (b) Bhabha, ZZ and "$\gamma\gamma$". The signal distributions ($m_{b'} = 100$ GeV/c^2) are also shown: (c) CC and (d) FCNC b' decays (the FCNC six jet topology is very similar to the CC one).*

a pseudoparticle with tetra-momentum $p_{ij}\,(E_{ij};\vec{p_{ij}})$, where $E_{ij} = E_i + E_j$ and $\vec{p_{ij}} = \vec{p_i} + \vec{p_j}$. Each pseudoparticle (or particle not grouped into a pseudoparticle) represents a jet.

The grouping of particles or pseudoparticles continues until the wanted number of jets is achieved. The minimum value of y_{ij} obtained when the event is clustered into n jets is the Durham jet resolution variable in the transition from n to $n-1$ jets ($y_{cut}(n \rightarrow n-1)$). This variable is related to the jet structure of the event.

All the events (both real and simulated) were clustered into two, four or six jets, according to the signal topology under study. In each analysis, the most suitable clustering for signal-like events identification (or, sometimes, for background rejection) was used. In each specific topology, the clustering into the signal number of the jets is assumed, unless explicitly stated.

When the jet comes from a b-quark, an useful tool is the DELPHI b-tagging algorithm [94], based on the identification of secondary vertex[3]. This algorithm is more efficient for energetic jets. Although two b jets are always present in the FCNC final states, they have a relatively low energy and the b-tagging technique was not used.

5.1.3 Missing energy and momentum

Due to the presence of neutrinos, some of the searched topologies ($bbll\nu\nu$, $bbjj\nu\nu$ and $ccqql\nu$) are characterized by the presence of missing energy ($E_{missing}$) and momentum ($p_{missing}$), defined as:

$$E_{missing} = \sqrt{s} - \sum_i E_i \ , \tag{5.2}$$

$$p_{missing} = ||\vec{p}_{missing}|| = || - \sum_i \vec{p_i}|| \ , \tag{5.3}$$

where i runs over all the measured charged and neutral particles. It is also common to define the missing mass as $\sqrt{E^2_{missing} - p^2_{missing}}$.

5.1.4 Common event preselection

Before a more restrictive analysis, an event preselection, common to all topologies, was done. Quality criteria were adopted to assure that only well reconstructed particles are considered. The charged multiplicity and visible momentum were used to reject background events with topologies incompatible with the studied signals. This preselection is described below.

[3] The b-quark has an average lifetime of 1.6 ps [23] and, consequently, it can originate a secondary vertex displaced from interaction point.

Quality criteria

Charged tracks were required to have a momentum greater than 0.2 GeV/c. The impact parameters in the transverse plane ($d_{R\phi}$) and in the beam direction (d_z) had to be below 4 cm (θ is the polar angle) and $4/\sin\theta$ cm, respectively. Only tracks passing this criteria were taken into account.

Further quality criteria were adopted for the events with leptons. Only leptons with a VD signal (*i.e.* with hits in, at least, two different layers of the VD) and with more than three hits in the TPC were considered. Additionally, leptons were required to have a momentum greater than 10 GeV/c and a polar angle above 25° and below 155°.

Charged multiplicity

As the considered topologies have, at least, two jets, the number of charged tracks present in the signal-like events is expected to be high. The distributions of the track multiplicities for the simulated events (background and signal) are shown in figure 5.5.

Events were required to have, at least, eight tracks. As signal events are expected to have a relatively high final state track multiplicity, this cut allowed to reduce the background contamination without loosing signal efficiency.

Visible momentum

The DELPHI detector covered about 90% of the solid angle, as previously discussed (chapter 3). In some cases (as for instance, events with particles along the beam pipe), the visible momentum can be very small. In the signal final states, most of the particles are expected to be in the barrel region of the detector. Therefore, the visible momentum, $p_{visible}$, defined as $\sum_i ||\vec{p}_i||$, where $\vec{p}_i$ is the momentum of each charged track, is expected to be high. The distributions of the visible momentum above 20° and below 160° in polar angle, $p_{visible}(barrel)$, of the background and signal simulated events are shown in figure 5.6.

As it can be seen from figure 5.6, the cut $p_{visible}(barrel)/\sqrt{s} > 0.2\,(1/c)$, largely reduces the "$\gamma\gamma$" background contribution, without practically affecting signal CC distributions. For the FCNC decays some less efficiency is expected.

5.2 Topology assignment

The number of isolated leptons (figure 5.3) and the missing energy variables were used to assign each data and simulated event to a specific topology within each decay

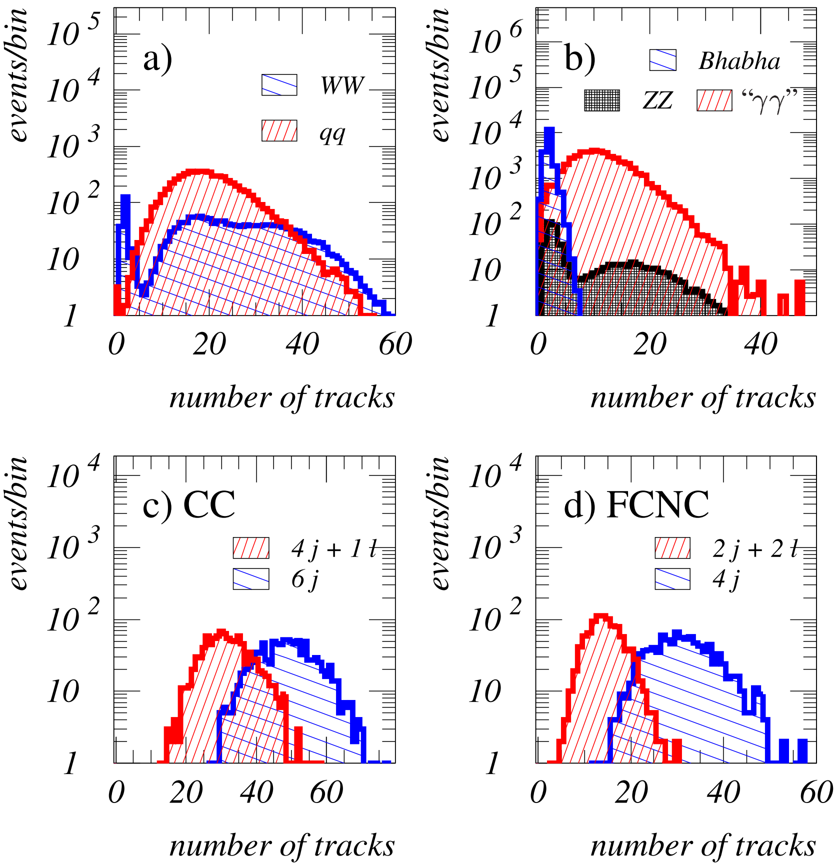

Figure 5.5: *Distribution of the charged track multiplicities of the simulated events ($\sqrt{s} = 207$ GeV). The background contributions from different SM processes are shown: (a) WW and $q\bar{q}$, (b) Bhabha, ZZ and "$\gamma\gamma$" events. The signal distributions ($m_{b'} = 100$ GeV$/c^2$) are also shown: (c) CC and (d) FCNC b' decays (the FCNC six jets topology is very similar to the CC one).*

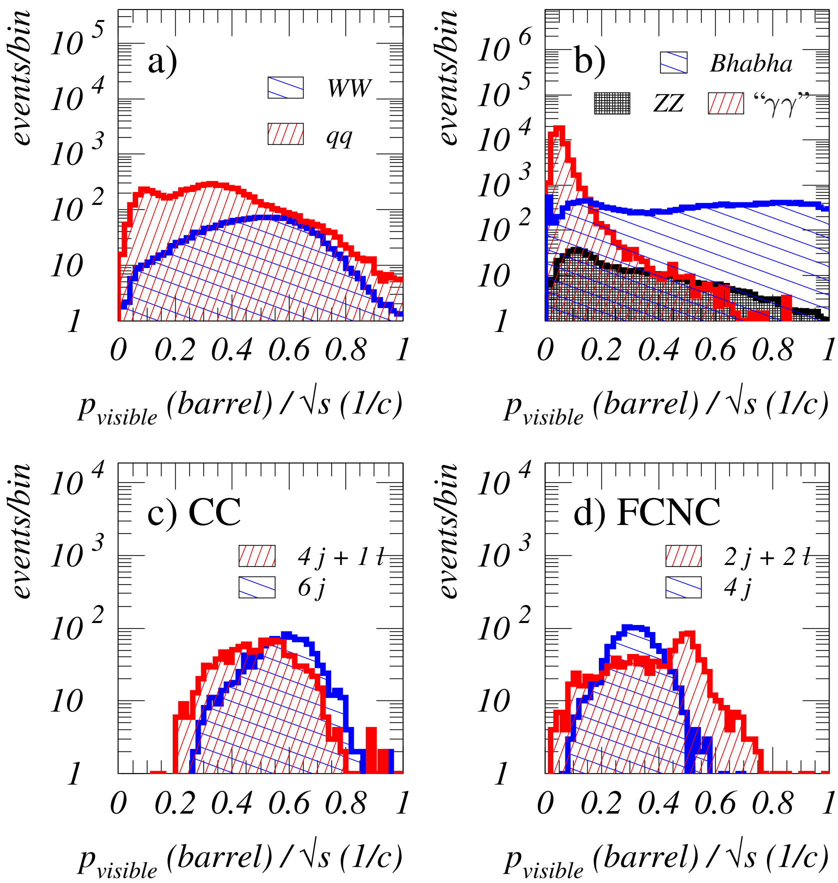

Figure 5.6: *Distributions of the visible momentum (above* 20° *and below* 160° *in polar angle) of the simulated events (*$\sqrt{s}$ = 207 *GeV). The background contributions from different SM processes are shown: (a)* WW *and* $q\bar{q}$*, (b) Bhabha,* ZZ *and "*$\gamma\gamma$*" events. The signal distributions (*$m_{b'}$ = 100 GeV/c^2*) are also shown for the: (c) CC and (d) FCNC* b' *decays (the FCNC six jet topology is very similar to the CC one).*

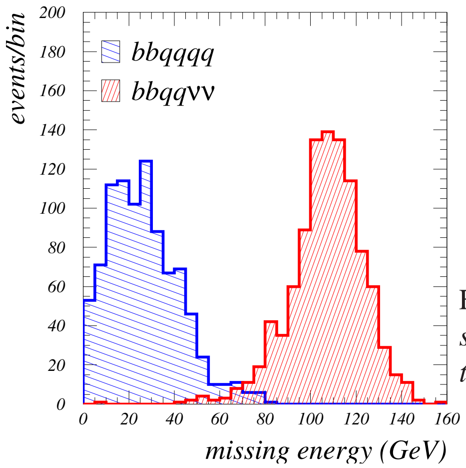

Figure 5.7: *Distribution of the missing energy of the signal events ($\sqrt{s}$ = 207 GeV, $m_{b'}$ = 100 GeV/c^2) for the FCNC $bbqq\nu\nu$ and $bbqqqq$ topologies.*

channel[4] (FCNC and CC).

In the FCNC channel, events with at least one isolated lepton were assigned to the $bbll\nu\nu$ topology. Overlap between the $bbqq\nu\nu$ and $bbqqqq$ topologies was avoided using the $E_{missing}$ variable (figure 5.7). Events with no isolated leptons having $E_{missing} <$ 50 GeV were classified as $bbqqqq$ candidates, while those with $E_{missing} >$ 50 GeV were considered $bbqq\nu\nu$ candidates.

In the CC channel, events with one lepton were assigned to the $ccqql\nu$ topology, while those without leptons and $E_{missing} <$ 50 GeV were considered as $ccqqqq$ candidates.

In all topologies, the signal is mostly characterized by the absence of isolated photons (figure 5.4). Consequently, only events without isolated photons were selected.

Whenever there were isolated leptons in the final state (FCNC $bbll\nu\nu$ and CC $ccqql\nu$), events were divided into different samples, according to the lepton flavour identification. Electron candidates classified as tight by the REMCLU and muons identified as standard or tight by the MUFLAG (*c.f.* chapter 3) were considered well identified. All the other isolated leptons were assumed to have non-identified flavour. The lepton flavour event samples are enumerated below.

1. *e sample:* well identified electrons.

2. *μ sample:* well identified muons.

3. *no-id sample:* leptons with non-identified flavour or two leptons identified with different flavours.

The criteria used to perform the topology assignment are summarized in table 5.2.

[4] As the aim of present analyses is to place independent limits in $BR_{b'\to bZ}$ and $BR_{b'\to cW}$, the same data candidate may be assigned to one topology in the FCNC channel and to another in the CC channel. It is only between the different final state topologies of the same decay mode (FCNC or CC) that overlap has to be avoided.

topology	assignment criteria
$bbll\nu\nu$	at least 1 isolated lepton no isolated photons
$bbqq\nu\nu$	no isolated leptons $E_{missing} > 50$ GeV no isolated photons
$bbqqqq$	no isolated leptons $E_{missing} < 50$ GeV no isolated photons
$ccqql\nu$	1 isolated lepton no isolated photons
$ccqqqq$	no isolated leptons $E_{missing} < 50$ GeV no isolated photons

Table 5.2: *Summary of the topology assignment criteria.*

5.3 Specific analyses

The specific criteria applied to each event topology are discussed in this section. For the $bbll\nu\nu$ topology a sequential analysis was used. In all other topologies a discriminant analysis was additionally applied in order to improve the signal to noise ratio. This method is based on the construction of a discriminant variable and it is discussed in appendix A.

5.3.1 FCNC $b' \to bZ$ decay

The searched topologies corresponding to the FCNC $b' \to bZ$ decay are $bbll\nu\nu$, $bbqq\nu\nu$ and $bbqqqq$, depending on the Z decay modes. As $m_Z \sim 90$ GeV/c^2, in the considered b' mass range($m_{b'} = 96 \to 103$ GeV/c^2), the Z and b are produced almost at rest.

In the FCNC topologies, the Z mass reconstruction can be done by evaluating the invariant mass of two of the jets and of the two leptons (for the $bbll\nu\nu$ topology) or the missing mass (for the $bbll\nu\nu$ and $bbqq\nu\nu$ topologies). The reconstruction with better resolution is done with the leptons, due to the small errors associated to the momentum measurements. This leads to a very clear signature for the $bbll\nu\nu$ topology and it is the reason for the choice of a sequential analysis[5]. For the other topologies, a sequential analysis followed by a probabilistic analysis was adopted. In a probabilistic analysis a signal likelihood ($\mathcal{L}_S$) and a background likelihood ($\mathcal{L}_B$) are calculated for each event by using Probability Density Functions (PDFs) based on relevant physical variables. The discriminant variable is defined as $\ln(\mathcal{L}_S/\mathcal{L}_B)$ (*c.f.* appendix A).

[5] In this type of analysis, a sequential set of cuts on relevant physical variables is used to select events on a particular region of the phase space.

$bbll\nu\nu$ topology

The signature of the $bbll\nu\nu$ topology is the presence of two low energy jets, two energetic leptons and a missing mass around m_Z. The distributions of relevant variables after the preselection level (section 5.1.4) are shown in figure 5.8. A fair agrement between data and SM expectation is observed in the three leptonic samples.

The event selection was done in two levels. In the first one, events were required to have at least two leptons, the effective centre-of-mass energy [95], $\sqrt{s'}$, had to be below $0.95\sqrt{s}$ and $-\log_{10}[y_{cut}(2 \to 1)] < 2.7$ (*c.f.* figures 5.9-5.11).

The number of data events and background expectation after this first selection level is shown in table 5.3. The background composition is roughly 16% of $q\bar{q}$, 16% of WW and 68% of ZZ for the e sample; 10% of WW and 90% of ZZ for the μ sample and 8% of $q\bar{q}$, 12% of ZZ and 80% of ZZ for the *no-id* sample.

$\sqrt{s}$ (GeV)	data (SM expectation)		
	e sample	μ sample	*no-id* sample
196	2 (2.6±0.3)	1 (2.9±0.3)	47 (35.9±1.4)
200	3 (2.5±0.4)	4 (3.4±0.4)	30 (37.4±1.4)
202	2 (1.3±0.2)	1 (1.7±0.2)	20 (18.7±0.7)
205	5 (2.5±0.4)	3 (3.0±0.4)	35 (36.2±1.4)
207	3 (2.3±0.4)	3 (3.1±0.4)	45 (35.1±1.3)
206*	1 (1.9±0.3)	2 (2.6±0.2)	31 (27.6±1.0)
total	16 (13.2±0.8)	14 (16.7±0.8)	208 (191.0±3.0)

Table 5.3: *$bbll\nu\nu$ topology: number of events selected in data and SM expectation after the first selection level for each sample and centre-of-mass energy.*

As in the adopted working region $m_{b'} \sim m_Z$, the two jets present in the signal-like events are expected to have low energy. The second selection level (named final selection) was made by requiring the momenta of the first and second jets to be below 30 GeV/c and 12.5 GeV/c, respectively (figures 5.12a-b, 5.13a-b and 5.14a-b). Furthermore, in this selection level, dedicated cuts for each of the samples were also applied:

- e sample: the $E_{missing}/\sqrt{s}$ (figure 5.12c) was required to be above 0.4. This cut was done in order to select only the events with missing energy compatible with a Z decaying invisibly.
- μ sample: the angle between the two muons (figure 5.13c) had to be greater than 125°. This requirement was motivated by the small Z boost, which lead to an almost back-to-back decay $Z \to \mu\mu$.
- *no-id* sample: events were required to have $E_{missing}/\sqrt{s} > 0.4$ (figure 5.14c), the angle between the two leptons (figure 5.14d) above 140° and $p_{missing}/E_{missing} < 0.4/c$ (figure 5.14e).

After the final selection, 1 (1.5±0.7) data (background) event was selected (*c.f.* table 5.4). At this level, the background was almost entirely dominated by ZZ events

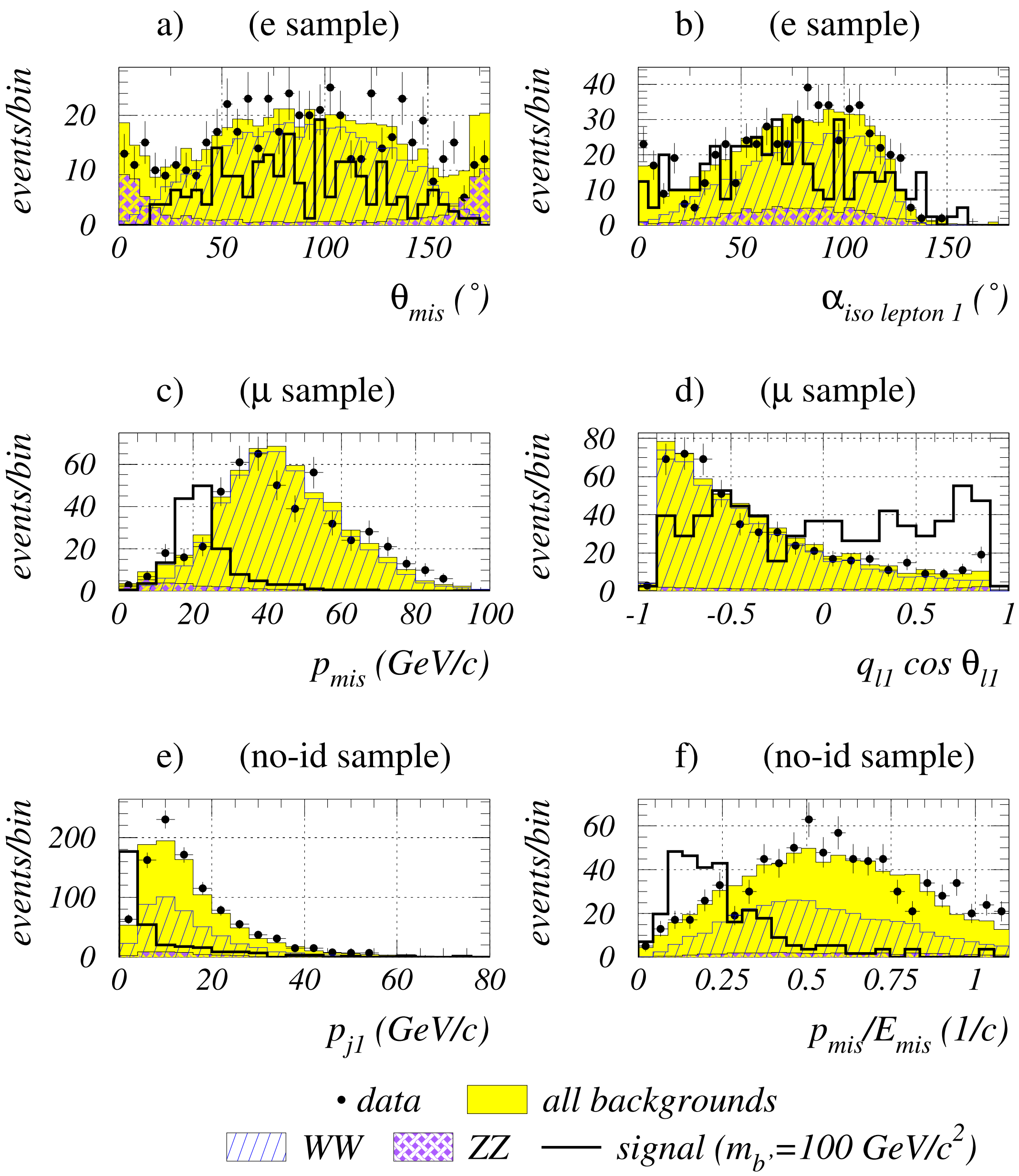

Figure 5.8: *$bbll\nu\nu$ topology: Data and SM expectation (total, WW and ZZ) distributions after the preselection level for $\sqrt{s}$ = 202 − 207 GeV. (a) The polar angle of the missing momentum (e sample), (b) the isolation angle of the most energetic lepton (e sample), (c) the missing momentum (μ sample), (d) $q_{l1} \times \cos\theta_{l1}$, where q_{l1} and θ_{l1} are the charge (normalized to the positron charge) and the polar angle of the most energetic lepton (μ sample), (e) the momentum of the most energetic jet (*no-id *sample) and (f) the ratio between the missing momentum and energy (*no-id *sample) are shown. The signal distributions with arbitrary normalization for $m_{b'}$ = 100 GeV/ c^2 and $\sqrt{s}$ = 205 GeV are also shown.*

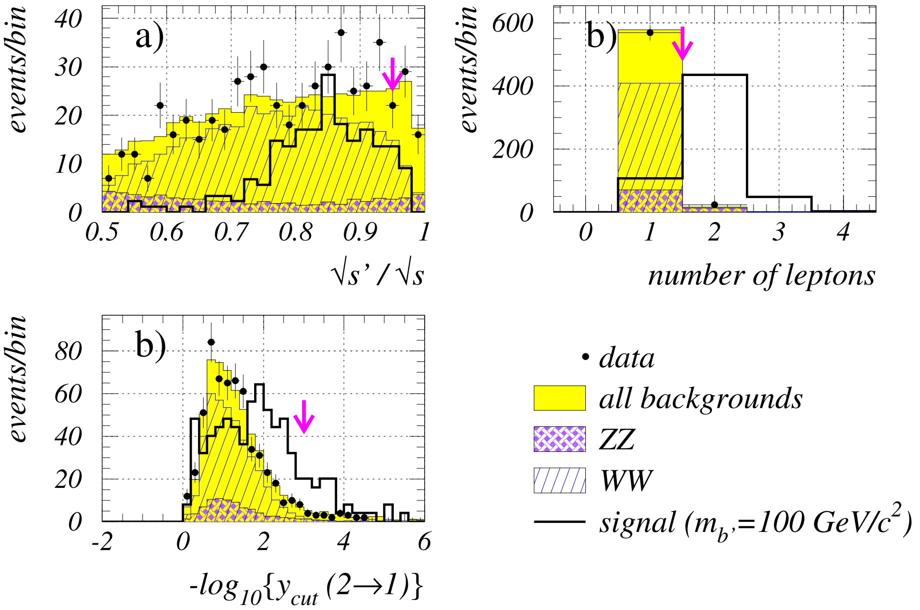

Figure 5.9: *bbllνν topology (e sample): data and SM expectation distributions before the first level of selection for* $\sqrt{s} = 202 - 207$ *GeV. (a)* $\sqrt{s'}/\sqrt{s}$*, (b) number of leptons and (c)* $-\log_{10}[y_{cut}(2 \to 1)]$ *are shown. The main background contributions (ZZ and WW) and the cuts applied at the first selection level (arrows) are represented. The signal distributions with arbitrary normalization for* $m_{b'} = 100$ *GeV/* c^2 *and* $\sqrt{s} = 205$ *GeV are also shown.*

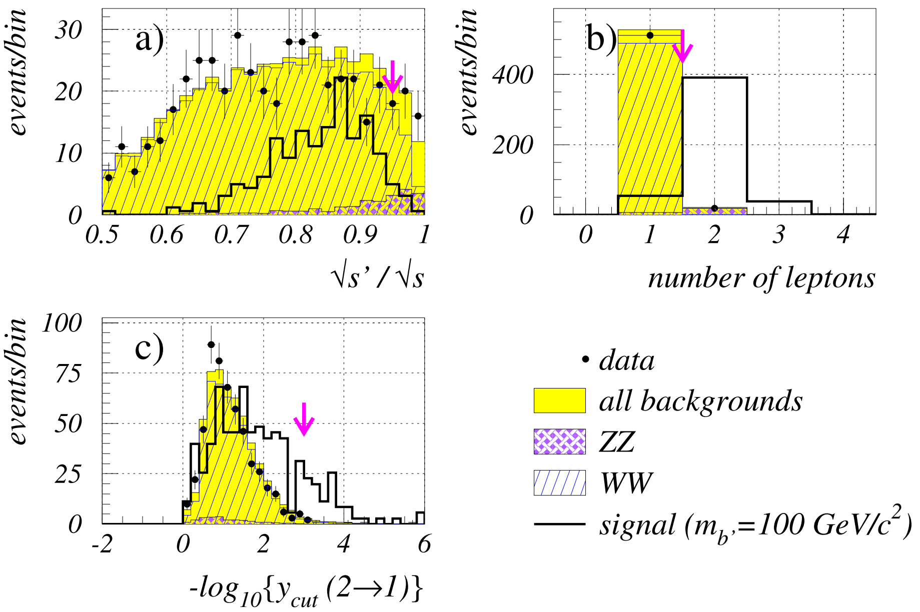

Figure 5.10: *bbllνν topology (μ sample): data and SM expectation distributions before the first level of selection for* $\sqrt{s} = 202 - 207$ *GeV. (a)* $\sqrt{s'}/\sqrt{s}$*, (b) number of leptons and (c)* $-\log_{10}[y_{cut}(2 \to 1)]$ *are shown. The main background contributions (ZZ and WW) and the cuts applied at the first selection level (arrows) are represented. The signal distributions with arbitrary normalization for* $m_{b'} = 100$ *GeV/* c^2 *and* $\sqrt{s} = 205$ *GeV are also shown.*

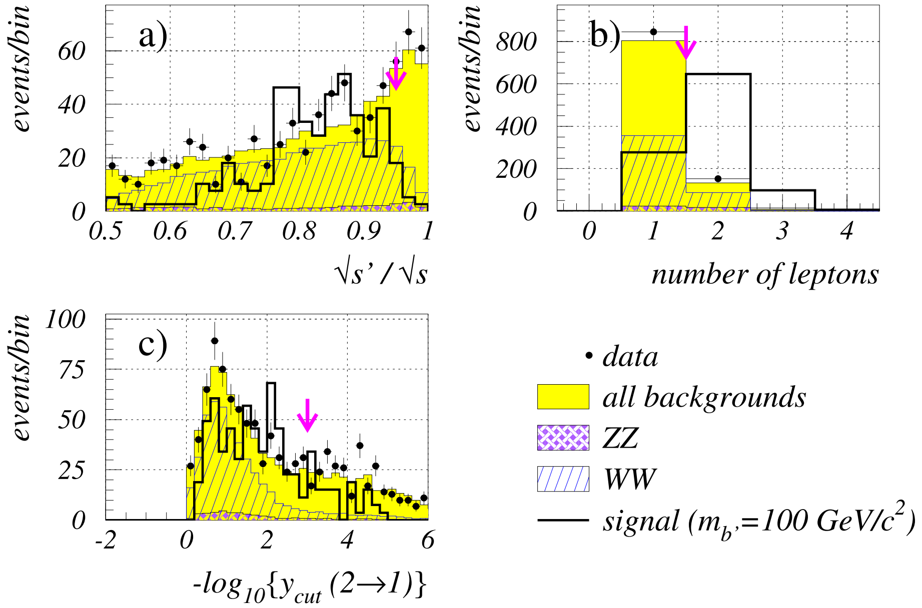

Figure 5.11: *bbllνν topology* (no-id *sample): data and SM expectation distributions before the first level of selection for* $\sqrt{s}$ = 202 − 207 *GeV. (a)* $\sqrt{s'}/\sqrt{s}$*, (b) number of leptons and (c)* $-\log_{10}[y_{cut}(2 \to 1)]$ *are shown. The main background contributions (ZZ and WW) and the cuts applied at the first selection level (arrows) are represented. The signal distributions with arbitrary normalization for* $m_{b'}$ = 100 *GeV/* c^2 *and* $\sqrt{s}$ = 205 *GeV are also shown.*

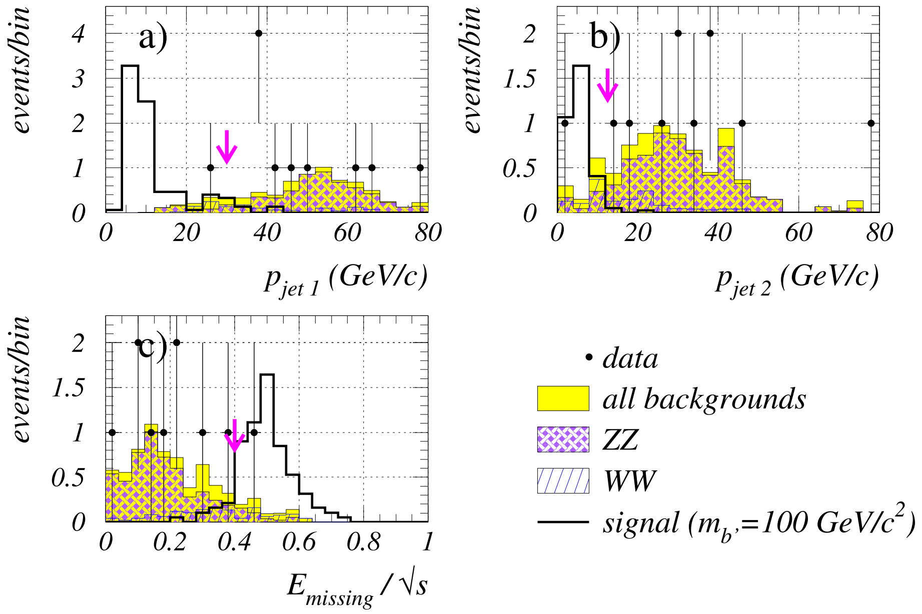

Figure 5.12: *bbllνν topology (e sample): comparison, before the final selection cuts, of the data events and background expectation (the two most relevant background processes, ZZ and WW, are also shown). Distribution of the momentum of (a) the first and (b) second jets and of (c) the ratio* $E_{missing}/\sqrt{s}$*. In these distributions the* $\sqrt{s}$ = 202 − 207 *GeV samples were added. Signal distributions for* $m_{b'}$ = 100 *GeV/* c^2 *and* $\sqrt{s}$ = 205 *GeV are also shown with arbitrary normalization.*

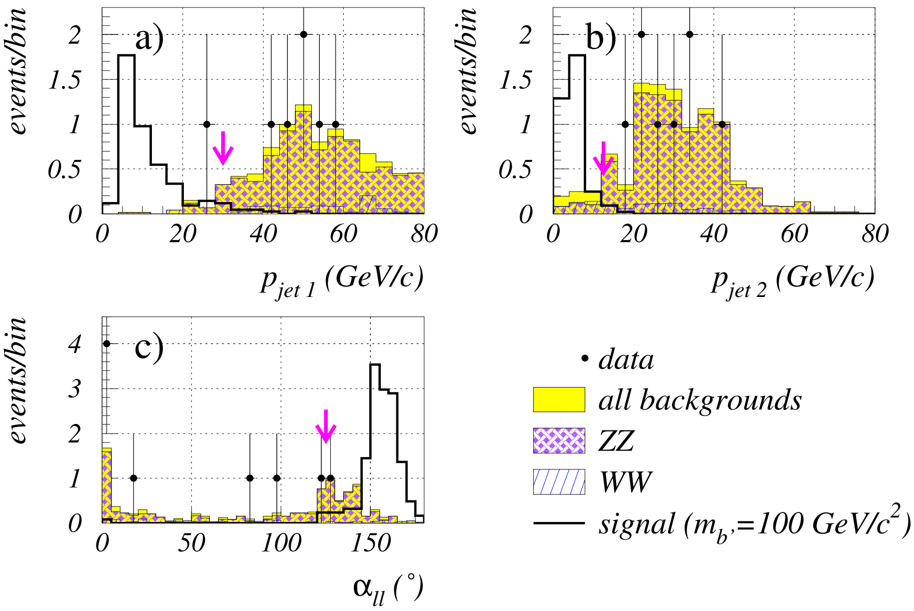

Figure 5.13: *$bbll\nu\nu$ topology (μ sample): comparison, before the final selection cuts, of the data events and background expectation (the two most relevant background processes, ZZ and WW, are also shown). Distribution of the momentum of (a) the first and (b) second jets and of (c) the angle between the two leptons (muons). In these distributions the $\sqrt{s} = 202 - 207$ GeV samples were added. Signal distributions for $m_{b'} = 100$ GeV/ c^2 $\sqrt{s} = 205$ GeV are also shown with arbitrary normalization.*

(other backgrounds represent less than 1% of the total).

$\sqrt{s}$ (GeV)	data (SM expectation)		
	e	μ	*no-id*
196	0 (0.0±0.3)	0 (0.0±0.2)	0 (0.5±0.3)
200	0 (0.0±0.3)	0 (0.1±0.3)	1 (0.4±0.3)
202	0 (0.0±0.1)	0 (0.0±0.1)	0 (0.2±0.1)
205	0 (0.7±0.3)	0 (0.1±0.3)	0 (0.1±0.3)
207	0 (0.0±0.3)	0 (0.1±0.3)	0 (0.1±0.3)
206*	0 (0.0±0.2)	0 (0.0±0.2)	0 (0.2±0.2)
total	0 (0.7±0.6)	0 (0.2±0.6)	1 (1.5±0.7)

Table 5.4: *$bbll\nu\nu$ topology: number of events selected in data and SM expectation after the final selection level for each sample and centre-of-mass energy.*

The signal efficiencies, ε, for $m_{b'} = 100$ GeV/c^2 and for each selection level are shown at table 5.5. The efficiency values for the other b' masses are within 1.5%, 1.7% and 1.2% for the electron, muon and *no-id* samples, respectively. The overall efficiency is $\varepsilon \times BR_{ZZ \to ll\nu\nu}$, where $BR_{ZZ \to ll\nu\nu}$ is given in table 5.1.

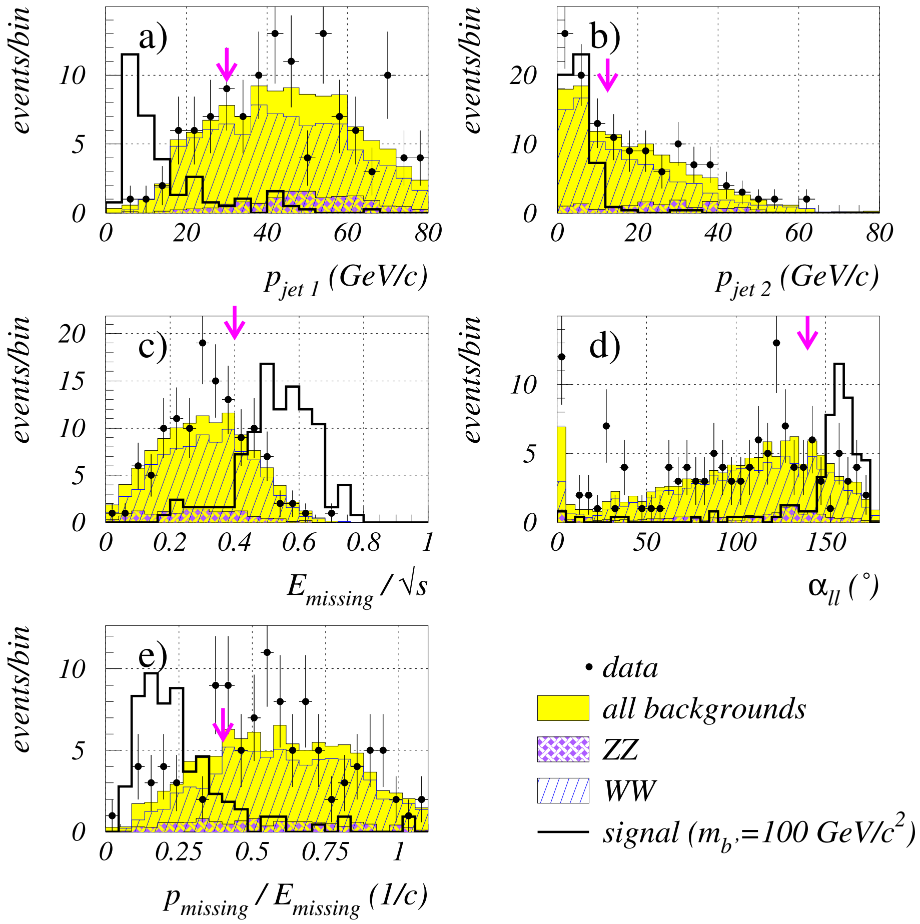

Figure 5.14: *$bbll\nu\nu$ topology (*no-id *sample): comparison, before the final selection cuts, of the data events and background expectation (the two most relevant background processes, ZZ and WW, are also shown). Distribution of the momentum of (a) the first and (b) second jets, (c) the ratio $E_{missing}/\sqrt{s}$, (d) the angle between the two leptons and (e) the ratio $p_{missing}/E_{missing}$. In these distributions the $\sqrt{s} = 202 - 207$ GeV samples were added. Signal distributions for $m_{b'} = 100$ GeV/ c^2 $\sqrt{s} = 205$ GeV are also shown with arbitrary normalization.*

$\sqrt{s}$ (GeV)	ε ($m_{b'}$ = 100 GeV/c^2) (%)					
	first selection level			final selection		
	e	μ	*no-id*	e	μ	*no-id*
196	11.3±1.1	17.9±1.3	12.1±1.1	9.1±1.0	16.0±1.3	8.8±0.9
200	11.3±1.1	16.6±1.3	12.1±1.1	9.1±1.0	16.2±1.3	8.8±0.9
202	11.3±1.1	16.6±1.3	12.1±1.1	9.1±1.0	16.2±1.3	8.8±0.9
205	11.7±1.1	17.8±1.3	12.3±1.1	10.2±1.0	16.2±1.3	7.2±0.8
207	12.5±1.1	18.5±1.4	11.5±1.1	10.4±1.0	16.6±1.3	7.7±0.9
206*	11.4±1.1	17.9±1.3	10.0±1.0	9.1±1.0	16.0±1.3	5.9±0.8

Table 5.5: *$bbll\nu\nu$ topology: signal efficiencies for $m_{b'} = 100$ GeV/ c^2 and for each centre-of-mass energy. The overall efficiency is $\varepsilon \times BR_{ZZ\to ll\nu\nu}$, where $BR_{ZZ\to ll\nu\nu}$ is given in table 5.1.*

$bbq\nu\nu$ topology

The $bbqq\nu\nu$ topology is characterized by the presence of four jets and a missing mass around m_Z. No isolated leptons or photons in the final state were allowed and the missing energy was required to be above 50 GeV.

A first level of selection was done using a sequential set of cuts on relevant variables. To avoid non-isolated leptons clustered together with the jets, events were required to have the most energetic track of the first jet with momentum below $0.1\sqrt{s}/c$ (figure 5.15a). Events with $y_{cut}(2 \to 1) < 0.2$ (figure 5.15b), corresponding to a mono-jet structure, were rejected. At least 20 charged tracks (figure 5.15c) were required in the events.

In order to partially reject the $q\bar{q}$ and semi-leptonic WW[6] backgrounds, which are characterized by the presence of two jets, a four jet structure was selected by requiring $-\log_{10}[y_{cut}(4 \to 3)] < 2.8$ (figure 5.15d). An important fraction of the radiative $q\bar{q}$ was rejected by selecting the events with $\sqrt{s'}$, above $0.5\sqrt{s}$ (figure 5.15e). The number of selected data events and SM expectation at the first level of selection can be seen in table 5.6.

$\sqrt{s}$ (GeV)	data (SM expectation)	
	first level of selection	$\chi^2/n.d.f.$ cut
196	203 (189.6±5.0)	123 (106.3±4.0)
200	210 (202.5±5.2)	111 (104.8±4.0)
202	94 (95.9±2.5)	50 (49.8±1.9)
205	176(190.0±4.8)	88 (94.2±3.7)
207	203 (190.4±4.7)	99 (91.2±3.6)
206*	142 (144.4±3.6)	62 (65.7±2.6)
total	1028 (1016.8 ± 10.8)	533 (511.7± 8.3)

Table 5.6: *$bbqq\nu\nu$ topology: number of events selected in data and SM expectation for each centre-of-mass energy after the first selection level and after the $\chi^2/n.d.f.$ cut.*

[6] *i.e.* when one of W decays into hadrons and the other into leptons.

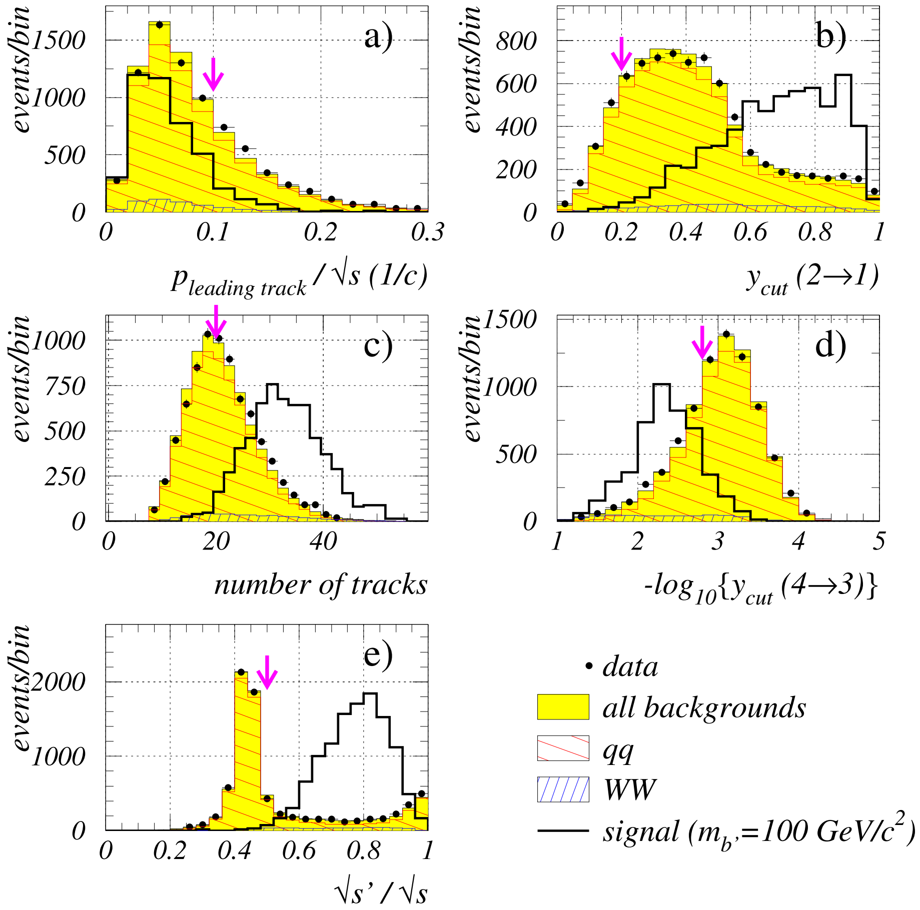

Figure 5.15: *bbqqνν topology: comparison of data and background expectation before the first level of selection ($\sqrt{s} = 202 - 207$ GeV). (a) The ratio between the momentum of the most energetic particle of the first jet and $\sqrt{s}$, (b) $y_{cut}(2 \to 1)$, (c) the multiplicity of charged tracks, (d) $-\log_{10}[y_{cut}(4 \to 3)]$ and (e) $\sqrt{s'}/\sqrt{s}$ are shown. The main background contributions (WW and $q\bar{q}$) are also shown. The signal normalization is arbitrary. The arrows represent the cuts applied at the first level of selection. The signal distributions for $m_{b'} = 100$ GeV/ c^2 and $\sqrt{s} = 205$ GeV are also shown with arbitrary normalization.*

$\sqrt{s}$ (GeV)	ε ($m_{b'}$ = 100 GeV/c^2) (%)	
	first level of selection	$\chi^2/n.d.f.$ cut
196	58.6±2.4	56.1±2.4
200	56.0±2.4	47.9±2.2
202	58.6±2.4	56.1±2.5
205	59.6±2.4	57.6±2.4
207	57.6±2.4	53.1±2.4
206*	56.1±2.4	53.5± 2.4

Table 5.7: *bbqq$\nu\nu$ topology: signal efficiencies for $m_{b'} = 100$ GeV/ c^2 and for each centre-of-mass energy. The overall efficiency is $\varepsilon \times BR_{ZZ \to qq\nu\nu}$.*

At this level, the signal efficiencies, ε, for $m_{b'} = 100$ GeV/c^2 and for each centre-of-mass energy are shown in table 5.7. The efficiency values for the other b' masses are within 3.4%. The overall efficiency is $\varepsilon \times BR_{ZZ \to qq\nu\nu}$ (*c.f.* table 5.1).

The direction of most particles is measured at DELPHI with a very good precision. However, the uncertainty on the momentum of the neutrinos (which are not reconstructed) and of the jets is higher. As the *bbqq$\nu\nu$* topology is characterized by the presence of four jets and two neutrinos, background events without neutrinos (*e.g.* $qq(\gamma)$ and hadronic WW) should be clearly distinguished from the signal events, which are expected to have a high missing mass. To do this, a kinematic fit imposing energy and momentum conservation was performed, according to the method described in [96]. Assuming that all particles are detected, the total energy and momentum should be conserved. Therefore, the tetra-momenta of the particles measured with larger errors may be constrained by the well measured quantities (other tetra-momenta and $\sqrt{s}$). Obviously, the measured quantities must be varied only within the experimental error[7]. The quality of the fit for each event is evaluated by the associated $\chi^2 = \sum_i \frac{(X_i^{fit} - X_i^{measured})^2}{\sigma^2_{X_i}}$, where σ_{X_i} is the experimental error associated to the observable X_i and X_i^{fit} ($X^{measured}$) is its value after (before) the fit.

The $\chi^2/n.d.f.$ of this fit for the data, SM expectation and signal events is shown is figure 5.16. The signal events have a high $\chi^2/n.d.f.$, while the background events with a small missing energy fit better the energy-momentum conservation hypothesis. Only events with $\chi^2/n.d.f. > 6$ were accepted. The number of data candidates and MC expectation after the $\chi^2/n.d.f.$ cut can be seen in table 5.6. The signal efficiencies (for $m_{b'} = 100$ GeV/c^2) are shown in table 5.7. The efficiency values for the other b' masses are within 3.2%.

After this selection, the discriminant variables were built based on the PDFs of several variables (appendix A). These variables were chosen in order to distinguish, as clearly as possible, the SM expectation from the signal. The physical variables used to construct the PDFs were:

1. the missing mass (figure 5.17a), which is roughly m_Z for the signal. This variable is sharper for the signal than for the background;

[7] The experimental resolutions were discussed in chapter 3.

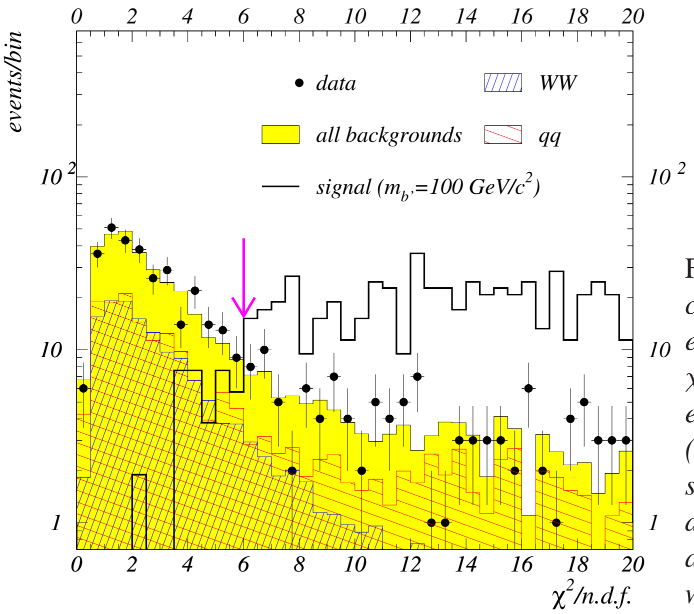

Figure 5.16: bbqqνν topology: comparison of data and SM expectation distributions of the $\chi^2/n.d.f.$ of the fit imposing energy-momentum conservation ($\sqrt{s}$ = 202 − 207 GeV). The arrow shows the applied cut. The signal distributions for $m_{b'}$ = 100 GeV/ c^2 and $\sqrt{s}$ = 205 GeV are also shown with arbitrary normalization.

2. the scaled acoplanarity, $\boldsymbol{Acop_{j_1j_2} \times \min(\sin\theta_{j_1}, \sin\theta_{j_2})}$ (figure 5.17b), where $Acop_{j_1j_2}$ is defined as $|180 - |\phi_{j_1} - \phi_{j_2}||$ and ϕ_{j_1,j_2} (θ_{j_1,j_2}) are the azimuthal (polar) angles of the jets. $j_{1,2}$ are the first and second jets of the event, with the events clustered into two jets (as the four jets topology characterizes the signal, the two jets configuration was used for the background rejection). At this level, the most important contribution for the background is the $q\bar{q}$ process[8].

3. the acoplanarity, $\boldsymbol{180° - \alpha_{j1j2}}$ (figure 5.17c), where α_{j1j2} is the angle between the two most energetic jets.

4. the first and third Fox-Wolfram momenta [97, 98] sum, $\boldsymbol{h_1 + h_3}$ (figure 5.17d). The Fox-Wolfram momenta are related to the spatial configuration of the event and are defined as $h_l = \sum_{i,j} \frac{|p_i||p_j|}{E^2_{visible}} P_l[\cos\alpha_{i,j}]$, with P_l being the Legendre polynomials [99], i, j any pair of particles and $\alpha_{i,j}$ the angle between them;

5. the polar angle of the missing momentum, $\theta_{missing}$ (figure 5.17e). The radiative $q\bar{q}$ is characterized by a forward photon, which is lost along the beam pipe. Consequently, for this background, differently from the signal, the polar of the missing momentum is expected to be very low. Therefore, the variable $\theta_{missing}$ is significantly different for the signal and background events.

The discriminant variables, $\ln(\mathcal{L}_S/\mathcal{L}_B)$, for data, SM expectation and signal are shown in figure 5.18.

bbqqqq topology

The events compatible with the *bbqqqq* topology have a high charged tracks multiplicity and a low missing energy and momentum. The event selection was made by

[8]The background composition at this selection level is ∼ 75% of $q\bar{q}$, ∼ 17% of WW, ∼ 5% of "$\gamma\gamma$" and ∼ 2% of ZZ.

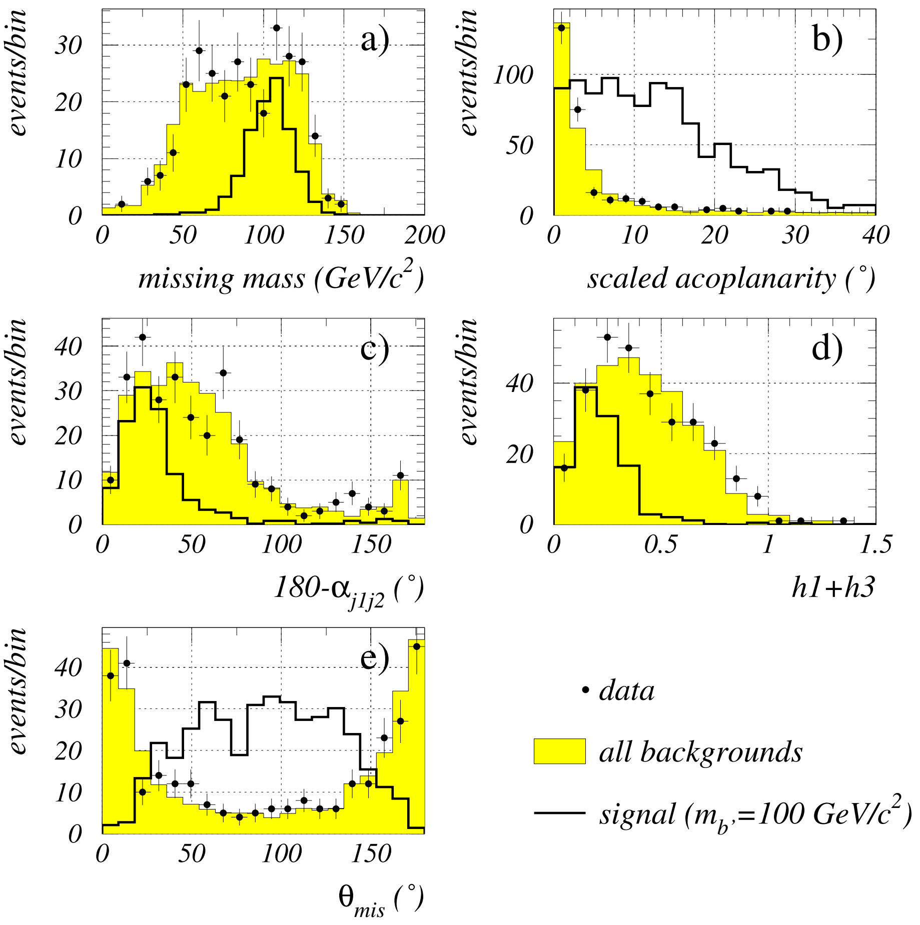

Figure 5.17: *bbqqνν topology: distribution of the variables based on which the PDFs were built. The data and SM expectation distributions for* $\sqrt{s} = 202 - 207$ *GeV are shown: (a) missing mass, (b)* $Acop_{j_1 j_2} \times \min(\sin\theta_{j_1}, \sin\theta_{j_2})$*, where* $j_{1,2}$ *are the first and second jets of the event, with the events clustered into two jets, (c) acolinearity, defined as* $180 - \alpha_{j_1 j_2}$*, (d) sum of the first and third Fox-Wolfram momenta and (e) the polar angle of the missing momentum. The signal distributions for* $m_{b'} = 100$ *GeV/* c^2 *and* $\sqrt{s} = 205$ *GeV are also shown.*

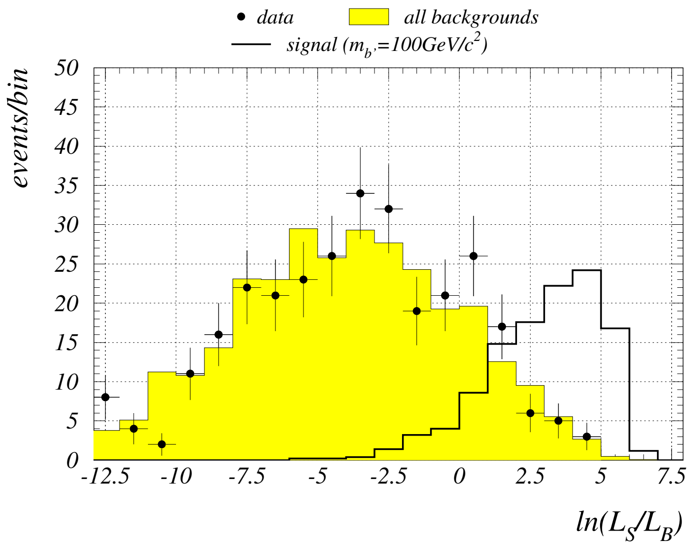

Figure 5.18: *bbqqνν topology: the discriminant variables,* $\ln(\mathcal{L}_S/\mathcal{L}_B)$*, for data and SM expectation* ($\sqrt{s} = 202 - 207$ *GeV) are shown. The signal distribution for* $m_{b'} = 100$ *GeV*/c^2 *and* $\sqrt{s} = 205$ *GeV is also shown.*

requiring at least 30 charged tracks and $p_{visible}(barrel) > 0.3\sqrt{s}$. Monojet-like events with $y_{cut}(2 \to 1) < 0.2$ were rejected (figure 5.19a). Furthermore, the effective centre-of-mass energy had to be above $0.6\sqrt{s}$ and a six-jet like structure was selected by requiring $-\log_{10}[y_{cut}(6 \to 5)] < 3.6$ (figures 5.19b and c). The number of selected data events and SM expectation are shown in table 5.8. The signal efficiencies for a b' mass of 100 GeV/c^2 are also shown. The efficiency values for the other b' masses under study are within 4.9%. The background composition is about 35% of $q\bar{q}$ and about 65% of WW.

$\sqrt{s}$ (GeV)	data (SM expectation)	$\varepsilon(m_{b'} = 100$ GeV/c^2) (%)
196	349 (326.7±5.3)	63.3±2.6
200	347 (342.1±5.5)	64.2±2.5
202	165 (162.1±2.6)	63.3±2.5
205	322 (319.0±5.2)	66.0±2.7
207	287 (307.6±5.0)	61.7±2.5
206*	192 (215.8±3.6)	60.1±2.5
total	1662 (1673.9±11.4)	—

Table 5.8: *bbqqqq topology: number of selected data events and SM expectation for each centre-of-mass energy after the first selection level. The signal efficiency,* ε*, for* $m_{b'} = 100$ *GeV/* c^2 *is also shown. The efficiency values for the other studied* b' *masses are within 4.9% and the overall efficiency is* $\varepsilon \times BR_{ZZ\to qqqq}$.

Following this first level of selection, a probabilistic analysis was used to improve the discrimination between six jet events (signal-like) and four jet events (background-like). The PDFs were built based on the following variables[9]:

[9]As defined in section 5.1.2, the events assigned to the *bbqqqq* topology were clustered into six jets, unless explicitly stated.

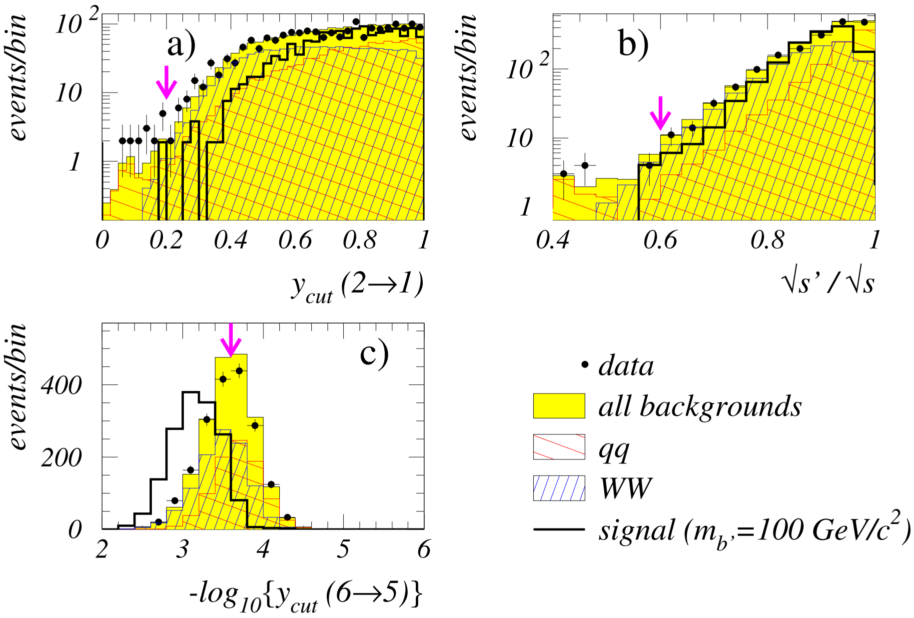

Figure 5.19: *bbqqqqq topology: comparison of data and background expectation at $\sqrt{s} = 202 - 207$ GeV. The distributions of (a) $y_{cut}(2 \to 1)$, (b) $\sqrt{s'}/\sqrt{s}$ and (c) $-\log_{10}[y_{cut}(6 \to 5)]$ are shown. The signal distributions for $m_{b'} = 100$ GeV/ c^2 and $\sqrt{s} = 205$ GeV are also shown with arbitrary normalization. The arrows show the cuts applied at the first level of selection.*

1. $\boldsymbol{-\log_{10}[y_{cut}(4 \to 3)]}$ (figure 5.20a);

2. $\boldsymbol{-\log_{10}[y_{cut}(5 \to 4)]}$ (figure 5.20b);

3. $\boldsymbol{180^\circ - \alpha_{j1j2(4jets)}}$, where $\alpha_{j1j2(4jets)}$ is the angle (in degrees) between the two most energetic jets, with the events clustered into four jets for background rejection (figure 5.20c);

4. the sum of the first and third Fox-Wolfram momenta, $\boldsymbol{h1 + h3}$ (figure 5.20d);

5. the momentum of the most energetic jet, $\boldsymbol{p_{j1}}$ (figure 5.20e). Signal-like events are expected to have less energetic jets than those coming from the hadronic WW or $q\bar{q}$ processes;

6. the angle between the two most energetic jets, $\boldsymbol{\alpha_{j1j2}}$, (figure 5.20f).

The discriminant variables, $\ln(\mathcal{L}_S/\mathcal{L}_B)$, for data, SM expectation and signal are shown in figure 5.21.

5.3.2 CC $b' \to cW$ decay

In the CC $b' \to cW$ decay mode, two topologies were searched for ($ccqqqq$ and $ccqql\nu$). These topologies correspond to the case where one W decays into hadrons and the other decays into quarks or leptons, respectively, originating final states with six jets or four jets and one lepton.

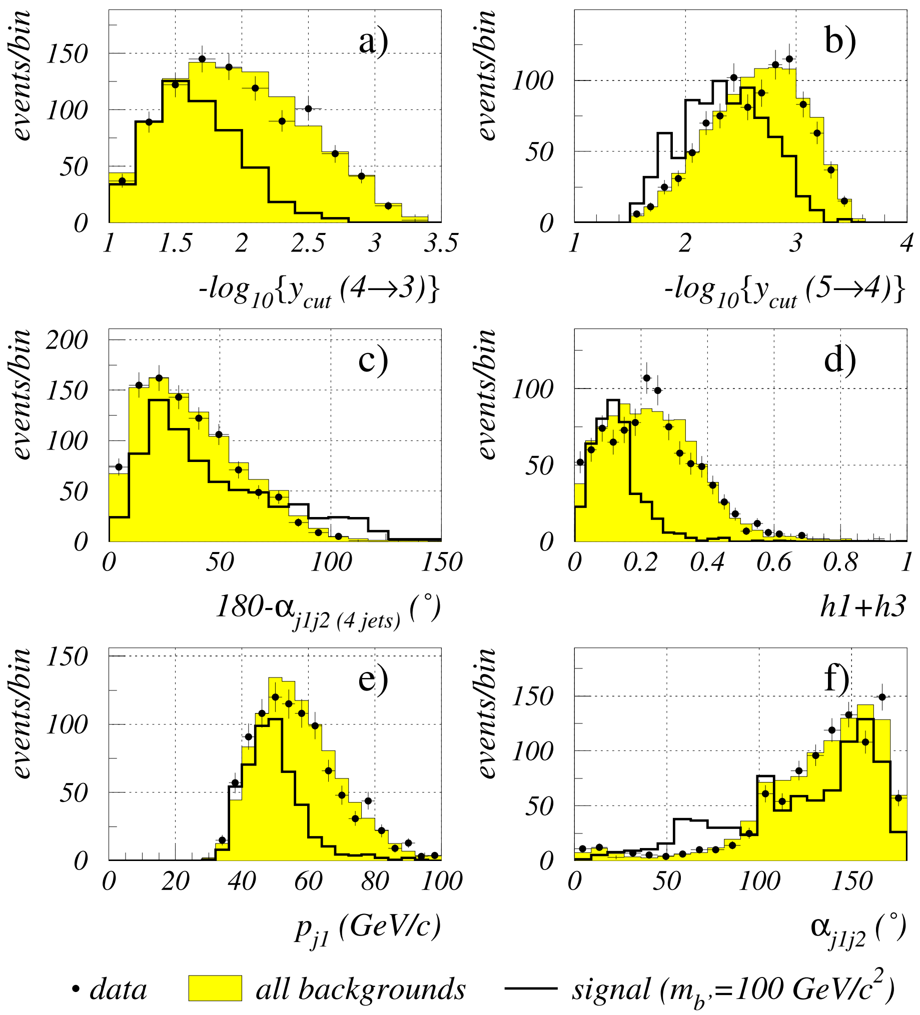

Figure 5.20: *bbqqqq topology: variables based on which the PDFs were built. The data and SM expectation distributions for* $\sqrt{s} = 202 - 207$ *GeV are shown: (a)* $-\log_{10}[y_{cut}(4 \to 3)]$*, (b)* $-\log_{10}[y_{cut}(5 \to 4)]$*, (c)* $180 - \alpha j1j2(4jets)$*, where* $\alpha j1j2(4jets)$ *is the angle (in degrees) between the two most energetic jets with the events clustered into four jets (see text for explanation), (d) the* $h1 + h3$ *Fox-Wolfram momenta sum, (e) the momentum of the most energetic jet and (f) the angle between the two most energetic jets. The signal distributions for* $m_{b'} = 100$ *GeV/*c^2 *and* $\sqrt{s} = 205$ *GeV are also shown with arbitrary normalization.*

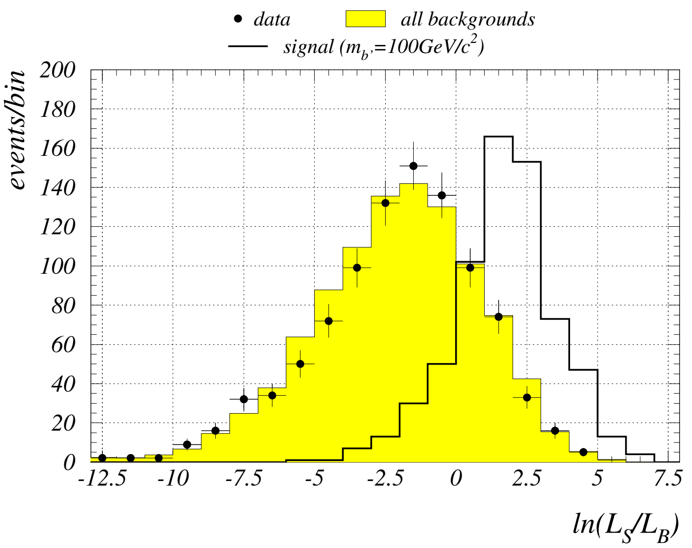

Figure 5.21: *bbqqqq topology: the discriminant variables,* $\ln(\mathcal{L}_S/\mathcal{L}_B)$*, for data and SM expectation (*$\sqrt{s} = 202 - 207$ *GeV) are shown. The signal distribution for* $m_{b'} = 100$ *GeV/*c^2 *and* $\sqrt{s} = 205$ *GeV is also shown.*

Similarly to the previous analyses a first selection, followed by a probabilistic analysis, was done. PDFs, based on relevant distributions, were used to evaluate the signal and background likelihoods.

ccqqqq topology

The CC *ccqqqq* final state is similar to the previously discussed FCNC *bbqqqq*. As no *b*-quarks tag was done, the main difference arrises from the difference of masses between the W and the Z. The same analysis was adopted for both topologies and the number of data candidates (and SM expectation) that passed the first level of selection is the same (table 5.8). The signal distributions for the *ccqqqq* final state are shown in figure 5.22.

Naturally, the differences between the two signals are reflected in a slight change in the efficiency values. The $\varepsilon(m_{b'} = 100$ GeV/$c^2)$ for the CC six jets final state are shown in table 5.9. The efficiency values for the other b' masses are within 6.1%.

$\sqrt{s}$ (GeV)	$\varepsilon(m_{b'} = 100$ GeV/$c^2)$ (%)
196	63.6±2.6
200	68.0±2.6
202	63.6±2.6
205	67.3±2.6
207	66.3±2.6
206*	66.0±2.6

Table 5.9: *ccqqqq topology: the signal efficiency,* ε*, for* $m_{b'} = 100$ *GeV/* c^2 *is shown. The overall efficiency is* $\varepsilon \times BR_{WW\rightarrow qqqq}$.

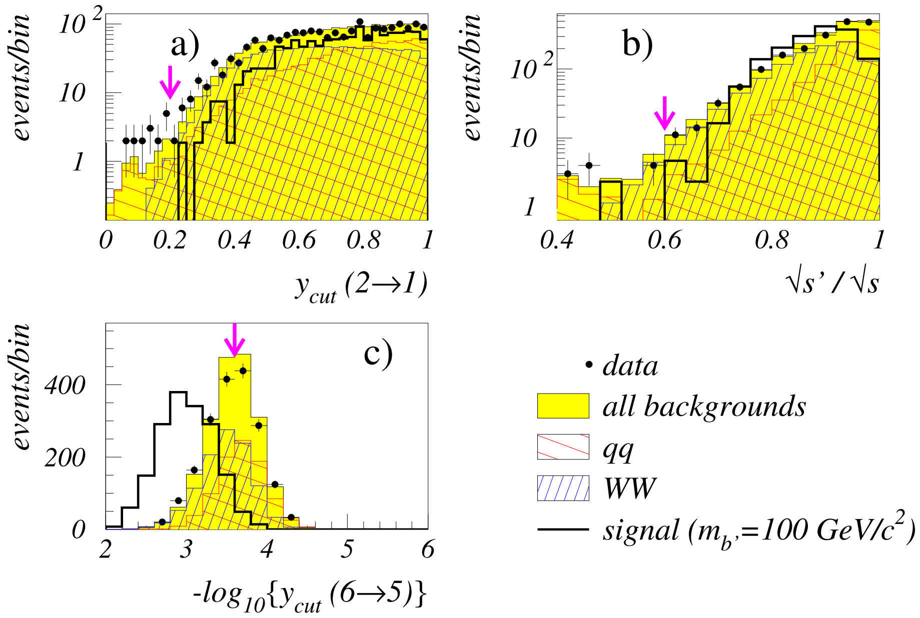

Figure 5.22: *ccqqqq topology: comparison of data and background expectation at* $\sqrt{s} =$ 202 − 207 *GeV. The distributions of (a)* $y_{cut}(2 \to 1)$*, (b)* $\sqrt{s'}/\sqrt{s}$ *and (c)* $-\log_{10}[y_{cut}(6 \to 5)]$ *are shown. The signal distributions for* $m_{b'} = 100$ *GeV/* c^2 $\sqrt{s} = 205$ *GeV are also shown with arbitrary normalization. The arrows show the cuts applied at the first level of selection.*

The PDFs for this topology were built based on the same distributions as the FCNC six jets topology and are shown in figure 5.23.

The discriminant variables, $\ln(\mathcal{L}_S/\mathcal{L}_B)$, for data, SM expectation and signal are shown in figure 5.24.

ccqqlν topology

The *ccqqlν* topology is characterized by the presence of four jets (two of them having low energy) and one energetic lepton. The invariant mass of the lepton and the missing energy/momentum should be around the W mass.

All events were clustered into four jets and were required to have more than 15 tracks in the final state. They were divided in three samples, according to the lepton flavour identification (e, μ and *no-id* samples, as discussed in section 5.2). The first level of selection, common to the three samples, was done by rejecting monojet-like events with $-\log_{10}[y_{cut}(2 \to 1)] > 0.7$. Furthermore, the most energetic track assigned to the first jet had to have a momentum below $0.1\sqrt{s}$ (to avoid a relatively energetic but not well isolated lepton in the jet). The events in the *no-id* sample were also required to have only one track assigned to the lepton. The distributions of these variables are shown in figures 5.25 and 5.26. The number of selected data candidates and SM expectation is shown in table 5.10. The background composition is about 82% of WW, 7% of $q\bar{q}$ and 11% of ZZ in the e sample, 97% of WW, 2% of $q\bar{q}$ and 1% of ZZ in the μ sample and 84% of WW, 9% of $q\bar{q}$ and 7% of ZZ in the *no-id* sample.

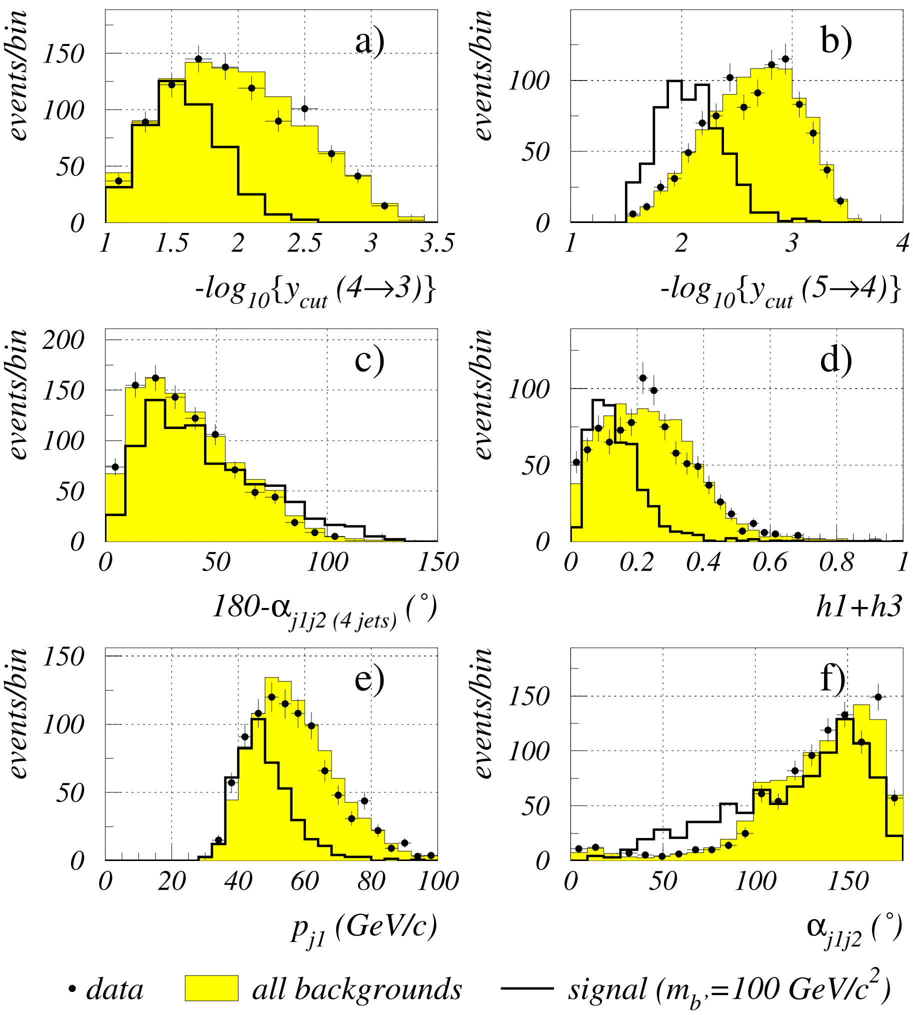

Figure 5.23: *ccqqqq topology: variables based on which the PDFs were built. The data and SM expectation distributions for* $\sqrt{s} = 202 - 207$ *GeV are shown: (a)* $-\log_{10}[y_{cut}(4 \to 3)]$*, (b)* $-\log_{10}[y_{cut}(5 \to 4)]$*, (c)* $180 - \alpha j1j2(4jets)$*, where* $\alpha j1j2(4jets)$ *is the angle (in degrees) between the two most energetic jets with the events clustered into four jets (see text for explanation), (d) the* $h1 + h3$ *Fox-Wolfram momenta sum, (e) the momentum of the most energetic jet and (f) the angle between the two most energetic jets. The signal distributions for* $m_{b'} = 100$ *GeV/*c^2 $\sqrt{s} = 205$ *GeV are also shown with arbitrary normalization.*

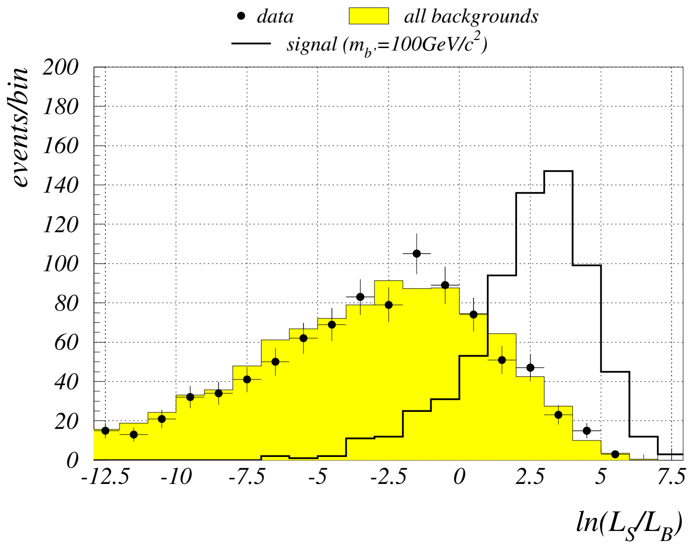

Figure 5.24: *ccqqqq topology: the discriminant variables,* $\ln(\mathcal{L}_S/\mathcal{L}_B)$, *for data and SM expectation* ($\sqrt{s}$ = 202 − 207 *GeV) are shown. The signal distribution for* $m_{b'}$ = 100 *GeV*/c^2 *and* $\sqrt{s}$ = 205 *GeV is also shown.*

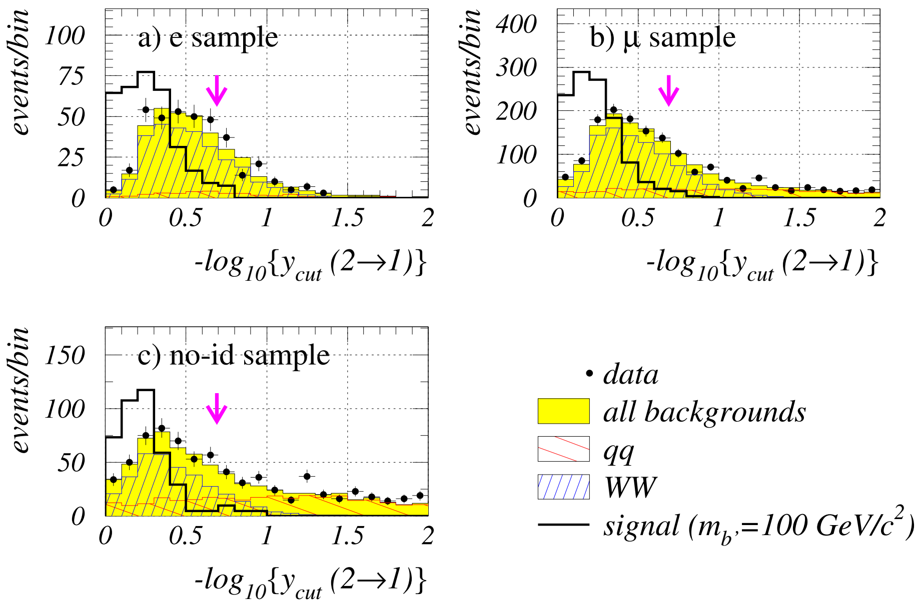

Figure 5.25: *ccqqlν topology: distributions before the first selection level.* $-\log_{10}[y_{cut}(2 \rightarrow 1)]$ *for* $\sqrt{s}$ = 202 − 207 *GeV is shown: (a) e sample, (b) μ sample and (c)* no-id *sample. The signal* ($m_{b'}$ = 100 *GeV*/c^2 *and* $\sqrt{s}$ = 205 *GeV) normalization is arbitrary. The arrows represent cuts applied at the first level of selection.*

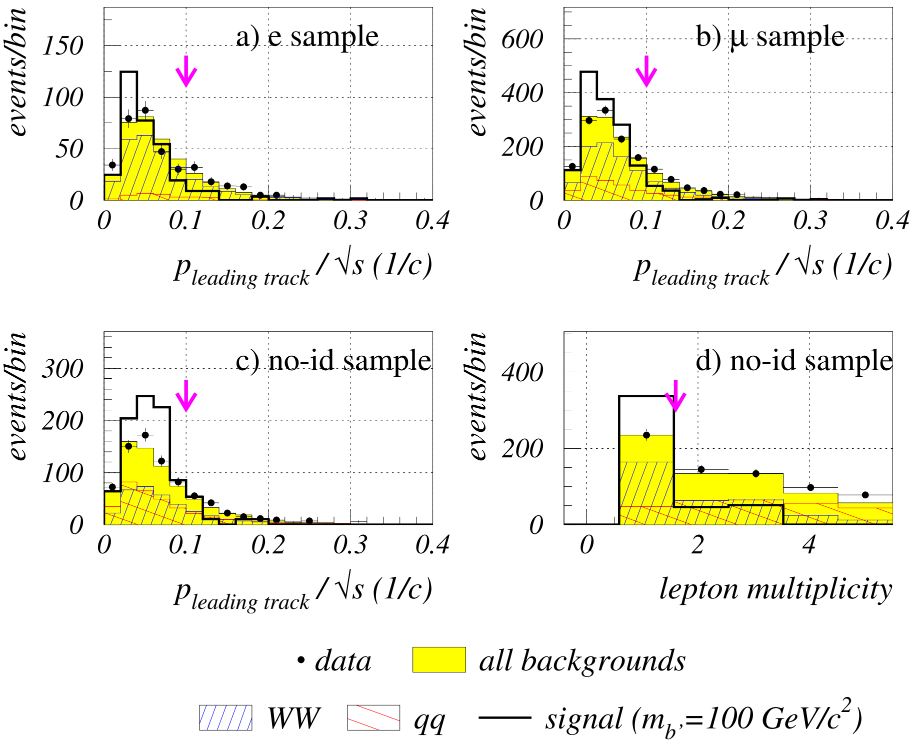

Figure 5.26: *ccqqlν topology: distributions before the first selection level. The ratio between the momentum of the most energetic track of the first jet and $\sqrt{s}$ for $\sqrt{s}$ = 202 − 207 GeV is shown: (a) e sample, (b) μ sample and (c)* no-id *sample. (d) The multiplicity of tracks assigned to the lepton in the* no-id *sample is also shown. The signal ($m_{b'}$ = 100 GeV/c^2 and $\sqrt{s}$ = 205 GeV) normalization is arbitrary. The arrows represent cuts applied at the first level of selection.*

$\sqrt{s}$ (GeV)	data (SM expectation)		
	e	μ	*no-id*
196	65 (51.1±1.4)	53 (56.1±1.5)	38 (34.4±1.4)
200	54 (58.1±1.7)	63 (59.9±1.6)	40 (35.0±0.7)
202	30 (27.8±0.8)	21 (28.4±0.8)	13 (16.9±0.7)
205	56 (50.8±1.5)	66 (53.6±1.5)	32 (33.3±1.4)
207	53 (53.8±1.6)	48 (57.2±1.6)	35 (33.8±1.4)
206*	31 (37.2±1.4)	42 (39.3±1.1)	21 (23.4±1.0)
total	289 (278.8±3.5)	293 (294.5±3.4)	179 (176.8 ± 2.8)

Table 5.10: *ccqqlν topology: number of selected data events and SM expectation after the first selection level for each sample and centre-of-mass energy.*

The signal efficiencies for $m_{b'} = 100$ GeV/c^2 are shown in table 5.11. The efficiency values for the other b' masses are within 3.3%, 3.6% and 1.8% for the e, μ and *no-id* samples, respectively.

$\sqrt{s}$ (GeV)	$\varepsilon(m_{b'} = 100\text{GeV}/c^2)$ (%)		
	e	μ	*no-id*
196	15.0±1.2	19.7±1.4	5.2±0.7
200	13.5±1.2	17.0±1.3	5.7±0.7
202	15.0±1.2	17.0±1.3	5.2±0.7
205	15.1±1.2	18.8±1.4	5.3±0.7
207	14.2±1.2	17.1±1.3	5.7±0.7
206*	11.8±1.1	16.3±1.3	6.1±0.7

Table 5.11: *ccqqlν topology: signal efficiencies, ε, for a b' mass of 100 GeV/c^2. The overall efficiency is $\varepsilon \times BR_{WW\to qql\nu}$.*

After this first level of selection, PDFs were built based on the following distributions (figures 5.27, 5.28 and 5.29 for the e, μ and *no-id* samples, respectively):

1. the $\boldsymbol{h1 + h3}$ Fox-Wolfram momenta sum. Signal-like events, characterized by a four jets structure, are expected to have smaller values of $h1 + h3$ than the background-like events (with two jets);

2. $\boldsymbol{-\log_{10}[y_{cut}(4 \to 3)]}$. This variable was also used to distinguish the four jet like events from those characterized by a two jet structure (*e.g.* semileptonic WW and qq backgrounds);

3. the invariant mass of the jets, $\boldsymbol{m_{j1j2}}$, defined as $\sqrt{p_{j1} \cdot p_{j2}(1 - \cos\alpha_{j1j2})}$, where p_{j1} (p_{j2}) is the momentum of the first (second) jet with the events clustered into two jets and α_{j1j2} is the angle between them. The two jet clustering was adopted for background rejection;

4. the $\boldsymbol{\sum_i ||\vec{p}_i||}$, where $\vec{p}_i$ is the momentum of each track in the same hemisphere

as the lepton[10]. This variable is expected to be small for the semileptonic WW events. As the two W are produced with low boost, the lepton and the jets are produced almost back-to-back (and consequently there should be no energetic tracks near the lepton);

5. $\mathbf{180^\circ - \alpha_{j1j2}}$, where α_{j1j2} is the angle between the two most energetic jets of the event (with the events clustered into four jets). For the signal events, the two most energetic jets are expected to come from the decay of one of the two W (produced by the decay $b'\bar{b}' \to cW\bar{c}W$). As the W are produced with a small boost, the angle between these two jets is, most of the times, bigger than α_{j1j2} for the background events (characterized mainly by a two jet structure);

6. the angle between the lepton and the missing momentum, $\boldsymbol{\alpha_{l\nu}}$. Due to the kinematic differences between signal and background, this variable is expected to have larger values for the signal.

The discriminant variable distributions of events belonging to the e, μ and *no-id* samples are shown in figure 5.30.

If no lepton is detected, the $ccqql\nu$ final state becomes very similar to the FCNC $bbqq\nu\nu$ topology (section 5.3.1). In order to improve the signal efficiency, preselected events with no lepton detected were kept in a fourth sample[11] (named *no lepton* sample). For this sample, the same cuts adopted to the FCNC $bbqq\nu\nu$ topology analysis were chosen (*c.f.* figure 5.31). The same set of variables was used to build the PDFs (figure 5.32). The signal efficiencies for this sample can be found in table 5.12.

$\sqrt{s}$ (GeV)	$\varepsilon(m_{b'} = 100$ GeV/c^2) (%)	
	first level of selection	$\chi^2/n.d.f.$ cut
196	15.0±1.2	7.7±0.9
200	15.7±1.3	7.0±0.8
202	15.0±1.2	7.7±0.9
205	17.4±1.3	8.9±0.9
207	16.6±1.3	10.0±1.0
206*	16.7±1.3	8.9±0.9

Table 5.12: *$ccqq(l)\nu$ topology (*no lepton *sample): the signal efficiency, ε, for $m_{b'} =$ 100 GeV/c^2 is shown after the first level of selection and after the $\chi^2/n.d.f.$ cut. The overall efficiency is $\varepsilon \times BR_{WW\to qql\nu}$. The efficiency values for the other b' masses are within 3.3%.*

The discriminant variable distributions of the *no lepton* sample events are shown in figure 5.33.

[10] A track is considered to be in the same hemisphere of the lepton if their angle is less than 90°.

[11] Events assigned to this sample were required to have no isolated photons or leptons and a missing energy above 50 GeV.

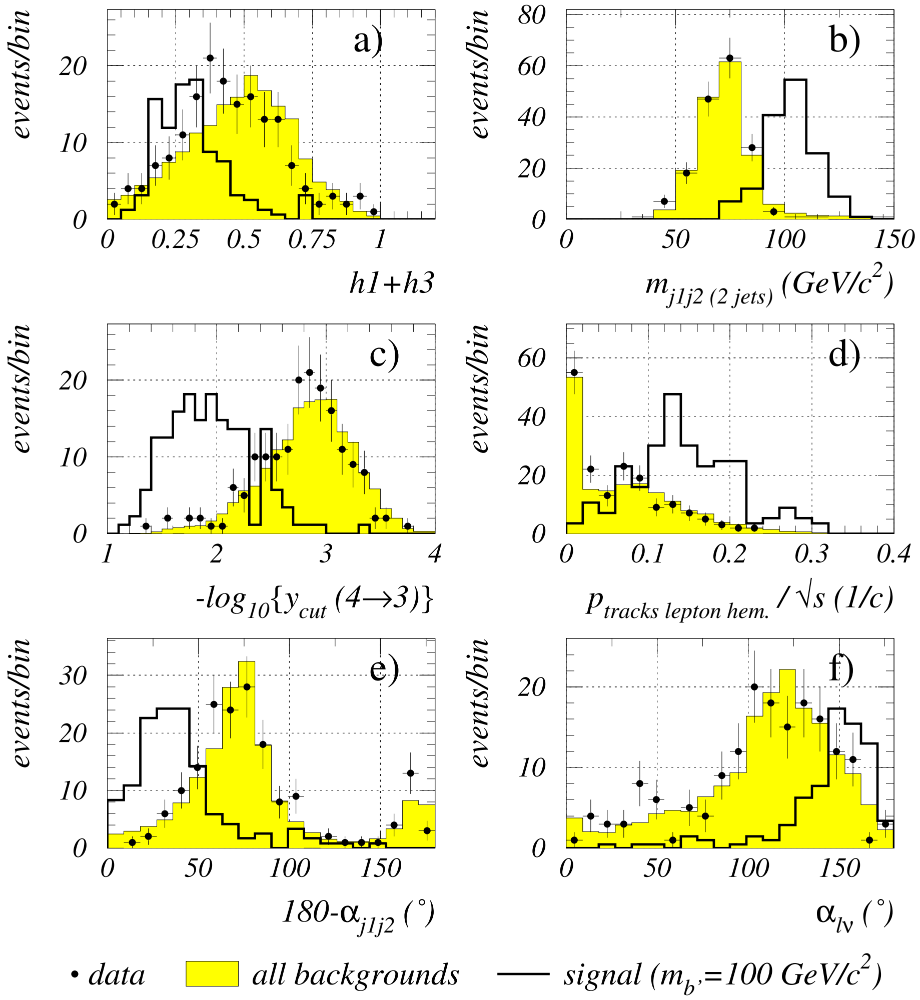

Figure 5.27: *ccqqlν topology (e sample): variables based on which the PDFs were built. The data events and background expectation for* $\sqrt{s} = 202 - 207$ *GeV are shown: (a) the* $h1 + h3$ *Fox-Wolfram momenta sum, (b) the invariant mass of the two jets with the events clustered into two jets (see text for explanation), (c)* $-\log_{10}[y_{cut}(4 \to 3)]$*, (d)* $\sum_i ||\vec{p}_i||$*, where* $\vec{p}_i$ *is the momentum of each track in the same hemisphere as the lepton, (e)* $180 - \alpha_{j1j2}$*, where* α_{j1j2} *is the angle (in degrees) between the two most energetic jets and (f) the angle between the lepton and the missing momentum. Signal distributions for* $m_{b'} = 100$ *GeV/* c^2 *and* $\sqrt{s} = 205$ *GeV are also shown with arbitrary normalization.*

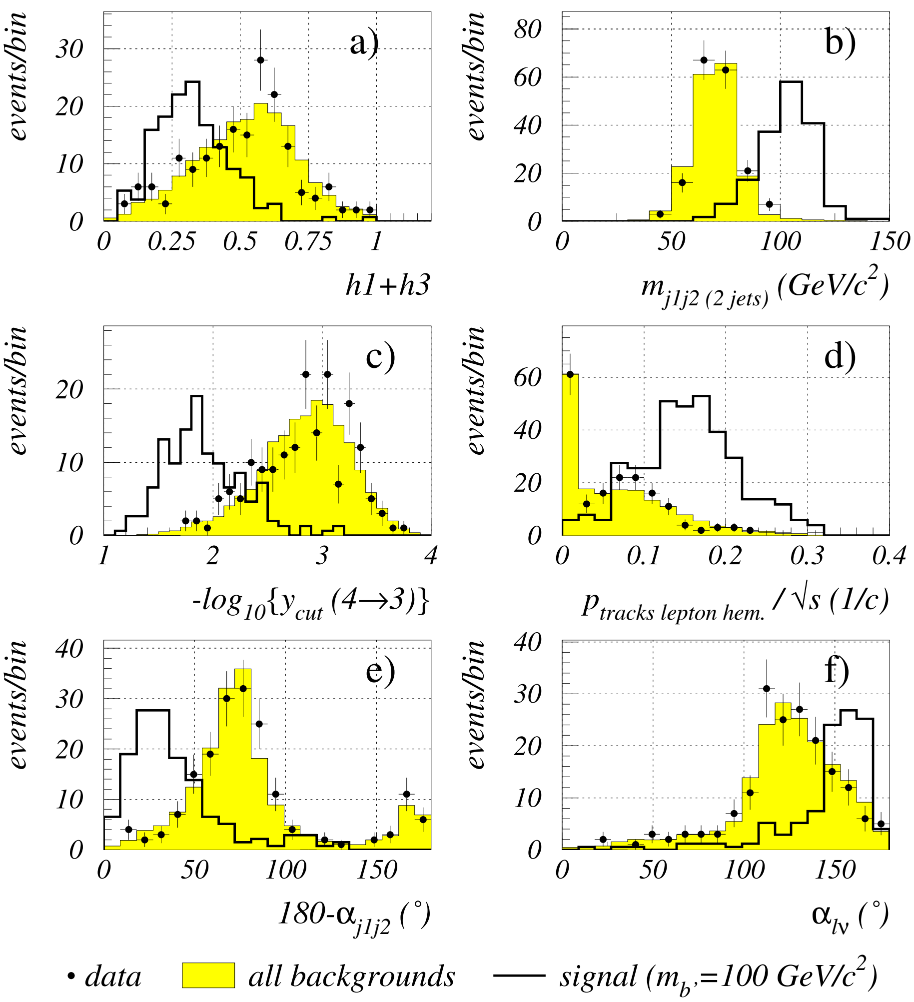

Figure 5.28: *ccqqlν topology (μ sample): variables based on which the PDFs were built. The data events and background expectation for $\sqrt{s} = 202 - 207$ GeV are shown: (a) the $h1 + h3$ Fox-Wolfram momenta sum, (b) the invariant mass of the two jets with the events clustered into two jets (see text for explanation), (c) $-\log_{10}[y_{cut}(4 \to 3)]$, (d) $\sum_i ||\vec{p}_i||$, where $\vec{p}_i$ is the momentum of each track in the same hemisphere as the lepton, (e) $180 - \alpha_{j1j2}$, where α_{j1j2} is the angle (in degrees) between the two most energetic jets and (f) the angle between the lepton and the missing momentum. Signal distributions for $m_{b'} = 100$ GeV/ c^2 and $\sqrt{s} = 205$ GeV are also shown with arbitrary normalization.*

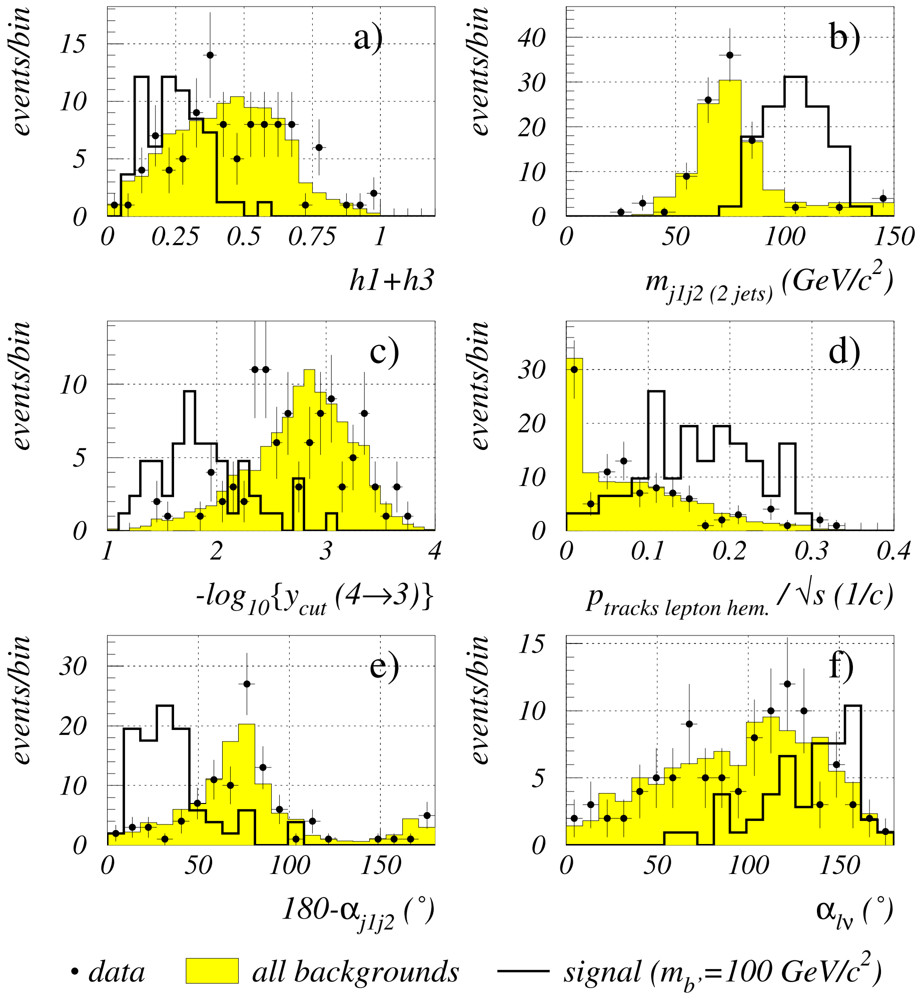

Figure 5.29: *ccqqlν topology (*no-id *sample): variables based on which the PDFs were built. The data events and background expectation for* $\sqrt{s} = 202 - 207$ *GeV are shown: (a) the* $h1 + h3$ *Fox-Wolfram momenta sum, (b) the invariant mass of the two jets with the events clustered into two jets (see text for explanation), (c)* $-\log_{10}[y_{cut}(4 \to 3)]$*, (d)* $\sum_i ||\vec{p}_i||$*, where* $\vec{p}_i$ *is the momentum of each track in the same hemisphere as the lepton, (e)* $180 - \alpha_{j1j2}$*, where* α_{j1j2} *is the angle (in degrees) between the two most energetic jets and (f) the angle between the lepton and the missing momentum. Signal distributions for* $m_{b'} = 100$ *GeV/* c^2 *and* $\sqrt{s} = 205$ *GeV are also shown with arbitrary normalization.*

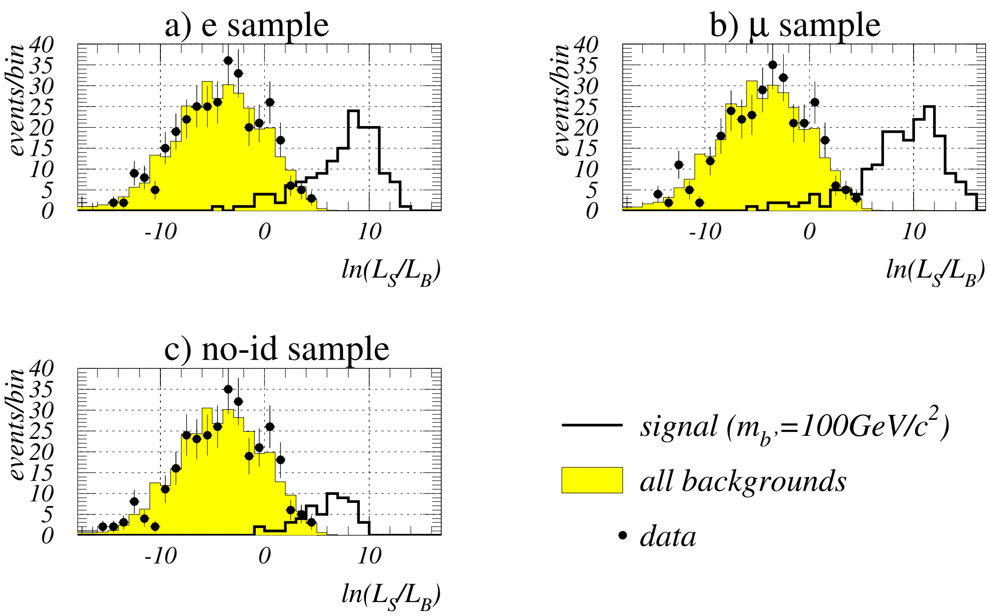

Figure 5.30: *ccqqlν topology: the discriminant variables,* $\ln(\mathcal{L}_S/\mathcal{L}_B)$*, for data and SM expectation (*$\sqrt{s}$ $=$ $202-207$ *GeV) are shown. The signal distributions for* $m_{b'}$ $=$ 100 *GeV/*c^2 *and* $\sqrt{s}$ $=$ 205 *GeV is also shown. According to the lepton flavour identification, events were separated into different samples (see text for further explanation): (a) e sample, (b)* μ *sample and (c)* no-id *sample.*

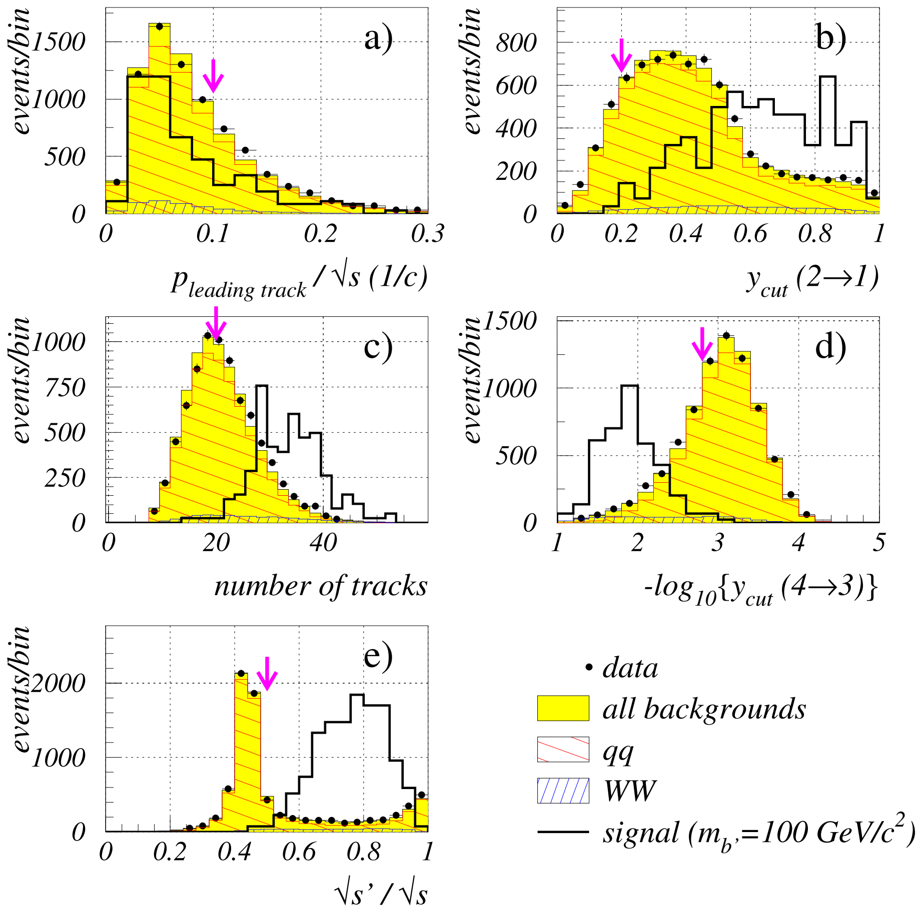

Figure 5.31: *ccqq(l)ν topology (*no lepton *sample): first level of selection. Data and SM expectation distributions for* $\sqrt{s} = 202 - 207$ *GeV are shown: (a) the ratio between the momentum of the most energetic particle of the first jet and* $\sqrt{s}$*, (b)* $y_{cut}(2 \to 1)$*, (c) the multiplicity of charged tracks, (d)* $-\log_{10}[y_{cut}(4 \to 3)]$ *and (e)* $\sqrt{s'}/\sqrt{s}$*. The signal distributions for* $m_{b'} = 100$ *GeV/*c^2 *and* $\sqrt{s} = 205$ *GeV are also shown with arbitrary normalization. The arrows represent the cuts applied at the selection level.*

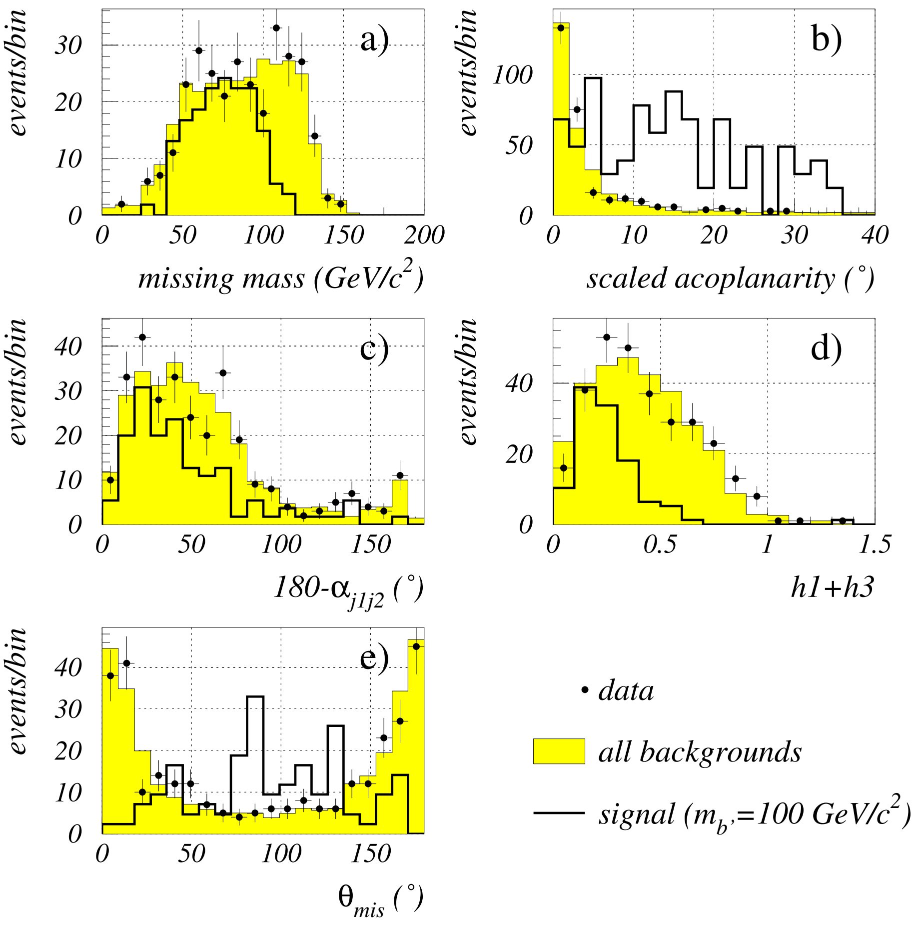

Figure 5.32: *ccqq(l)ν topology (*no lepton *sample): distribution of the variables based on which the PDFs were built. The data, SM background for* $\sqrt{s} = 202 - 207$ *GeV are shown: (a) the missing mass, (b)* $Acop_{j_1 j_2} \times \min(\sin\theta_{j_1}, \sin\theta_{j_2})$*, where* $j_{1,2}$ *are the first and second jets of the event, with the events clustered into two jets, (e) the acolinearity, defined as* $180 - \alpha_{j_1 j_2}$*, (d) the sum of the first and third Fox-Wolfram momenta and (e) the polar angle of the missing momentum. The signal distributions for* $m_{b'} =$ 100 *GeV/* c^2 *and* $\sqrt{s} = 205$ *GeV are also shown with arbitrary normalization.*

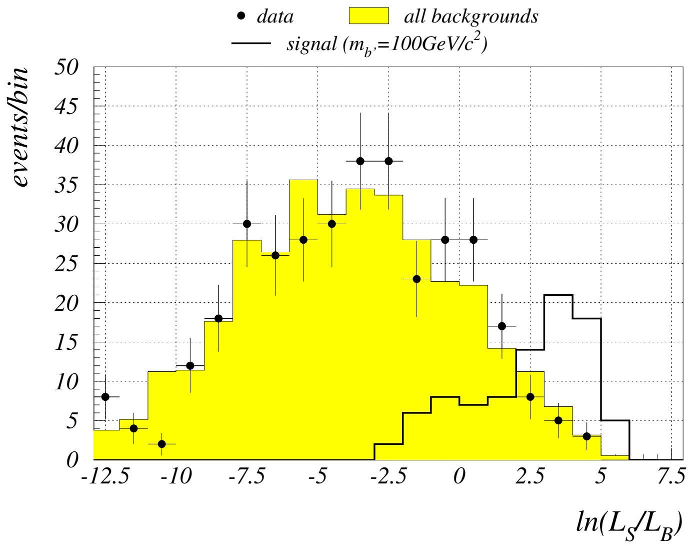

Figure 5.33: *ccqq(l)ν topology (*no lepton *sample): the discriminant variables,* $\ln(\mathcal{L}_S/\mathcal{L}_B)$*, for data and SM expectation (*$\sqrt{s} = 202 - 207$ *GeV) are shown. The signal distribution for* $m_{b'} = 100$ *GeV/*c^2 *and* $\sqrt{s} = 205$ *GeV is also shown.*

Chapter 6

RESULTS

In the absence of any evidence of a b' pair production signal, limits on $BR_{b'\to bZ}$ and $BR_{b'\to cW}$ were derived. In section 6.1 these limits are presented and in section 6.2 the systematic error evaluation is discussed. In section 6.3 the experimental limits on $BR_{b'\to bZ}$ and $BR_{b'\to cW}$ are compared with theoretical predictions, in order to constrain the possible values of an extended 4×4 CKM matrix elements ratio.

6.1 Limits on $BR_{b'\to bZ}$ and $BR_{b'\to cW}$

No evidence for double production of b'-quarks was found at LEP-II, after the analysis of the data collected by the DELPHI experiment.

Data and background discriminant variables for the FCNC (CC) topologies, the respective signal efficiencies and data luminosity collected at the various centre-of-mass energies were combined to derive 95% confidence level limits on the number of signal events at each b' mass. Assuming the SM cross-section for the pair production of heavy quarks at LEP[1], these limits were converted into limits on the branching ratios corresponding to the $b'\to bZ$ and $b'\to cW$[2]. The modified frequentist likelihood method [100] was used. Discriminant variables corresponding to each topology and centre-of-mass energy bin were treated as independent channels. For each b' mass (in the range between 96 and 103 GeV/c^2, with 1 GeV/c^2 steps), only the channels with $\sqrt{s} > 2\,m_{b'}(1/c^2)$ were considered (table 6.1).

The median expected limit, *i.e.* the limit which would be obtained if the data were exactly described by the SM, was also calculated. In figure 6.1 the observed and expected limits on $BR_{b'\to bZ}$ and $BR_{b'\to bZ}$ are shown. The 1σ and 2σ bands around the expected limit are also shown. The observed and expected limits in both the FCNC and CC channels are statistically compatible. These limits were evaluated taking into account the systematic errors contribution, which will be the subject of the next section.

[1]The cross-section $e^+e^-\to b'\bar{b}'$ was calculated with PYTHIA, as discussed in section 4.1.

[2]This procedure is explained in appendix A.

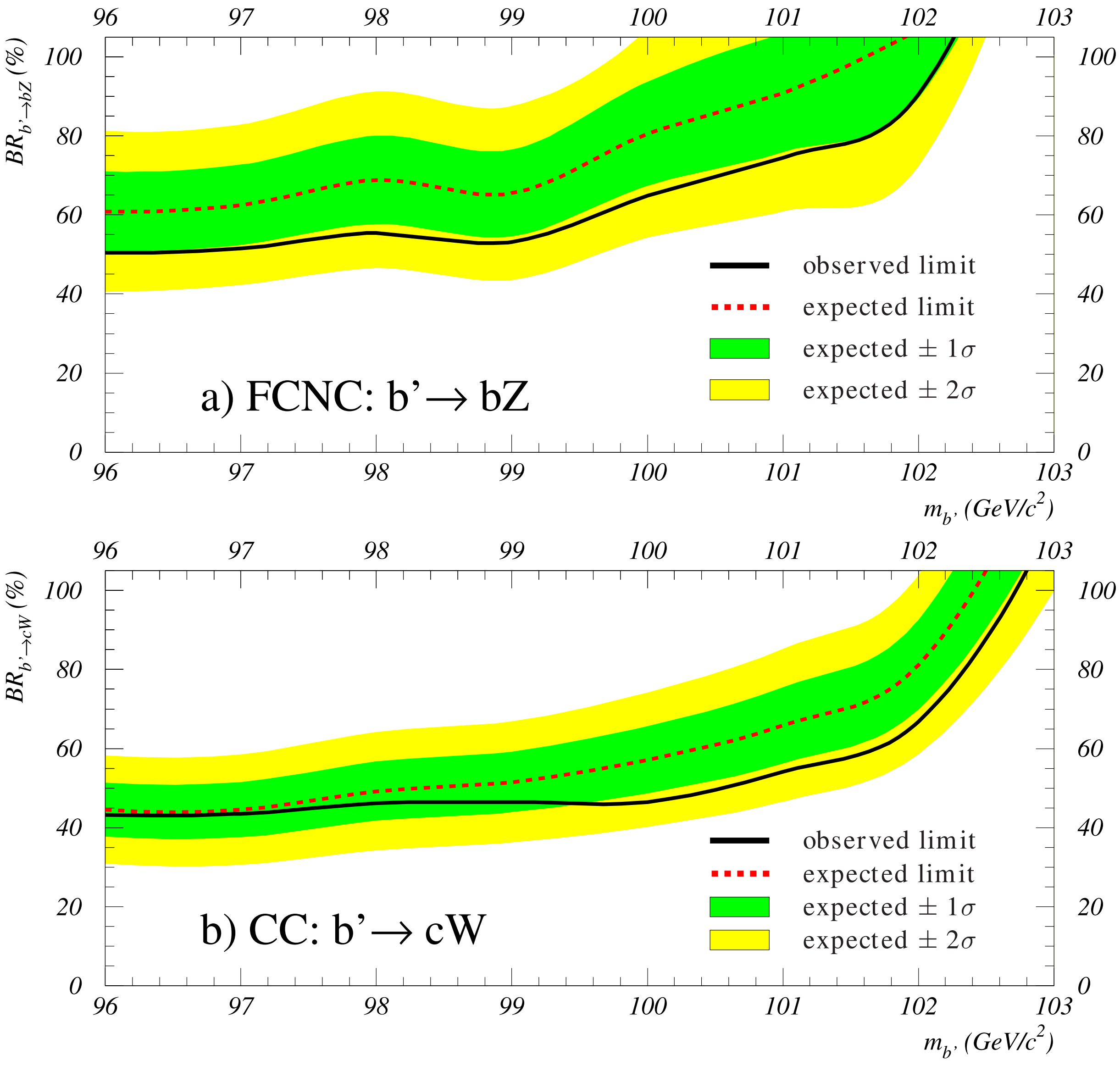

Figure 6.1: *Observed and expected (median) upper limits at 95% confidence level on a) $BR_{b'\to bZ}$ and b) $BR_{b'\to cW}$. The 1σ and 2σ bands around the expected median limit are also shown. Systematic errors were taken into account in the limit evaluation.*

b' mass (GeV/c^2)	used data samples 196	200	202	205	207	206*
96	×	×	×	×	×	×
97	×	×	×	×	×	×
98		×	×	×	×	×
99		×	×	×	×	×
100			×	×	×	×
101				×	×	×
102				×	×	×
103					×	×

Table 6.1: *Data samples used to derive the limits for each b' mass (*c.f. *table 3.4).*

6.2 Systematic errors study

The analyses stability study and the limit evaluation requires the estimation of the systematic errors. The effect of the uncertainties associated to the background cross-section evaluation, signal generation and discriminant variable (likelihood ratio) construction was studied. The repercussion of the systematic errors on the derivation of the expected limits on $BR_{b' \to bZ}$ and $BR_{b' \to cW}$ was also investigated. Each systematic error source was studied independently and compared with the reference values[3]. This study was done for each topology, centre-of-mass energy and b' mass. The method used to propagate the systematic uncertainties in the limit calculation is briefly described in appendix A. The considered systematic uncertainties sources are enumerated below.

- **SM background cross-sections**
  The inaccuracy of the cross-section description for the different SM background processes at LEP is typically small, except for the "$\gamma\gamma$" processes [101, 102]. The uncertainty on the cross-sections calculated within the acceptance region of the dominant background processes for the present analyses is 1% for WW and qq, 2% for ZZ and 15% for "$\gamma\gamma$" [103]. The relative effect of these uncertainties on the number of expected background events for each topology is below 6% and it is shown in table 6.2.

- **Signal generation: hadronization modeling**
  The uncertainties associated to the hadronization and fragmentation modeling of the quarks present in the signal final states were studied. The Lund symmetric fragmentation function was tested and compared with the scheme were the b and c quark masses are taken into account and also with the scheme where the mass effect is introduced in the fragmentation function via heavy hadron production[4] [86]. Signal samples were simulated for each of these three hadronization schemes ($m_{b'} = 96$ GeV/c^2 and $m_{b'} = 102$ GeV/c^2 samples were simulated

[3]For each change corresponding to a considered systematic uncertainty, all the described analyses procedure was repeated and the effect on the limit evaluation was calculated. Only one change was done at each time.

[4]By default PYTHIA uses this last scheme (mass effect introduced in the fragmentation function via heavy hadron production).

for the 196 GeV and 207 GeV centre-of-mass energies). The maximum relative change on ε was 19.8%. Conservatively[5], the effect of this systematic error was taken into account by decreasing the signal efficiency by 20%.

- **Signal generation: b' mass points generation**
  Among all the considered b' mass points (*c.f.* table 6.1), two of them were not generated [6]. In fact, as the kinematics of signal events is expected not to change significantly for two close b' mass points, the $m_{b'} = 97$ GeV/c^2 and $m_{b'} = 101$ GeV/c^2 samples were not generated (the $m_{b'} = 98$ GeV/c^2 and $m_{b'} = 100$ GeV/c^2 samples, respectively, were used instead). In order to study the systematic uncertainty due to this approach, different (but equally close) samples were used to replace to non-simulated ones[7]. The maximum relative changes obtained on the signal efficiency for each topology are shown in table 6.3.

- **Discriminant variables smoothing**
  The limited statistics of the generated events leads to some non-physical fluctuations of the discriminant variables distributions. This effect was avoided by using a smoothing algorithm. The systematic error associated to this procedure was evaluated by testing two smooths: a stronger and a softer smoothing were tested. This systematic error does not change the number of SM expected events or the signal efficiency, but it leads to some differences on the discriminant variables, which will be reflected on the limits evaluation.

The effect of each systematic error on the $BR_{b' \to bZ}$ and $BR_{b' \to cW}$ expected limits is summarized in tables 6.4 and 6.5. The shown values are the relative difference to the reference limit (calculated without any systematic error contribution). The dominant systematic error source is the hadronization scheme choice, which is below 16%. The limits presented in the previous section were calculated taken into account all the described systematic uncertainties.

6.3 Constraints on R_{CKM}

The theoretical branching ratios for the b' decays were calculated within a four generation sequential model [48, 42, 43]. If the b' is lighter than both the t and the t' quarks and $m_Z < m_{b'} < m_H$, the main b' decays are $b' \to b\,Z$ and $b' \to c\,W$. The two-body decays ($b' \to b\,\gamma$, $b' \to b\,g$) and the three body decays ($b' \to b\,e^+\,e^-$, $b' \to b\,\nu\,\bar{\nu}$, $b' \to b\,q\,\bar{q}$) are expected to have a smaller branching ratio[8] (*c.f.* chapter 2).

Using the approximate diagonality ($V_{ub'}\,V_{ub} \approx 0$ and $V_{cb'}\,V_{cb} \approx 0$) and the unitarity ($V_{ub'}\,V_{ub} + V_{cb'}\,V_{cb} + V_{tb'}\,V_{tb} + V_{t'b'}\,V_{t'b} = 0$) of the extented 4×4 CKM matrix, the

[5]The adopted strategy is considered conservative because it leads to a less stringent exclusion on the possible values of $BR_{b' \to bZ}$ and $BR_{b' \to cW}$.

[6]Each b' mass point implies the generation of several samples, corresponding to all the different $\sqrt{s}$ and topologies.

[7]The effect of this systematic error source was evaluated by using the $m_{b'} = 96$ GeV/c^2 and $m_{b'} = 102$ GeV/c^2 samples to replace the non-simulated ones.

[8]Conservatively, the branching ratios corresponding to all the three body decays plus the $b' \to b\gamma$ two-body decay was considered to be equal to $BR_{b' \to bg}$ [42, 43].

topology	maximum effect on SM expectation (%)
$bbll\nu\nu$ (e sample)	5.9
(μ sample)	5.7
(*no-id* sample)	3.4
$bbqq\nu\nu$	2.2
$bbqqqq$	1.0
$ccqqqq$	1.0
$ccqql\nu$ (e sample)	1.3
(μ sample)	1.2
(*no-id* sample)	1.5
(*no lepton* sample)	1.0

Table 6.2: *Maximum effect of the background cross-section uncertainty on the number of expected background events. The maximum relative values, calculated in relation with the reference analysis (*i.e.* without taking into account the systematic errors), are shown. A positive value means that the signal efficiency is higher in the reference analysis.*

topology	maximum effect on ε
$bbll\nu\nu$ (e sample)	-14.8
(μ sample)	19.7
(*no-id* sample)	44.1
$bbqq\nu\nu$	-13.6
$bbqqqq$	4.7
$ccqqqq$	4.7
$ccqql\nu$ (e sample)	21.9
(μ sample)	9.1
(*no-id* sample)	-21.2
(*no lepton* sample)	31.0

Table 6.3: *Effect on the signal efficiency due to the choice of different neighbour b' mass points. The maximum relative values, calculated in relation with the reference analysis (*i.e.* without taking into account the systematic errors), are shown. A positive value means that the signal efficiency is higher in the reference analysis.*

	effect on $BR_{b'\to bZ}$ (%)				
$m_{b'}$ (GeV/c^2)	background cross-sections	hadronization	$m_{b'}$ generation	($\ln \mathcal{L}_S/\mathcal{L}_B$) smooth stronger	softer
96	-3.4	-12.3	—	5.6	-1.1
97	-1.1	-11.9	-6.5	0.1	1.1
98	-2.1	-13.5	—	-1.0	-1.0
99	-2.1	-13.5	—	1.0	0.1
100	-1.7	-11.2	—	3.4	0.1
101	-0.1	-10.1	—	4.3	-0.7
102	-1.8	-12.7	-10.3	2.4	0.1

Table 6.4: *Effect of each considered systematic error source on the $BR_{b'\to bZ}$ expected limits. These values were calculated in relation with the reference limits (*i.e.* the limits calculated without taking into account the systematic errors). A positive value means that the limit evaluated with systematic error source is lower than the reference one.*

	effect on $BR_{b'\to cW}$ (%)				
$m_{b'}$ (GeV/c^2)	background cross-sections	hadronization	$m_{b'}$ generation	($\ln \mathcal{L}_S/\mathcal{L}_B$) smooth stronger	softer
96	-1.2	-10.7	—	8.3	-0.1
97	2.4	-10.7	-2.4	4.7	-1.2
98	-1.1	-12.4	—	4.6	-1.1
99	0.1	-10.0	—	3.3	-0.1
100	-5.9	-15.2	—	1.2	-1.2
101	-6.0	-15.9	—	-1.0	-1.0
102	-2.4	-12.8	-8.0	1.6	-0.1

Table 6.5: *Effect of each considered systematic error source on the $BR_{b'\to cW}$ expected limits. These values were calculated in relation with the reference limits (*i.e.* the limits calculated without taking into account the systematic errors). A positive value means that the limit evaluated with systematic error source is lower than the reference one.*

branching fractions of all possible b' decays can be written as a function of three variables: $R_{CKM} = |\frac{V_{cb'}}{V_{tb'}V_{tb}}|$, $m_{b'}$ and $m_{t'}$ [48, 42, 43].

Bounds at 95% confidence level on R_{CKM} as a function of $m_{b'}$ can be drawn, using the limits on the branching ratios ($BR_{b' \to bZ}$ and $BR_{b' \to cW}$) presented in section 6 (figure 6.1) and fixing $m_{t'} - m_{b'}$. Two extreme cases were considered: the almost degenerate case, where $m_{t'} - m_{b'} = 1$ GeV/c^2, and the case where the mass difference is close to the largest possible value, $m_{t'} - m_{b'} = 50$ GeV/c^2 [29, 48]. These limits are shown in figures 6.2 and 6.3. The upper curve in the $(R_{CKM}, m_{b'})$ plane was obtained from the limits on $BR_{b' \to cW}$. The lower curve is related to $BR_{b' \to bZ}$, which decreases with growing $m_{t'}$. This suppression is due to the GIM mechanism [17] and gets more relevant as $m_{t'}$ approaches m_t (*c.f.* figures 6.2 and 6.3).

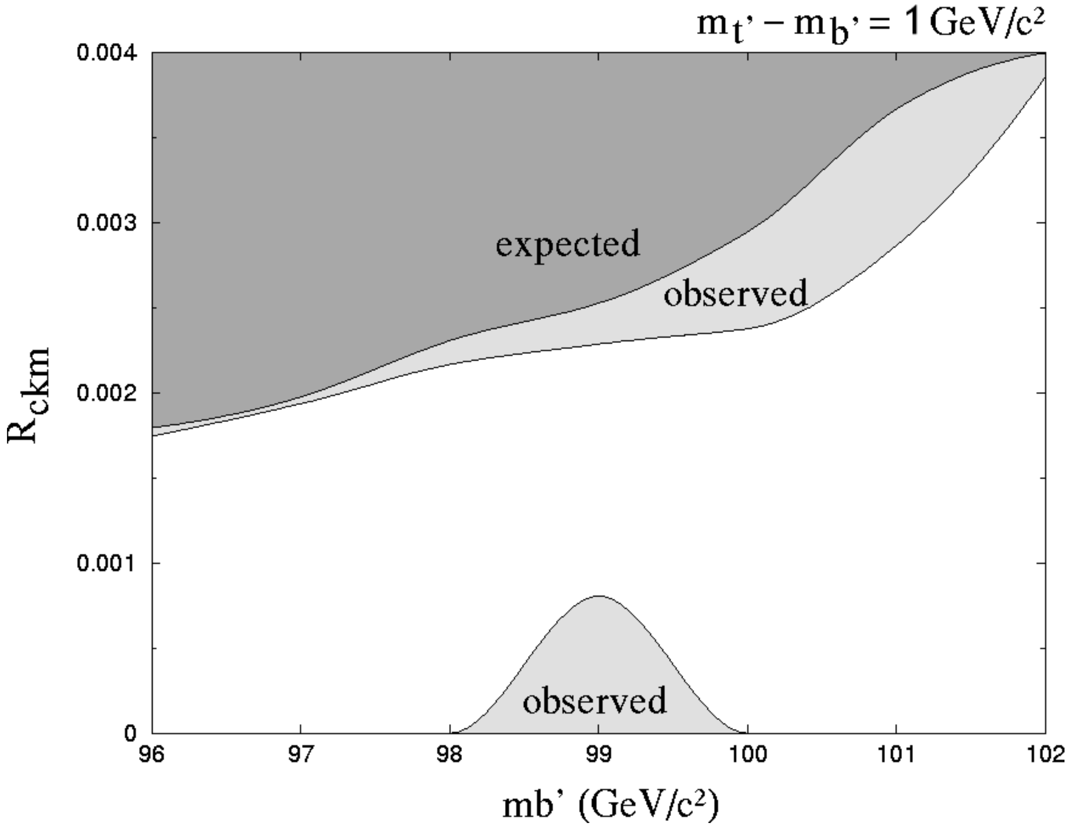

Figure 6.2: *95% confidence level excluded region in the plane (R_{CKM}, $m_{b'}$) with $m_{t'} - m_{b'} = 1$ GeV/c^2, obtained from the limits on $BR_{b' \to bZ}$ (bottom) and $BR_{b' \to cW}$ (top). The light and dark shadings correspond to the observed and expected median limits, respectively.*

The reason why there is not a lower bound on R_{CKM} for $m_{b'}$ close to 96 GeV/c^2 (figures 6.2 and 6.3).is related to the other FCNC b' decays ($b' \to bg$ and $b' \to b\gamma$) which, near the Zb threshold can dominate over $b' \to bZ$. For higher b' masses (below the Higgs mass), the $b' \to bZ$ becomes the only relevant FCNC b' decay (*c.f.* figure 2.3). Above $m_{b'} = 102$ GeV/c^2, almost all values of R_{CKM} are allowed because the experimental upper limits on $BR_{b' \to bZ}$ and $BR_{b' \to cW}$ are close to 100%.

In figure 6.4, the excluded region in the $(m_{t'}, m_{b'})$ plane is shown for $R_{CKM} =$

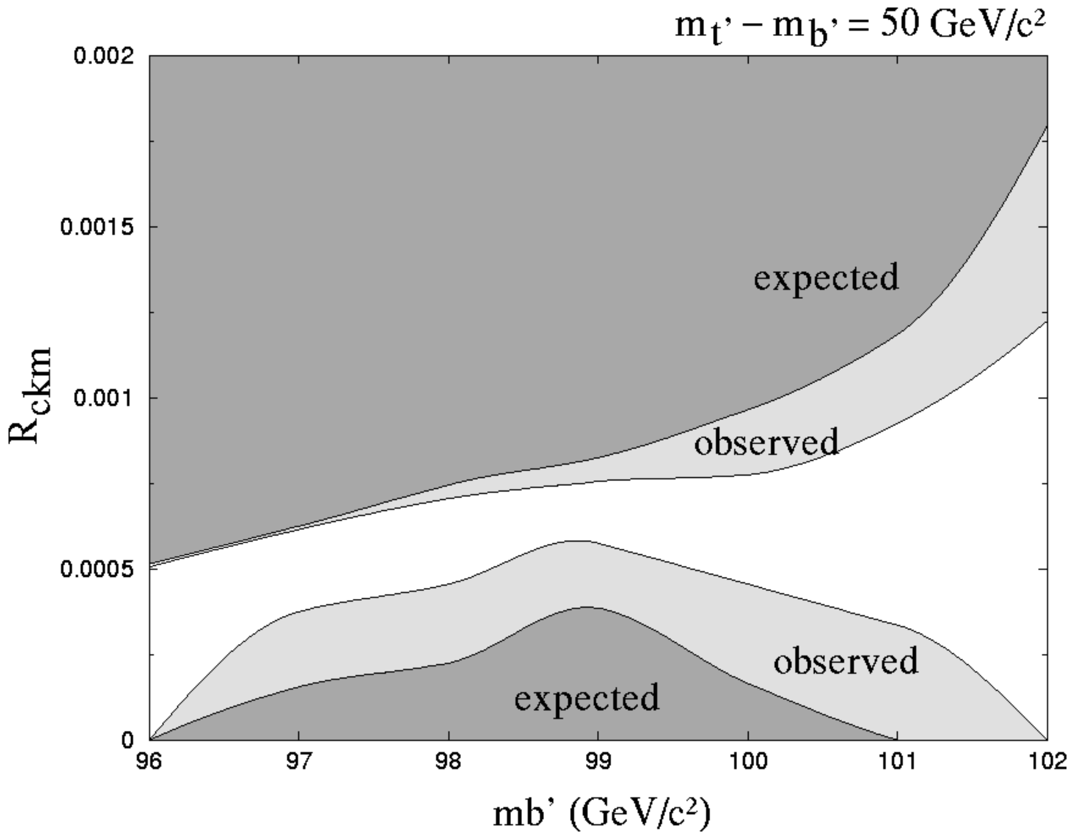

Figure 6.3: *95% confidence level excluded region in the plane (R_{CKM}, $m_{b'}$) with $m_{t'} - m_{b'} = 50$ GeV/c^2, obtained from the limits on $BR_{b' \to bZ}$ (bottom) and $BR_{b' \to cW}$ (top). The light and dark shadings correspond to the observed and expected median limits, respectively.*

2×10^{-4}. The horizontal stripe centered around the t mass was obtained from the experimental limit on $BR_{b' \to cW}$. Due to GIM mechanism, when $m_{t'} \sim m_t$, the branching ratio corresponding to the $b' \to cW$ decay is close to 100%. For higher values of R_{CKM} this band becomes larger.

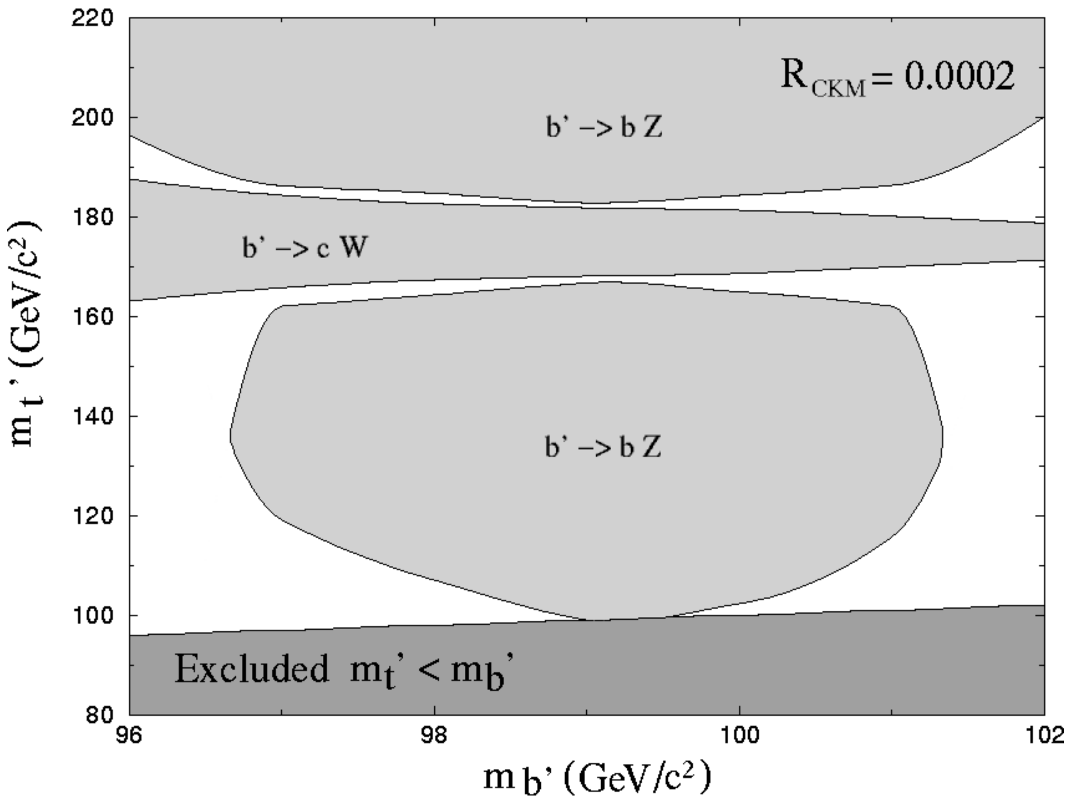

Figure 6.4: *95% confidence level excluded region in the* $(m_{t'}, m_{b'}$ *plane* ($R_{CKM} = 2 \times 10^{-4}$)*, obtained from the observed limits on* $BR_{b' \to bZ}$ *and* $BR_{b' \to cW}$*. The darkest zone (bottom of the plot) corresponds to* $m_{b'} > m_{t'}$ *and it is excluded assuming a* t' *heavier than* b'.

The CDF [62] and D$\emptyset$ [63] results on $BR_{b' \to bZ}$ and $BR_{b' \to cW}$ (*c.f.* chapter 2) can also be used to constrain the possible values of R_{CKM} [42, 43] and the excluded region grows with $m_{t'} - m_{b'}$. This is consistent with the electroweak precision data, which disfavour a fourth generation with a large mass difference between the two additional quarks. The combination of the CDF/D$\emptyset$ results with those obtained by DELPHI allow to exclude additional values of R_{CKM}. For $m_{b'} = 100$ GeV/c^2 and $m_{t'} - m_{b'} = 50$ GeV/c^2, the CDF/D$\emptyset$ analyses establishes that $6.7 \times 10^{-4} < R_{CKM} < 1.1 \times 10^{-3}$, while DELPHI resuls are compatible with $4.6 \times 10^{-4} < R_{CKM} < 7.8 \times 10^{-4}$. Hence, the combination of these limits stongly constrain the values of R_{CKM}: $6.7 \times 10^{-4} < R_{CKM} < 7.8 \times 10^{-4}$. As expected, the allowed region grows for the almost degenerate case.

Chapter 7

CONCLUSIONS

A search for the b' pair production with the DELPHI detector at LEP-II was presented. The data samples were collected with $\sqrt{s} = 196 \rightarrow 209$ GeV and the b' mass in the range between 96 and 103 GeV/c^2 was studied. Several different final states, corresponding to different b' decay modes, were considered. Specific analyses were developed for each topology. No evidence for a b' signal was found.

In the absence of a signal, 95% confidence level upper limits on $BR_{b' \rightarrow bZ}$ and $BR_{b' \rightarrow cW}$ were obtained, assuming the SM cross section for pair production of heavy quarks at LEP. These limits, which include the systematic errors contribution, were compared with the theoretical predictions within the sequential fourth generation model. Large parts of the (R_{CKM}, $m_{b'}$) plane for two extreme hypotheses on the $m_{t'} - m_{b'}$ mass difference were excluded. The possible values of $R_{CKM} = |\frac{V_{cb'}}{V_{tb'} V_{tb}}|$ were, therefore, strongly constrained: in the studied b' mass range, R_{CKM} should be less than $\sim 4 \times 10^{-3}$. This result suggests that, if the fourth generation of quarks exists, the new CKM matrix elements should have a structure similar to the known ones.

Combining the DELPHI results with those obtained by the CDF collaboration for $m_{t'} - m_{b'} = 50$ GeV/c^2, one finds that the b' with a mass of 100 GeV/c^2 is almost excluded (almost no R_{CKM} values remain possible). Nevertheless, the exclusion plots presented in chapter 6 show that, for other b' and t' masses, there is still plenty of room for a sequential b' quark. These results were presented at the Lake Louise Winter Institute 2003[1].

At this point, it should be stressed that the theoretical calculations of the branching ratios for the different b' decay modes allowed a deeper understanding of the implications of the experimental results. The definitive confirmation or exclusion of the fourth generation hypothesis requires further experimental and theoretical inputs.

In the near future, the TEVATRON Run-II data can either find an evidence for a fourth generation quark or tight the constraints on R_{CKM} (eventually leading to

[1]This conference took place at Lake Louise (Alberta, Canada) in February of 2003. Further details can be found in `http://www.phys.ualberta.ca/~llwi/`.

the exclusion of the additional sequential quarks hypothesis). With higher values for the b' pair production cross sections, due to higher centre-of-mass energy, the Large Hadron Collider (LHC) data will certainly contribute to the study of the fourth generation of quarks through both direct and indirect searches [104]. Such results are expected either to find a b' signal or to further constrain the possible R_{CKM} values in a larger $m_{b'}$ range leading, in the limit, to a definitive b' hypothesis exclusion. The existence of a fourth generation of quarks would imply several mass and decay widths precision measurements. Moreover, it is also possible that, for certain values of the new CKM matrix elements, bound states of fourth generation quarks could be formed, opening a new branch of spectroscopy studies [105].

The definitive answer to the question of the fermion families number would largely improve the present knowledge we have about the nature constituents. The existence or exclusion of a fourth generation of fermions can be an important piece of the puzzle and, therefore, it is an interesting and up to date subject of both experimental and theoretical high energy physics.

Appendix A

STATISTICAL METHODS

In the present appendix, the statistical tools used in the interpretation of the analysis results are presented. The 95% confidence level limits on $BR_{b'\to cW}$ and $BR_{b'\to bZ}$ were evaluated using the modified frequentist likelihood method [100]. A detailed review of this method can be found in [106].

A.1 Discriminant variables construction

After the sequential analyses described in chapter 5, a signal likelihood ($\mathcal{L}_S$) and a background likelihood ($\mathcal{L}_B$) were calculated for each selected event by using PDFs based on relevant physical variables. Neglecting correlations, the signal and background likelihoods for each selected event are:

$$\mathcal{L}_S = \prod_{i=1}^{n} P_i^S(x_i)\,, \qquad \mathcal{L}_B = \prod_{i=1}^{n} P_i^B(x_i)\,, \tag{A.1}$$

where n is the number of used PDFs. For the $i^{\rm th}$ signal (background) PDF, $P_i^S(x_i)$ ($P_i^B(x_i)$) is the probability that the event has the value x_i (*c.f.* figure A.1). The discriminant variable was defined as $-\ln(\mathcal{L}_S/\mathcal{L}_B)$.

A.2 Hypothesis testing and limits derivation

In the absence of a signal evidence, 95% confidence level upper limits on the number of signal events present in the data samples were derived[1]. With this purpose, a

[1]The limit on the number of signal, $n_S(BR)$, is converted into limits on the branching ratio (BR) of the decay $b' \to X$ ($X = cW$ or $X = bZ$ depending on the considered decay channel). In fact, $n_S(BR) = \mathcal{L}\times\varepsilon\times\sigma(e^+e^- \to b'\bar{b}')\times(BR_{b'\to X})^2$, where ε is the signal efficiency and $\mathcal{L}$ is the luminosity corresponding to each data sample.

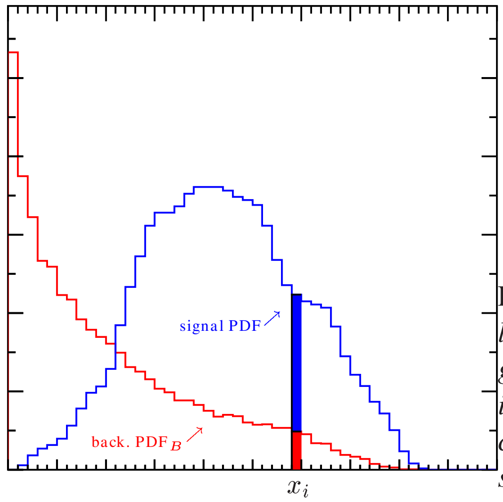

Figure A.1: *Example of the signal (background) likelihood evaluation using the signal (background) PDF. The signal (background) probability of having one specific event with value x_i is calculated as the normalized area of the corresponding histogram bin.*

statistical test variable (X_d) was built:

$$X_d = \sum_{i=1}^{N_{bins}} n_i \ln\left(1 + \frac{s_i(BR)}{b_i}\right) , \tag{A.2}$$

where the index i runs over the number of bins (N_{bins}) of the discriminant variable, and n_i, $s_i(BR)$ and b_i are the number of events in the i^{th} bin of the data, signal and background discriminant variables, respectively. The variable X_d has higher values for signal-like events than for background-like events.

The statistical test X_d was compared with the analogous statistical tests for the signal plus background (X_{s+b}) and background only (X_b) hypotheses. For the signal plus background hypothesis, the distribution of X_{s+b} was computed via iterative Monte Carlo (MC) simulation of distributions statistically compatible (according to a Poisson distribution) with the sum of the background and signal discriminant variables. For each MC iteraction, a value of X_{s+b} was computed:

$$X_{s+b} = \sum_{i=1}^{N_{bins}} n_i^{(s+b)^*} \ln\left(1 + \frac{s_i(BR)}{b_i}\right) , \tag{A.3}$$

where $n^{(s+b)^*}$ is the total number of events of the MC generated distribution obtained from the sum of the background and signal discriminant variables. Similarly, the distribution of X_b was computed using MC simulation of distributions statistically compatible with the background discriminant variable distribution and, for each MC iteration:

$$X_b = \sum_{i=1}^{N_{bins}} n_i^{b^*} \ln\left(1 + \frac{s_i(BR)}{b_i}\right) , \tag{A.4}$$

where n^{b^*} is the total number of events of the MC generated distribution obtained from the background discriminant variable distribution.

The confidence level (CL) for the number of signal events is defined as [100, 106]:

$$1 - CL = \frac{\int_0^{X_d} P_{s+b}(X)dX}{\int_0^{X_d} P_b(X)dX} , \tag{A.5}$$

where $P_{s+b}(X)$ and $P_b(X)$ are the distributions of X_{s+b} and X_b, respectively. The 95% confidence level observed limit on BR is the value for which $1 - CL = 0.05$. This procedure is schematically represented in figure A.2.

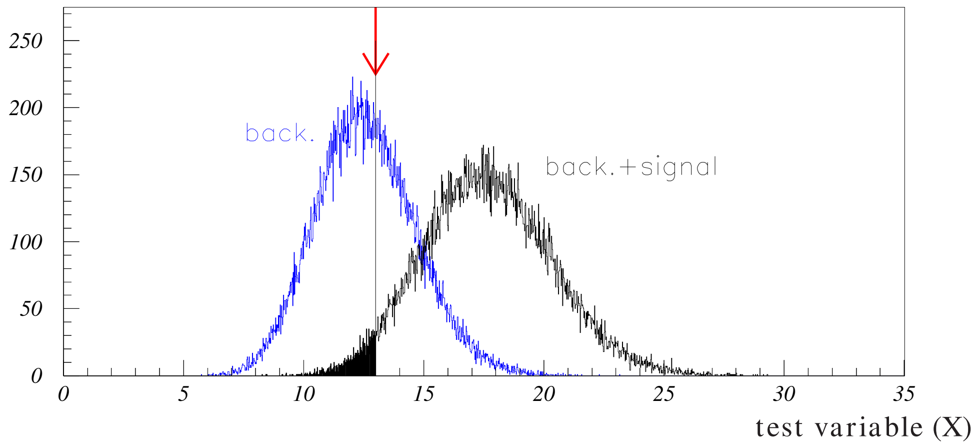

Figure A.2: *Schematic representation of the confidence level evaluation (adapted from [70]). The arrow represents X_d. The distributions of X_{s+b} and X_s are shown. The median of the background curve is displaced in relation to X_d, which indicates there is a small execess of data events in relation to the background expectation.*

The expected limit is defined as the limit which would be obtained if the data were exactly described by the SM background. It was evaluated by replacing X_d by the median of the X_b distribution.

A.3 Systematic errors in the limit derivation

In order to include the systematic uncertainties in the limits derivation, the discriminant variables corresponding to each set of systematic errors (see chapter 6) were calculated[2]. For each set of discriminant variables corresponding to each systematic error source (plus the set corresponding to the reference discriminant variables), X_d was calculated as discussed in the previous section. The considered test variable for data was the average of the different X_d. The statistical test variables for background plus signal and background only hypotheses were calculated in the following way: in each MC iteration (see previous section), a set of discriminant variables (*i.e.* one of the systematic uncertainty sets or the reference set) was randomly chosen for the X_{s+b} and X_b evaluation. The CL calculation was done as previously discussed.

[2]For each topology, b' mass and centre-of-mass energy, the data, SM expectation and signal discriminant variables corresponding to each systematic uncertainty source were calculated.

Bibliography

[1] S. L. Glashow *Nucl. Phys.* **22** (1961) 579.

[2] A. Salam, *Weak and Electromagnetic Interactions.* Originally printed in Svartholm: Elementary Particle Theory, Proceedings Of The Nobel Symposium, held at Lerum, Sweden, Stockholm, 1968.

[3] S. Weinberg *Phys. Rev. Lett.* **19** (1967) 1264.

[4] M. Gell-Mann *Phys. Rev.* **175** (1968) 2194.

[5] G. Zweig, *An SU_3 model for strong interaction symmetry and its breaking.* CERN/TH 401, 1964.

[6] C. Bouchiat, J. Iliopoulos and Ph. Meyer *Phys. Lett.* **B28** (1972) 519.

[7] S. Weinberg, *The Quantum Theory of Fields - volume II.* Cambridge University Press, 1998.

[8] P. W. Higgs *Phys. Rev. Lett.* **12** (1964) 132.

[9] P. W. Higgs *Phys. Rev. Lett.* **145** (1966) 1156.

[10] **Super-Kamiokande** Collaboration, S. Fukuda *et. al. Phys. Lett.* **B539** (2002) 179.

[11] **K2K** Collaboration, M. H.Ahn *et. al. Phys. Rev. Lett.* **90** (2003) 041801.

[12] **SNO** Collaboration, S. N. Ahmed *et. al.*, *Measurement of the Total Active* ^{8}B *Solar Neutrino Flux at the Sudbury Neutrino Observatory with Enhanced Neutral Current Sensitivity.* 2003. Nucl-ex/0309004 (submitted to *Phys. Rev. Lett.*).

[13] **KamLAND** Collaboration, K. Eguchi *et. al. Phys. Rev. Lett.* **90** (2003) 021802.

[14] J. W. F. Valle, *Brief neutrino physics update.* 2003. Talk given at the 2nd International Conference on String Phenomenology 2003, Durham, England. `hep-ph/0310125`.

[15] C. Giunti and M. Laveder, *Neutrino Mixing.* 2003. To be published in 'Progress in Quantum Physics Research', edited by V. Krasnoholovets, Nova Science Publishers, Inc. `hep-ph/0310125`.

[16] M. Kobayashi and K. Maskawa *Prog. Theor. Phys.* **49** (1973) 652.

[17] S. L. Glashow, J. Iliopoulos and L. Maiani *Phys. Rev.* **D2** (1970) 1285.

[18] **ALEPH** Collaboration, D. Decamp *et. al. Phys. Lett.* **B231** (1989) 519.

[19] **DELPHI** Collaboration, P. Aarnio *et. al. Phys. Lett.* **B231** (1989) 539.

[20] **L3** Collaboration, B. Adeva *et. al. Phys. Lett.* **B231** (1989) 509.

[21] **OPAL** Collaboration, M. Z. Akrawy *et. al. Phys. Lett.* **B231** (1989) 530.

[22] A. A. Rademakers, *The Determination of the Number of Light Neutrino Species.* PhD. Thesis, Universiteit van Amsterdam, 1991.

[23] **PDG** Collaboration, K. Hagiwara *et. al. Phys. Rev.* **D66** (2002).

[24] **LEP EEWG**, **SLD HFG**, **ALEPH**, **DELPHI**, **L3** and **OPAL** Collaborations, D. Abbaneo *et. al.*, *Combination of Preliminary Electroweak Measurements and Constraints on the Standard Model.* LEPEEWG/2003-01, 2003.

[25] A. Cuoco *et. al.*, *Present status of primordial nucleosysthesis after WMAP: results from a new BBN code.* astro.ph/0307213, 2003.

[26] D. N. Schramm and M. S. Turner *Rev. Mod. Phys.* **70** (1998) 303.

[27] I. J. R. Aitchinson and A. J. G. Hey, *Gauge Theories in Particle Physics.* Institute of Physics Publishing, 1993.

[28] **LEP Working Group for Higgs Bosons Searches**, **ALEPH**, **DELPHI**, **L3** and **OPAL** Collaborations, D. Abbaneo *et. al.*, *Search for Standard Model Higgs Boson at LEP.* CERN-EP/2003-011, 2003. Submitted to Phys. Lett. B.

[29] P. H. Frampton, P. Q. Hung and M. Sher *Phys. Rep.* **330** (2000) 263.

[30] A. Djouadi *et. al.*, *New particles and interactions*, in *Electroweak symmetry breaking and new physics at the TeV scale* (T. Barklow *et. al.*, eds.), p. 416, World Scientific, March, 1995. SLAC-PUB-95-6772.

[31] D. London, *Exotix fermions*, in *Precision Tests of the Standard Model* (P. Langacker, ed.), World Scientific, 1993.

[32] S. Godfrey, J. L. Hewett and L. E. Prince, *Discovery potential for new phenomena*, in *Snowmass 1996, New directions for high-energy physics* (D. G. Cassel *et. al.*, eds.), p. 846, Stanford Linear Accelerator Center, July, 1997. SLAC-PUB-7440.

[33] M. S. Carena, H. E. Haber and C. Wagner *Nucl. Phys.* **B472** (1996) 55.

[34] J. F. Gunion, D. W. McKay and H. Pois *Phys. Rev.* **D53** (1996) 1616.

[35] J. E. Dubicki and C. D. Froggatt *Phys. Lett.* **B567** (2003) 46.

[36] U. Cotti *et. al. Phys. Rev.* **D66** (2002) 015004.

[37] G. Triantaphyllou, *Mirror Fermions and the Hierarchy problem.* 1999. Talk given at the International Europhysics Conference HEP99, Tampere, Finland. `hep-ph/9908250`.

[38] M. Popovic *Phys. Rev.* **D64** (2001) 035001.

[39] G. C. Branco and L. Lavoura *Nucl. Phys.* **B278** (1986) 738.

[40] J. A. Aguilar-Saavedra *Phys. Rev.* **D67** (2002) 035003.

[41] V. Barger *et. al. Phys. Rev.* **D52** (1995) 1663.

[42] S. M. Oliveira and R. Santos *Phys. Rev.* **D68** (2003) 093012.

[43] S. M. Oliveira and R. Santos *Acta Phys. Polon.* **B34** (2003) 5523. Presented at the XXVII International Conference of Theoretical Physics, *Matter to the Deepest*, Ustron, Poland.

[44] T. Yanir *JHEP* **06** (2002) 044.

[45] M. E. Peskin and T. Takeuchi *Phys. Rev.* **D46** (1992) 381.

[46] M. E. Peskin and T. Takeuchi *Phys. Rev. Lett.* **65** (1990) 964.

[47] P. Langacker *J. Phys.* **G29** (2003) 35.

[48] A. Arhrib and W. S. Hou *Phys. Rev.* **D64** (2001) 07316.

[49] V. A. Novikov, L. B. Okun, A. N. Rozanov and M. I. Vysotsky *Phys. Lett.* **B259** (2001) 111.

[50] H. J. He, N. Polonsky and S. Su *Phys. Rev.* **D64** (2001) 043004.

[51] W. S. Hou and R. G. Stuart *Phys. Rev. Lett.* **62** (1989) 617.

[52] W. S. Hou and R. G. Stuart *Nucl. Phys.* **B320** (1989) 277.

[53] W. S. Hou and R. G. Stuart *Phys. Lett.* **B242** (1990) 467.

[54] W. S. Hou and R. G. Stuart *Nucl. Phys.* **B349** (1991) 91.

[55] B. Haeri, G. Eilam and A. Soni *Phys. Rev. Lett.* **62** (1989) 719.

[56] B. Haeri, G. Eilam and A. Soni *Phys. Rev.* **D41** (1990) 875.

[57] M. Sher *Phys. Rev.* **D61** (2000) 073016.

[58] **ALEPH** Collaboration, D. Decamp *et. al. Phys. Lett.* **B236** (1990) 511.

[59] **DELPHI** Collaboration, P. Abreu *et. al. Nucl. Phys.* **B367** (1991) 511.

[60] **L3** Collaboration, O. Adriani *et. al. Phys. Rep.* **B236** (1993) 1.

[61] **OPAL** Collaboration, M. Z. Akrawy *et. al. Phys. Lett.* **B246** (1990) 285.

[62] T. Affolder *et. al. Phys. Rev. Lett.* **84** (2000) 835.

[63] **D∅** Collaboration, S. Abachi *et. al. Phys. Rev.* **D52** (1995) 4877.

[64] C. D. Froggatt, D. J. Smith and H. B. Nielsen *Z. Phys.* **C73** (1997) 333.

[65] *LEP Design Report (volumes I, II and III).* CERN-TH/83-29 (volume I), CERN-LEP/84-01 (volume II) and CERN-AC/96-01 (volume III), 1984-1996.

[66] R. Assmann, M. Lamont and S. Myers, *A brief history of the LEP collider*, *Nucl. Phys. Proc. Suppl.* **109** (2002) 17.

[67] A. Blondel *et. al. Eur. Phys. J.* **C11** (1999) 573.

[68] **DELPHI** Collaboration, P. Aarnio *et. al. Nucl. Instrum. Meth.* **A303** (1991) 276.

[69] **DELPHI** Collaboration, P. Abreu *et. al. Nucl. Instrum. Meth.* **A378** (1996) 57.

[70] S. Andringa, *Study of the Anomalous Quartic Gauge Couplings and Search for Fermiophobic Higgs at LEP2.* PhD. Thesis, Instituto Superior Técnico da Universidade Técnica de Lisboa, 2003.

[71] T. Camporesi *et. al.*, *Luminosity Measurement in 1994 with the STIC detector.* 1997. DELPHI-97-08 PHYS/667.

[72] B. Tomé, *High Precision Luminosity Measurement al LEP with the DELPHI STIC calorimeter.* PhD. Thesis, Faculdade de Ciências da Universidade de Lisboa, 1998.

[73] Ph. Charpentier *et. al.*, *The DELPHI fastbus data aquisition system.* 1991. DELPHI 91-92 DAS 112.

[74] T.J. Adye *et. al.*, *The design and operation of the slow controls for the DELPHI experiment at LEP.* 1994. DELPHI 94-14 DAS 151.

[75] S. Amato, *Quality Checking of the Reconstructed Data at the Pit.* 1996. 96-17 DAS 173.

[76] W. J. Murray, *Fast Offline Quality Checking of the DELPHI data in 1996.* 1998. 98-32 GEN 175 PROG 230.

[77] **DELPHI** Trigger Group, J. Augustinus *et. al.*, *The DELPHI trigger system at LEP2 energies.*, *submitted to Nucl. Instr. and Meth. A* (2002). CERN-EP-2002-086.

[78] M. Elsing *et. al.*, *Changes in the track reconstruction to recover from the TPC sector 6 failure.* 2001. DELPHI-2001-004 TRACK/95.

[79] **DELPHI** Collaboration, *DELANA User's guide.* 1989. DELPHI-89-44 PROG/137.

[80] D. Bertrand and L. Pape, *TANAGRA, Track Analysis and Graphics Package.* 1987. DELPHI-87-95 PROG/98.

[81] D. Bertrand *et. al.*, *DELGRA, DELPHI Graphics for Interactive Event Viewing – User Manual.* 1998. `http://delgra.home.cern.ch/delgra`.

[82] M. Elsing, *The new 'ID+VD' track search in DELANA.* 1995. DELPHI-99-171 TRACK/95.

[83] F. Cossutti and A. Tonazzo, *REMCLU: a package for the Reconstruction of ElectroMagnetic CLUsters at LEP200.* 1995. DELPHI-99-171 TRACK/95.

[84] N. Crossland, Wilkinson, G. and Kluit, P., *EMMASS Muon Identification within DELPHI*. 1992. DELPHI-92-17 PHYS/157.

[85] H. De Boeck and G. Wilkinson, *MUFLAG: A Framework for Muon Identification*. 1993. DELPHI-93-14 PHYS/263.

[86] T. Sjöstrand *Comp. Phys. Comm.* **135** (2001) 238.

[87] **L3** Collaboration. This plot can be found in `http://l3www.cern.ch`. Similar plots by the other LEP collaborations were not found.

[88] E. Accomando and A. Ballestero *Comp. Phys. Comm.* **99** (1997) 270.

[89] T. Sjöstrand *Comp. Phys. Comm.* **82** (1994) 74.

[90] S. Jadach, B.F.L. Ward and Z. Was *Comp. Phys. Comm.* **130** (2000) 260.

[91] S. Jadach, B.F.L. Ward and Z. Was *Phys. Lett.* **B390** (1997) 298.

[92] **DELPHI** Collaboration, *DELSIM, DELPHI event generation and detector simulation*. 1989. DELPHI-89-68 PROG/143.

[93] S. Catani *et. al. Phys. Lett* **B256** (1991) 432.

[94] **DELPHI** Collaboration, J. Abdallah *et. al. Eur.Phys.J* **C32** (2004) 185.

[95] **DELPHI** Collaboration, P. Abreu *et. al. Nucl. Instr. Meth.* **A427** (1999) 487.

[96] N. Kjar and R. Møler, *Reconstruction of invariant masses in multi-jet events*. 1991. DELPHI-91-17 PHYS/88.

[97] G. Fox and S. Wolfram *Nucl. Phys.* **B149** (1979) 413.

[98] G. Fox and S. Wolfram *Phys. Lett.* **B82** (1979) 139.

[99] J. Matews and R.L. Walker, *Mathematical Methods of Physics*. Addison-Wesley, 1970.

[100] A. Read, *Modified Frequentist Analysis of Search Results (The CL_S Method)*. 2000. CERN report 2000-005.

[101] G. Altarelli *et. al.*, Physics at LEP2. 1996. CERN 96-01 (volume 2).

[102] S. Jadach *et. al.*, *LEP2 Monte Carlo* in 'Report of the Working Groups on Precision Calculations for LEP2 Physics'. 2000. CERN 2000-009.

[103] **DELPHI** Collaboration, J. Abdallah *et. al.*, *Searches for supersymmetric particles in e^+e^- collisions up to 208 GeV and interpretation of the results within the MSSM*. 2003. CERN/EP 2003-007.

[104] I. F. Ginzburg, I. P. Ivanov and A. Schiller *Phys. Rev.* **D60** (1999) 095001.

[105] E. Arik, O. Cakir, S. A. Cetin and S. Sultansoy *Phys. Rev.* **D66** (2002) 116006.

[106] P. Gonçalves, *Test of QED and Search for New Physics in Multi-Photonic Final States at LEP 2*. PhD. Thesis, Instituto Superior Técnico da Universidade Técnica de Lisboa, 2002.